Imperial College London

Topological Insulators and their Topological Markers

A thesis submitted in partial fulfilment of the requirements for the degree of

Doctor of Philosophy of Imperial College London

and the

Diploma of Imperial College London

by

Joseph Sykes

Department of Mathematics

Imperial College London

180 Queen's Gate, London SW7 2BZ

January 2022

Declaration of Originality

I certify that this thesis, and the research to which it refers, are the product of my own work, and that any ideas or quotations from the work of other people, published or otherwise, are fully acknowledged in accordance with the standard referencing practices of the discipline. Parts of this thesis appear in the following published articles:

- Local topological markers in odd dimensions, J Sykes, R Barnett, Physical Review B 103, 155134 2021
- 1D quasicrystals and topological markers, J Sykes, R Barnett, arxiv: 2201.09741 2022

Signed:_____

Copyright Statement

Acknowledgements

I would first like to thank my supervisor Ryan Barnett for giving me the opportunity carry out research in this wonderful and exciting new field of physics. I would also like to thank him for all the patience and guidance he has offered me throughout these past years as well as for all the knowledge he has shared with me.

I would also like to thank my colleagues Peru d'Ornellas, Derek Lee, Gregory Chaplain, Mathew Proctor and Chris Oliver for all the interesting conversations they made possible. Some of the best ideas in research come from spontaneous discussions had with colleagues and discussions with these people over the past few years has both helped and inspired me in a lot of the work I present here.

I also want to thank Sam Carr and Chris Hooley as well as all the other people who made Physics by the lake 2019 possible.

Finally, I would like to thank my fiancé for supporting me throughout my PhD and believing in me when I didn't believe in myself.

Abstract

Topological physics is a rapidly developing field that could potentially open the door to utilising quantum mechanics in electrical circuits. The discovery of local topological markers for two-dimensional (2D) systems has allowed the investigation of disordered topological systems as well as topological quasicrystal systems. However, adapting these topological markers to one-dimensional (1D) time-dependent systems is not straight forward. The aim of this thesis is to develop topological markers for 1D time-dependent systems, three-dimensional (3D) time-dependent systems and 1D time-dependent aperiodic systems.

We first develop a topological marker for 1D time-dependent systems and use it to determine the topological structure of a known Hamiltonian. We then use this marker to investigate how different types of disorder affect the topological structure of a system. We also show that this marker can determine the polarisation of any system, topological or not. Next, we use the marker to analyse the topological phase transitions of the Generalised Aubry-André model finding that this model displays numerous topological phase transitions, some of which are between topologically trivial and topologically non-trivial systems.

We then develop a topological marker that determines the second Chern number of a 3D time-dependant system. We confirm its accuracy using a 3D Hamiltonian with known topological structure.

Afterwards, we adapt the 1D marker such that it can be used to determine the topological structure of 1D time-dependent aperiodic systems. We then use this marker to investigate a quasicrystal with known topological structure as well as a system with unknown topological structure and confirm the accuracy of the adapted 1D marker. Next, we use this marker to investigate the topological structure of two aperiodic systems which have previously been hard to study and show that both systems possess a topological nature. Finally, we show that this marker can also determine the polarisation of aperiodic systems.

Contents

List of Figures

1

Introduction

Condensed matter physics is a staggeringly large field of physics which aims to describe the properties of many-particle systems. These systems are described using both electromagnetism and quantum mechanics with the other fundamental forces playing little part in the description. The study of condensed matter systems is a vibrant field of study due to the fact that increasing the number of particles within a system increases its complexity and in doing this allows emergent properties to arise. Philip Warren Anderson, the theoretical physicist responsible for naming the field of condensed matter physics, once wrote [2]

> "The behavior of large and complex aggregates of elementary particles, it turns out, is not to be understood in terms of a simple extrapolation of a few particles. Instead, at each level of complexity entirely new properties appear."

A large part of condensed matter physics is the understanding of phase transitions between different states a system can take. One example of this is the phase transition between a ferromagnetic system and a paramagnetic system. Within a ferromagnetic system all the magnetic moments are aligned in the same direction and have equivalent magnitude; as such, the system has an overall magnetic orientation and is therefore magnetic. As the temperature of the system is increased each magnetic moment acquires more energy which allows them to change their orientation relative to one another.

At the Curie temperature each magnetic moment has enough energy such that it can point in any direction. This causes the magnetic moments to point in random directions and destroys the overall magnetic orientation of the system resulting in the system no longer being magnetic; thus the system has transitioned into a different phase. This phase transition can be described in terms of a breaking of symmetry within the system. In the paramagnetic state the system has rotational invariance due to the randomly orientated magnetic moments; transitioning to the ferromagnetic state breaks this rotational symmetry and the system becomes more ordered. In fact, the use of symmetry breaking to explain phase transitions is very general and can be applied to a variety of systems all across physics [3]. However, in the latter part of the 20th century phase transitions which could not be described by symmetry breaking started to be observed. It later transpired that a number of these phase transitions were due to a change in the topological structure of the system.

In 1980 K. Klitzing observed one of the first topological effects of a system by analysing the Hall resistivity of a 2D electron gas with a magnetic field applied perpendicular to it. It was seen that the Hall resistivity took the form $\rho_{xy} = \frac{h}{e^2}\frac{1}{v}$ with v being restricted to integer values. As such, the Hall resistivity displayed plateaus, along with sharp increases, in its behaviour as the strength of the magnetic field was increased [4]. This was contrary to the expected linear behaviour and this effect is now known as the quantum Hall effect. In 1982 D. Thouless, M. Kohmoto, M.P. Nightingale, M. den Nijs released a paper in which the behaviour of the Hall resistivity was ascribed to the change in the Chern number of the system which describes the system's topological phase [5]. It was shown that the Chern number is restricted to take on integer values and can only change when the energy gap considered closes or the number of bands occupied increases (which is the case in the quantum Hall effect). This therefore explained the plateaued behaviour along with the sudden increases. Their paper also highlighted that the Chern number is related to the change in the phase of the systems wave function. This then clarifies why topological phase transitions cannot be described by traditional symmetry breaking methods. These two papers played a fundamental role in the creation of a new field in condensed matter physics known as topological insulators and were key in developing the broader field of topological phases of matter. The year 1982 also saw the discovery of the Fractional Quantum Hall Effect (FQHE) where the value of v in the Hall resistivity, $\rho_{xy} = \frac{h}{e^2}\frac{1}{v}$, can take on specific fractional values (e.g. $\frac{1}{3}$, $\frac{2}{5}$, $\frac{3}{7}$ ...). This effect was first observed by D. Tsui and H. Störmer and requires electron-electron interactions in the system to be observed. The understanding of the FQHE depends on fractionally-charged quasiparticles and quasihole excitations along with their interactions. A large part of this understanding came from a theory proposed by R. Laughlin and was further expanded upon by others to account for unexplained fractional cases [6, 7]. The FQHE will not be addressed within this thesis and we refer the reader to [8, 7] for further details. Despite its relatively young age, the field of topological phases of matter has already received 3 Nobel prizes; one in 1985

awarded to Klaus von Klitzing for his work on measuring the quantum Hall effect, one in 1998 awarded to Robert B. Laughlin, Horst L. Störmer and Daniel C. Tsui for their work on the fractional quantum Hall effect and the discovery of a fractionally charged quantum fluid, and one more recently in 2016 awarded to David J. Thouless, F. Duncan M. Haldane and J. Michael Kosterlitz for their contributions to the understanding of topological physics and topological phase transitions.

Since the 1980s the field of topological phases of matter has rapidly expanded and many new interesting areas of study have developed within it. One of these areas is the study of 1D topological pumps which was first proposed in 1982 by D. Thouless [9]. It was shown that if a 1D time-dependent system is topological in nature then, as a result of this, it will pump a quantized amount of charge across the system over a full time period with the quantized amount of charge directly proportional to the Chern number of the system. Despite its early prediction, this phenomenon has only recently be observed experimentally in cold atomic gas systems [10, 11, 12, 13]; as well as photonic systems [14, 15, 16]. This pumping effect has also been shown to exist in magneto-mechanical meta-materials and elastic lattice systems [17, 18]. In the 1990s the modern theory of polarisation was developed and shed a new light on the effect of topological pumping [19, 20, 21, 22, 23]. This new theory showed that the Chern number for a 1D time dependent system is equal to the change in the polarisation of the system over a time period which, in turn, explained why 1D topological systems exhibit quantized pumping. Understanding and harnessing this effect of quantized pumping could have important implications for systems requiring fine current control. One obvious area that this could greatly benefit is the control of lasers for etching, shaping and imaging materials. The precise control of lasers is important in many processes from microchip manufacturing to medical equipment design to experimental set-ups in physics and chemistry.

At this point it is worth pointing out that while topological effects can be observed in photonic systems the topology that arises here is slightly different than the topology that arises in cold atomic systems. This is due to the fact that photonic systems consist of light particles which are bosons where as cold atomic systems usually consist of electrons which are fermions. Due to this difference the concept of a band structure makes sense for cold atomic systems but does not make sense for photonic systems. Throughout this thesis we will concentrate on explaining the topological properties that arise in fermionic systems rather than bosonic systems.

In the years since the discovery of the quantum Hall effect the topological structure of higher dimensional systems has been investigated and it has been shown that for both three dimensional time-dependent systems and four dimensional systems another topological index arises; this is known as the second Chern number [24]. For the three dimensional time-dependent case it was shown that the second Chern number can be linked to the change in the isotropic part of the magneto-electric polarisability of the system over a full time period [24, 25, 26]. This has parallels with the relation between the first

Chern number and the change in the polarisation of a one dimensional system mentioned previously. Unlike the one dimensional case however, it is not clear what is pumped through the system in the three dimensional case when no magnetic or electric field is present but the second Chern number of the system takes on a non-zero value. More success has been found for the four dimensional case. Considerable advances in the understanding of the topological structure of four dimensional systems like the four dimensional quantum Hall effect (4D QHE) have been made [27, 28, 29]. As well as this, despite the fact that the real world only possesses three spatial dimensions, not four, the 4D QHE has been observed in both photonic and cold atomic experiments [30, 31]. In both cases this was achieved by simulating two of the spatial dimensions with 'synthetic' dimensions. These experiments showed that when the the 4D QHE is realised in two dimensions the edge state modes can exhibit more exotic behaviours like corner to corner pumping and edge to edge pumping rather than propagating around the edge of the system as seen in the two dimensional QHE.

At this point it is important to stress that the Chern number and the second Chern number are not the only topological invariant used to classify the topological nature of a system. To understand why more than one topological invariant is needed we first have to understand the types of systems that can display topological behaviour. This has previously been understood via the classification method known as the 'ten-fold way' and from this a periodic table of topological systems has been developed for varying dimensions (shown in table 1.2) [32]. The Ten-fold way considers a generic non-interacting single-particle Hamiltonian and classifies it into ten categories according to how the Hamiltonian reacts under time-reversal symmetry, charge-conjugation symmetry and chiral symmetry (sometimes referred to as 'sublattice' symmetry). To understand this classification let us take a closer look at these symmetries.

A Hamiltonian, $\mathcal{H}$, is invariant under time-reversal symmetry if the complex conjugate of $\mathcal{H}$ is equal to $\mathcal{H}$ up to some unitary rotation U_T:

$$U_T^\dagger \, \mathcal{H}^* \, U_T = \mathcal{H}. \tag{1.1}$$

As well as this, if the system is time-reversal symmetric the square of the time-reversal operator can be either plus the identity operator or minus the identity operator, $\mathcal{T}^2 = \pm 1$. From this we label the three possible cases with the value T as follows; if the system is not time-reversal symmetric we label it with $T = 0$, if the system is time-reversal symmetric and $\mathcal{T} = +1$ we label this with $T = +1$, and if the system is time-reversal symmetric and $\mathcal{T} = -1$ we label this with $T = -1$.

Next, we look at charge-conjugation. A system is invariant under charge-conjugation symmetry if the complex conjugate of the Hamiltonian is equal to minus the Hamiltonian up to some unitary

Symmetry Class	T	C	S
A	0	0	0
AI	+1	0	0
AII	-1	0	0
AIII	0	0	1
BDI	+1	+1	1
CII	-1	-1	1
D	0	+1	0
C	0	-1	0
DIII	-1	+1	1
CII	+1	-1	1

Table 1.1: Table showing the 10 symmetry classes for single-particle Hamiltonians, classified by their behaviour under time-reversal symmetry, $\mathcal{T}$, charge-conjugation symmetry, $\mathcal{C}$ and chiral symmetry, $\mathcal{S}$.

rotation:

$$U_C^\dagger \, \mathcal{H}^* U_C \; = \; -\mathcal{H}. \tag{1.2}$$

Like the time-reversal operator, the square of the charge-conjugation operator, $\mathcal{C}$, can be plus or minus the identity operator. We therefore have three cases which we label with C; if the system is not invariant under charge conjugation we set $C = 0$, if the system is invariant under charge conjugation and $\mathcal{C}^2 = +1$ we set $C = +1$, and if the system is invariant under charge conjugation and $\mathcal{C}^2 = -1$ we set $C = -1$.

With these two symmetries we have 9 possible cases. The tenth case comes from considering the chiral symmetry of the Hamiltonian. The chiral symmetry of the Hamiltonian is given by the combined operation of time-reversal symmetry and charge conjugation symmetry such that $\mathcal{S} = \mathcal{T} \cdot \mathcal{C}$, where $\mathcal{S}$ is the chiral symmetry operator. For 8 of the possible 9 cases the chiral symmetry operator is determined by the product of T and C and therefore does not contribute any more cases. However, for the case where $T = 0$ and $C = 0$ the system can either be invariant under chiral symmetry, which we label with $S = 1$, or not, which we label with $S = 0$ (for the 8 determined cases we set $S = 0$ if the product of T and C is zero and $S = 1$ otherwise). This then gives us our extra case giving a total of ten possible cases. These 10 cases are labelled in table 1.1.

Now we have introduced the different topological classes of the ten-fold way we can analyse these classes in different dimensions and ask if the system is topological or not. Tabulating this information makes up the 'Periodic table of topological insulators' and is shown in table 1.2 [33, 32]. This table provides us with a bit more information than if the system can be topological or not, it also tells us what values the topological invariant can take. With this table we are now ready to answer why more than one topological invariant is needed. We previously mentioned that the Chern number can be used to determine the topological structure of the 2D IQHE. This system falls into the symmetry

Symmetry Class	$d=0$	$d=1$	$d=2$	$d=3$	$d=4$	$d=5$	$d=6$	$d=7$	$d=8$
A	$\mathbb{Z}$	0	$\mathbb{Z}$	0	$\mathbb{Z}$	0	$\mathbb{Z}$	0	$\mathbb{Z}$
AIII	0	$\mathbb{Z}$	0	$\mathbb{Z}$	0	$\mathbb{Z}$	0	$\mathbb{Z}$	0
AI	$\mathbb{Z}$	0	0	0	$2\mathbb{Z}$	0	$\mathbb{Z}_2$	$\mathbb{Z}_2$	$\mathbb{Z}$
BDI	$\mathbb{Z}_2$	$\mathbb{Z}$	0	0	0	$2\mathbb{Z}$	0	$\mathbb{Z}_2$	$\mathbb{Z}_2$
D	$\mathbb{Z}_2$	$\mathbb{Z}_2$	$\mathbb{Z}$	0	0	0	$2\mathbb{Z}$	0	$\mathbb{Z}_2$
DIII	0	$\mathbb{Z}_2$	$\mathbb{Z}_2$	$\mathbb{Z}$	0	0	0	$2\mathbb{Z}$	0
AII	$2\mathbb{Z}$	0	$\mathbb{Z}_2$	$\mathbb{Z}_2$	$\mathbb{Z}$	0	0	0	$2\mathbb{Z}$
CII	0	$2\mathbb{Z}$	0	$\mathbb{Z}_2$	$\mathbb{Z}_2$	$\mathbb{Z}$	0	0	0
C	0	0	$2\mathbb{Z}$	0	$\mathbb{Z}_2$	$\mathbb{Z}_2$	$\mathbb{Z}$	0	0
CI	0	0	0	$2\mathbb{Z}$	0	$\mathbb{Z}_2$	$\mathbb{Z}_2$	$\mathbb{Z}$	0

Table 1.2: Table classifying the different types of topological systems stated in table 1.1 for varying dimensions. The value 0 indicates that this system is not topological in nature and the values $\mathbb{Z}$ and $\mathbb{Z}_2$ indicate that the system can be topological in nature with its topological invariant restricted to values within the respected groups. The value $2\mathbb{Z}$ again indicates that the system can be topological in nature but its topological invariant can only take on even integers due to some doubling of the degrees of freedom. An example of this doubling could be due to Kramers degeneracy.

class A and has a topological invariant restricted to $\mathbb{Z}$. In general, the Chern number and its higher dimensional forms can be used to describe the topological structure of any even dimensional (or odd dimensional time-dependant) topological system labelled by $\mathbb{Z}$. Looking at the symmetry class AIII we see that these types of systems are described by a topological invariant restricted to $\mathbb{Z}$ and only possess topological properties in odd dimensions. Due to the Chern number only being well defined for systems with an even number of dimensions, it can not be used to describe the topological structure of the symmetry class AIII. The topological structure of this class is determined by another topological invariant known as the winding number. This then demonstrates the need for more than one type of topological invariant. Over all there are four main topological invariants used to describe the topological structure of all ten symmetry classes; the Chern number, the winding number, the Chern-Simons invariant, and the Kane-Mele invariant (sometimes known as the Fu-Kane-Mele or the Fu-Kane invariant). In this thesis we will concentrate on systems that can be described by the Chern number, however, for more information on the other topological invariants see [32] and the citations therein.

In the past decade there has been another important advance in the field of topological physics; the development of local topological markers. These objects can be used to measure the topological index of a system but, unlike most methods, do not require translational invariance to be evaluated. This is very useful as it allows one to determine the topological structure of a system that has an inhomogeneous nature. These objects also allow one to investigate the topological structure within a small region of a system meaning the effects of local defects within a system can be investigated. Determining how local defects affect the topological properties of a system is a crucial step if topological properties are to be utilised within modern technology. The most prevalent of these local topological

markers is the Chern marker which is defined for two dimensional systems and was presented by Raffaello Bianco and Raffaele Resta in 2011 [34]. The Chern marker has been used to probe the topological phases along with topological phase transitions of many two dimensional inhomogeneous systems [35, 36, 37, 38, 39, 40, 41, 42, 43]. Generally the Chern marker is used to measure the topological structure of a system in equilibrium, however, recent work analysed the non-equilibrium dynamics of the Chern marker for a system undergoing a quantum quench from a topological regime to a non-topological regime [44]. It was shown that after the quench the value of the Chern marker through the system fluctuated and displayed a current like behaviour. The Chern marker has also been employed to investigate the topological aspects of non-Hermitian systems where boundary conditions are important as they can affect the topological properties of the system [45]. It is clear then that the Chern marker is very useful for investigating the topological properties of two dimensional systems. Due to the way it is defined, however, it is not straightforward to apply the Chern marker to one dimensional time-dependent systems or adapt it to analyse three dimensional time dependent systems.

One other developing subfield of topological physics is that of topological quasicrystals. To define a quasicrystal system it is first best to define an aperiodic crystal; of which quasicrystals are a special type. Aperiodic crystals are crystals that have some structural order, but do not possess translational invariance. The structural order can be determined by analysing the Fourier transform of the lattice structure to see if it possesses sharp diffraction peaks. If a system possesses sharp diffraction peaks and is not translationally invariant it is said to be aperiodic. Quasicrystal systems are a special type of aperiodic crystal in that they are said to have an almost periodic structure. These systems can be differentiated by analysing the Fourier transform of their lattice structure to see if it displays a countable set of diffraction peaks with a well-defined spacing [46]. For a more in-depth discussion about aperiodic and quasicrystal order see [47].

Figure 1.1 shows a 2D quasicrystal pattern known as Penrose tiling. From this figure it can be seen that this pattern has repeating sections along with rotational symmetry but does not have translational invariance. It has been shown that the Penrose tiling, as well as other two dimensional quasicrystal patterns, can possess topological properties [48, 49]. However, due to their non-transitionally invariant structure the Chern number cannot be used for these types of systems and the Chern marker has to be used to investigate the topology of 2D quasicrystal structures. Topological properties have also been identified in one dimensional time-dependent quasicrystal systems. However, only a small subset of these types of systems have been investigated [14, 50, 15, 51]. This is due to the fact that a one dimensional time-dependent topological marker would be needed to investigate these types of systems. Without this topological marker only one dimensional time-dependent quasicrystal systems that can be mapped to two dimensional time independent systems can be investigated. The one dimensional systems that have been investigated display complex topological structures that may prove useful in

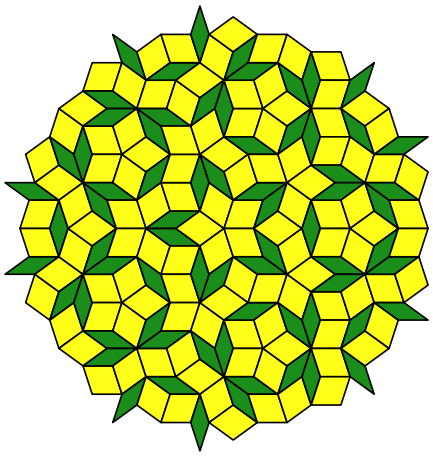

Figure 1.1: A 2D quasicrystal pattern known as Penrose tiling. The pattern is made of two types of rhombi which are coloured differently to identify them.

the future.

Outline

Within this thesis we aim to introduce the reader to topological markers that can be used for one dimensional and three dimensional time-dependent systems and demonstrate how useful these objects can be when investigating topological systems. We also wish to demonstrate how the one dimensional topological marker can be altered such that it can be used to investigate the topological structure of any one dimensional quasicrystal or aperiodic system.

We start in chapter 2 by introducing the Chern number along with all the constituent parts needed to make it. We derive it for both the discrete and continuous cases seen as the discrete case is very useful when calculating the Chern number numerically. We also introduce the Diophantine equation, which can be used to determine the Chern number of specific systems, as well as the second Chern number seen as these will both be used later in the thesis. We also look at the effects a non-zero topology has on a system by analysing edge modes that arise within these systems. We start by analysing how edge state modes behave in one dimensional time-dependent systems and then move on to analyse their behaviour in two dimensional systems.

In chapter 3 we introduce the Hamiltonians that will be analysed throughout this thesis. We demonstrate the topological structure of some of these Hamiltonians but leave others unspecified when the topological structure requires further specification of the Hamiltonian.

After this we introduce the Chern marker for 2D systems in chapter 4 and demonstrate its usefulness

by using it to analyse the topological structure of the Hofstadter butterfly. We also define the Chern marker for a four dimensional system system in this section, drawing parallels with the two dimensional version.

Chapter 5 introduces the Bott index which is a different method for determining the topological structure of a system. Here we first define the Bott index and then show analytically that the Bott index is equivalent to the Chern number in both the continuous and the discrete cases. We then analyse the relation between the local version of the Bott index and the Chern marker, finding that the local Bott index and the Chern marker are equivalent when the system is of reasonable size.

In chapter 6 we define a local topological marker for one dimensional time-dependent systems and demonstrate numerically that it can be used to correctly predict the topology of the system. We also show that the change in the one dimensional marker over time is equivalent to the polarisation of the system. We then use this marker to investigate systems with both local and random disorder and analyse how this affects the topological structure of the system. Lastly, we investigate topological phase transitions of the generalised Aubry-André model by producing a topological phase diagram. We do this for the regime where the fixed hopping parameter in this system is set to one and for the regime where it is set to zero. We find that the later case displays numerous phase transitions some of which are from a topologically non-trivial system to a topologically trivial one.

Chapter 7 then goes on to develop a topological marker for three dimensional time-dependent systems using similar techniques defined for the one dimensional topological marker. We also show that the three dimensional marker is equal to the change in the Chern-Simons axion coupling over time. After this the three dimensional marker is used to determine the topological structure of a three dimensional time-dependent Hamiltonian with a known second Chern number and it is found that the topological marker correctly predicts the second Chern number of the system.

With this we then move on to analyse a one dimensional time-dependent quasicrystal system in chapter 8 using an altered version of the one dimensional marker introduced in chapter 7. It is shown that this altered version of the marker can accurately predict the topological structure of both periodic and quasicrystal systems. We then use the altered marker on a system with unknown topological structure and confirm the markers accuracy by analysing the current through the system as well as looking at the change in the Wannier centres of the system. As well as this, we show that, like in the periodic case, the marker can be used to determine the topological structure of a region within the system, but find that this region has to be considerably larger than in the periodic case to give an accurate prediction. Having shown that the marker works for systems with a quasicrystal structure we then investigate systems with aperiodic structure. We analyse the topological structure of two systems; one with the Thue-Morse sequence determining the atomic structure and the other with the Period-doubling sequence determining the atomic structure. We find that these aperiodic systems can

possess a non-zero topological structure despite them not having a quasicrystaline nature. Finally, we show in this chapter that the equality between the polarisation of the system and the one dimensional marker persists for both quasicrystal and aperiodic systems also.

Chapter 9 demonstrates that the Aubry-André model can be used not only to determine the topological structure of the Fibonacci chain, shown previously by Kraus and Zilberberg [50], but can also determine the topological structure of any noble mean chain. It is then shown how the parameter b of the Aubry-André model can be determined so that the topology of the desired noble mean chain is realised.

Finally, chapter 10 concludes by reviewing the new material shown in this thesis as well as discussing possible future directions and applications that could arise due to these findings.

2

Chern Number

Topology is a well established field of mathematics and is concerned with classifying geometrical objects through continuous deformations such as stretching, compressing, twisting and bending. Two objects are said to be topologically distinguishable if one has to tear, glue or open or close holes within one of the objects to deform it into the other. The most famous example of this is the coffee cup and the doughnut; these objects are topologically equivalent because one can perform a continuous deformation on the coffee cup and produce a doughnut. In this example the important feature of each shape is the number of holes in the object. It is said that both the coffee cup and the doughnut have a genus of 1 and therefore they are topologically equivalent. Both of these objects are topologically distinct from a ball seen as the ball has a genus of 0 due to it having no holes in it. From this it is obvious that the topology of an object is a global property because it requires the analysis of the whole object.

The idea of classifying objects through continuous deformations is a very useful concept in condensed matter physics, especially when classifying insulators which will be the topic of this thesis. Using electronic band structure theory a material is defined as an insulator when all the energy bands are populated or when its Fermi-Energy lies between two separated bands. For the former case the electrons in the material are fixed in place and the material does not conduct electricity. However, for the latter case this is not strictly true and cases can arise where electrons can flow in very specific ways through the system. To distinguish between these types of insulators we use the ideas from topology

and ask whether two Hamiltonians can be continuously deformed into each other without the band gap closing. If this is the case it is said that the two Hamiltonians are topologically equivalent and possess the same topological band structure. It is important that the band gap remain open throughout the deformation to ensure the topology of the system does not change. The application of topological classification to insulators was a major break through in the condensed matter field and resulted in the 2016 Nobel prize in physics being awarded for this work.

Just like the genus allows us to distinguish the topology of a coffee cup from the topology of a ball one can define objects that classify the topology of Hamiltonians. Throughout this thesis we will refer to these objects as topological indices. For two dimensional (2D) time-independent systems and one dimensional (1D) time dependent systems there exists a topological index known as the Chern number which can be used to determine the topological structure of these systems. For three dimensional (3D) time-dependent systems and four dimensional (4D) time-independent systems another topological index exists which is known as the second Chern number. In this section we will define both the first and second Chern numbers.

This chapter is structured as follows. First, we will recap Bloch's theorem for the continuous case as well as for the discrete case. Here we will introduce specific notation that will be used throughout this thesis. Next we derive the Berry phase, Berry flux and the Chern number for the discrete case. Then, using the discrete case as a guide, we will derive the Berry phase, Berry flux and Chern number for the continuous case. We will also show an alternate form of the Berry Flux and Chern number that is useful in showing the relationship between the Hall conductance and the Chern number of a 2D topological system. After this, we will state the form of the second Chern number. Throughout this thesis we will sometimes refer to the first Chern number as the Chern number. We also sometimes refer to both the first Chern number and the second Chern number as the topological index of the system but in each case it will be obvious which one we are referring to. Finally, we will look at the properties that arise from a system being topological in nature by analysing the edge state modes of the system.

2.1 Bloch's Theorem Notation

Within this thesis we will be interested in the bulk properties of both periodic and aperiodic Hamiltonians, but we will start by analysing periodic Hamiltonians first. Felix Bloch pioneered the current quantum mechanical understanding of electrons in a periodic structure with his thesis entitled "Quantum Mechanics of the Electron in Crystal Lattices" [52]. Within this he demonstrated Bloch's theorem which states that for a potential $V(\boldsymbol{x})$ with a periodicity equal to $\boldsymbol{r}$, $V(\boldsymbol{x}) = V(\boldsymbol{x} + \boldsymbol{r})$, the energy

eigenstates take the form

$$\psi_{\boldsymbol{k},n}(\boldsymbol{x}) = e^{i\boldsymbol{k}\cdot\boldsymbol{x}} u_{\boldsymbol{k},n}(\boldsymbol{x}). \tag{2.1}$$

Above, $\psi_{\boldsymbol{k},n}(\boldsymbol{x})$ is the single-particle wave function, $\boldsymbol{k}$ is the wave vector and $u_{\boldsymbol{k},n}(\boldsymbol{x})$ is the corresponding Bloch function which has the periodicity of the lattice, $u_{\boldsymbol{k},n}(\boldsymbol{x}) = u_{\boldsymbol{k},n}(\boldsymbol{x}+\boldsymbol{r})$. The index n here labels each band within the system. To solve the system one then has to solve for $u_{\boldsymbol{k},n}(\boldsymbol{x})$ by finding the eigenvectors of $\hat{H}(\boldsymbol{k})$ which is defined as

$$\hat{H}(\boldsymbol{k}) = e^{-i\boldsymbol{k}\cdot\boldsymbol{x}}\, \hat{H}\, e^{i\boldsymbol{k}\cdot\boldsymbol{x}}. \tag{2.2}$$

For a more in depth analysis of Bloch's theorem see [53].

The above application is to a continuous system with periodicity, but we will be concerned with tight binding models on a lattice. As such, we will adapt Bloch's theorem for the tight binding case and also introduce some useful notation that will be used later in the thesis. The methods laid out here are presented in more detail in [54]. We take the Hilbert space of our tight binding Hamiltonian to be spanned by the states

$$|\boldsymbol{m},\alpha\rangle \to |\boldsymbol{m}\rangle \otimes |\alpha\rangle \quad \in \quad \mathscr{H}_{lattice} \otimes \mathscr{H}_{internal} \tag{2.3}$$

where $|\boldsymbol{m}\rangle$ is a vector labelling the unit cell and α is a vector labelling the internal degrees of freedom within the unit cell. These states obey the normalisation conditions $\langle \boldsymbol{m}'|\boldsymbol{m}\rangle = \delta_{\boldsymbol{m}'\boldsymbol{m}}$ and $\langle \alpha'|\alpha\rangle = \delta_{\alpha'\alpha}$. Throughout this thesis we will generally label unit cells with roman numerals and internal degrees of freedom of the unit cell with Greek symbols unless otherwise stated. Here we have chosen to separate out the external degrees of freedom from the internal degrees of freedom as this will make future calculations simpler. It is important to point out that the degrees of freedom within the unit cell labelled by α covers the spin degrees of freedom and other intrinsic properties of the particles, but also includes the position within the unit cell. For our lattice system we have translational invariance in the bulk at the level of the unit cell such that

$$\langle \boldsymbol{m}|\, \hat{H}\, |\boldsymbol{n}\rangle = \langle \boldsymbol{m}+\boldsymbol{L}|\, \hat{H}\, |\boldsymbol{n}+\boldsymbol{L'}\rangle \tag{2.4}$$

where $\boldsymbol{m},\boldsymbol{n},\boldsymbol{L},\boldsymbol{L'} \in \mathbb{Z}^d$. We therefore define a normalised plane wave basis $|\boldsymbol{k}\rangle$ as

$$|\boldsymbol{k}\rangle = \frac{1}{\sqrt{V_{\mathrm{BZ}}}} \sum_{\boldsymbol{x}} e^{i\boldsymbol{x}\cdot\boldsymbol{k}}\, |\boldsymbol{x}\rangle\,. \tag{2.5}$$

Here V_{BZ} is the volume of the Brillouin zone, which is related to the volume of the unit cell by

$V_c = (2\pi)^d / V_{\mathrm{BZ}}$, where d is the dimensionality of the system. We use the normalisation convention $\langle \boldsymbol{k'} | \boldsymbol{k} \rangle = \delta(\boldsymbol{k'} - \boldsymbol{k})$ and $\langle u_{\boldsymbol{k}n} | u_{\boldsymbol{k}m} \rangle = \delta_{n,m}$, where $\delta(\boldsymbol{k'} - \boldsymbol{k})$ is the Dirac delta function and $\delta_{n,m}$ is the Kronecker delta function. We restrict $\boldsymbol{k}$ to take on values within the first Brillouin zone of the system. With this Bloch's theorem is now given by

$$|\psi_{\boldsymbol{k},n}\rangle = |\boldsymbol{k}\rangle \otimes |u_{\boldsymbol{k},n}\rangle \tag{2.6}$$

with n labelling the band and the state $|u_{\boldsymbol{k},n}\rangle \in \mathscr{H}_{internal}$ being the Bloch state with periodicity of the unit cell. To determine the Bloch states one finds the eigenvalues of the Hamiltonian $\hat{H}(\boldsymbol{k})$ given by

$$\hat{H}(\boldsymbol{k}) = \langle \boldsymbol{k} | \hat{H} | \boldsymbol{k} \rangle = \sum_{\alpha,\beta} \langle \boldsymbol{k}, \alpha | \hat{H} | \boldsymbol{k}, \beta \rangle \tag{2.7}$$

such that we have

$$\hat{H}(\boldsymbol{k}) | u_{\boldsymbol{k},n} \rangle = E_{\boldsymbol{k}} | u_{\boldsymbol{k},n} \rangle . \tag{2.8}$$

With this we can now start to define the Chern number which topologically defines insulating systems. The first step is to understand the Berry phase which we will introduce in the next section.

2.2 Discrete Case

The Berry phase was first introduced by Michael Berry in 1983 in which he showed that when a system is adiabatically evolved around a closed loop the system picks up a phase which does not return back to itself, i.e. $\gamma(0) \neq \gamma(T)$ [55]. As we will show, the Berry phase plays a crucial part in identifying topological insulating systems. For a more detailed definition we refer the reader to Berry's original paper or pedagogical introductions in [54, 23].

Just like Bloch's theorem in the previous section, the Berry phase can be defined in a discrete way and in a continuous way. Here we will first define it in the discrete way as it is slightly easier to conceptualise and then we will define it for the continuous case. As well as being slightly easier to understand, the discrete form of the Berry flux will prove useful when analysing the Bott index for the discrete case in section chapter 5.

2.2.1 Berry Phase

In quantum mechanics a system is described by the state $|\Psi\rangle$ which can have some complex phase $e^{i\phi}$. Observables of the system are required to be real values and are given by expectation values of operators $\langle \Psi | \hat{A} | \Psi \rangle$. As such, observables are not affected by this complex phase and we can therefore

choose the value of ϕ to be what we want. This is known as a gauge transformation and is defined as

$$|\Psi\rangle \quad \rightarrow \quad e^{i\phi}\,|\Psi\rangle\,. \tag{2.9}$$

Properties of the system are determined by observables and therefore these properties should also be gauge invariant. We can define the relative phase between 2 states by considering

$$e^{-i\gamma_{12}} = \frac{\langle\Psi_1|\Psi_2\rangle}{|\langle\Psi_1|\Psi_2\rangle|} \tag{2.10}$$

and then taking the argument of this complex number such that

$$\gamma_{12} = -\arg\frac{\langle\Psi_1|\Psi_2\rangle}{|\langle\Psi_1|\Psi_2\rangle|}. \tag{2.11}$$

It is important to note that the relative phase, γ_{12}, can only be defined modulo 2π seen as $e^{i\pi} = e^{i(\pi+2\pi M)}$ where $M \in \mathbb{Z}$. Performing a gauge transformation on the relative phase shows that it is not invariant under a local gauge transformation and therefore cannot describe properties of the system;

$$|\Psi_j\rangle \rightarrow e^{i\boldsymbol{\alpha_j}}\,|\Psi_j\rangle \qquad\qquad e^{-i\gamma_{12}} \rightarrow e^{-i\gamma_{12}+i(\alpha_2-\alpha_1)}. \tag{2.12}$$

Now consider a group of states arranged in a loop (see fig. 2.1). For this loop we can calculate the phase around the loop by summing the relative phases between each of the states. We will call the phase of the loop the Berry phase and label it by γ_L. We define the Berry phase in the following way

$$\gamma_L = -\arg\langle\Psi_1|\Psi_2\rangle\langle\Psi_2|\Psi_3\rangle ... \langle\Psi_N|\Psi_1\rangle = -\arg\,\mathrm{Tr}\Big[\,|\Psi_1\rangle\langle\Psi_1|\Psi_2\rangle\langle\Psi_2|\Psi_3\rangle\langle\Psi_3|...|\Psi_N\rangle\langle\Psi_N|\,\Big]. \tag{2.13}$$

In the second equality we have expressed the Berry phase in terms of projectors which are inherently gauge invariant. This then shows that the Berry phase, γ_L, is a gauge invariant quantity and could thus describe observables of the system.

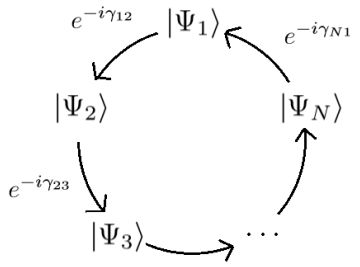

Figure 2.1: Berry phase path around a loop consisting of N states.

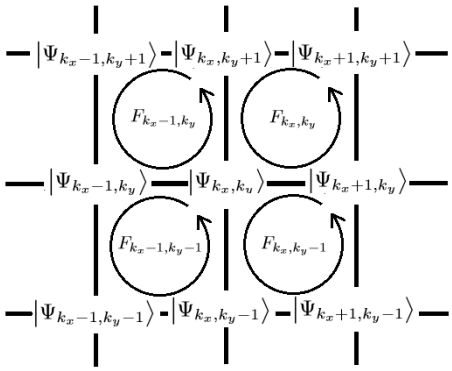

Figure 2.2: Berry flux around each plaquette for a group of states arranged in a lattice.

2.2.2 Berry Flux

In the previous section we defined the Berry phase of an object around a closed loop and showed that one can measure it by considering the projectors at each point along the loop. Here we consider a 2D lattice system and show that the Berry phase around the edge of the system can be expressed as the sum of the Berry phase around each plaquette in the system.

Consider a collection of states arranged in a square lattice and each state is labelled by 2 quantum numbers k_x and k_y (see fig. 2.2). For this system we introduce a quantity called the Berry flux defined as the Berry phase around a single plaquette (or unit square);

$$\begin{aligned} F_{k_x,k_y} &= -\arg \left\langle \Psi_{k_x,k_y} \middle| \Psi_{k_x+1,k_y} \right\rangle \left\langle \Psi_{k_x+1,k_y} \middle| \Psi_{k_x+1,k_y+1} \right\rangle \left\langle \Psi_{k_x+1,k_y+1} \middle| \Psi_{k_x,k_y+1} \right\rangle \left\langle \Psi_{k_x,k_y+1} \middle| \Psi_{k_x,k_y} \right\rangle \\ &= -\arg e^{-i\,(\gamma_{k_x,k_y} + \gamma_{k_x+1,k_y} + \gamma_{k_x+1,k_y+1} + \gamma_{k_x,k_y+1})}. \end{aligned} \tag{2.14}$$

Using the Berry fluxes we can then calculate the Berry phase along any closed path on the lattice by adding all the Berry fluxes that are contained within the closed path. This is possible because any internal edge within the closed loop will be considered twice in the summation but in the opposite direction. Using eq. (2.9) and eq. (2.10) it can be shown that the relative phase between two states depends on the direction travelled such that $\gamma_{12} = -\gamma_{21}$. Therefore, when all the Berry fluxes are summed the internal edges are neglected and we have the relation

$$e^{-i\gamma_L} = \exp\Big(-i \sum_{k_x,k_y \in L} F_{k_x,k_y} \Big) \tag{2.15}$$

where L is a closed loop on the lattice and the summation is over positions labelled by k_x and k_y that lie within the loop. It is important to note that the relation above only holds modulo 2π and therefore we can only say that the Berry flux and the Berry phase are equal up to an integer value of 2π.

2.2.3 The Chern number

As mentioned earlier, we are interested in systems with periodicity in the bulk and, as a result of this, our system has periodic boundary conditions. We therefore need to consider the lattice on a torus geometry which has an interesting effect on the Berry phase. Earlier, we stated that the Berry phase of a region can be found by summing all the Berry fluxes within that region. Therefore, if we want to find the Berry phase of the whole lattice we sum all the Berry fluxes of the lattice. Recall that the internal edges of the lattice cancel out and only the external edges are left. If we now place the lattice on a torus, interestingly, the external edges are matched and cancel each other out. As a result, the product of the Berry flux phase factors is equal to 1;

$$\prod_{k_x}\prod_{k_y} e^{-iF_{k_x,k_y}} = 1. \tag{2.16}$$

At this point it is important to stress that the above equation does not mean that $F_{k_x,k_y} = 0$, but means that $F_{k_x,k_y} = 2\pi N$ with $N \in \mathbb{Z}$. This is because the matched external edges can still cancel each other out when they differ by a value of 2π such that $e^{-i\gamma_{12}} = e^{-i(-\gamma_{21}+2\pi N)}$. Using eq. (2.16) and eq. (2.14) we now define the Chern number of the system as

$$C_1 = \frac{1}{2\pi}\sum_{k_x,k_y} F_{k_x,k_y}. \tag{2.17}$$

From the above equation we can see that the Chern number is gauge invariant, due to it being constructed from gauge invariant quantities, and is restricted to take integer values. With this we have shown that the Chern number represents a property of the system and we will show later that it can be used to distinguish 2D topological insulators from trivial insulators.

2.3 Continuous Case

In this section we define the Chern number for the continuous case. In this case we consider a system described by the states $|\Psi(\boldsymbol{k})\rangle$ where $\boldsymbol{k}$ is a vector that spans the parameter space of the system. We consider some smooth closed path in this parameter space such that all points along this path have a well defined derivative. It should be noted that while it is not always possible for the whole of the parameter space to be smooth it is always possible to perform some local gauge transformation such that all points in some local region of the parameter space are smooth.

2.3.1 Berry Phase

We first define the relative phase between two states along our closed path. We will take the states to be infinitesimally close to one another and describe their difference by $\delta\boldsymbol{k}$. Using eq. (2.10) we define the relative phase as

$$e^{-i\Delta\gamma} = \frac{\langle\Psi_{\boldsymbol{k}}|\Psi_{\boldsymbol{k}+\delta\boldsymbol{k}}\rangle}{|\langle\Psi_{\boldsymbol{k}}|\Psi_{\boldsymbol{k}+\delta\boldsymbol{k}}\rangle|}. \tag{2.18}$$

Due to the states being infinitesimally close we take the limit $\delta\boldsymbol{k} \ll 1$ and Taylor expand $|\Psi_{\boldsymbol{k}+\delta\boldsymbol{k}}\rangle$ to first order in $\delta\boldsymbol{k}$ to get

$$|\Psi_{\boldsymbol{k}+\delta\boldsymbol{k}}\rangle = |\Psi_{\boldsymbol{k}}\rangle + \delta\boldsymbol{k}\cdot\nabla_{\boldsymbol{k}}|\Psi_{\boldsymbol{k}}\rangle \tag{2.19}$$

where $\nabla_{\boldsymbol{k}}$ is the gradient operator. Acting on this from the left with $\langle\Psi_{\boldsymbol{k}}|$ we get

$$\langle\Psi_{\boldsymbol{k}}|\Psi_{\boldsymbol{k}+\delta\boldsymbol{k}}\rangle = 1 + \delta\boldsymbol{k}\cdot\langle\Psi_{\boldsymbol{k}}|\nabla_{\boldsymbol{k}}|\Psi_{\boldsymbol{k}}\rangle. \tag{2.20}$$

It can be shown that the second term is purely imaginary and therefore the magnitude of eq. (2.20) is 1. If we now Taylor expand the exponential of the Berry phase it can be shown that

$$\Delta\gamma = i\langle\Psi_{\boldsymbol{k}}|\nabla_{\boldsymbol{k}}|\Psi_{\boldsymbol{k}}\rangle\cdot\delta\boldsymbol{k} \equiv \boldsymbol{A}\cdot\delta\boldsymbol{k}. \tag{2.21}$$

to leading order in $\delta\boldsymbol{k}$. Here we have defined the vector $\boldsymbol{A} = A_x, A_y$ which is known as the Berry connection. We stated in the discrete case that the relative phase is not gauge invariant and therefore $\Delta\gamma$ shouldn't be gauge invariant either. This implies that the Berry connection should not be gauge invariant and indeed it isn't;

$$|\Psi_{\boldsymbol{k}}\rangle \to e^{-i\boldsymbol{\alpha}_{\boldsymbol{k}}}|\Psi_{\boldsymbol{k}}\rangle \qquad\qquad \boldsymbol{A} \to \boldsymbol{A} + \nabla_{\boldsymbol{k}}\boldsymbol{\alpha}_{\boldsymbol{k}} \tag{2.22}$$

where $\boldsymbol{\alpha}_{\boldsymbol{k}}$ represents a local gauge transformation.

We are now ready to define the Berry phase in the continuum case. We defined the Berry phase, in the discrete case, as the sum of all relative phases around a closed loop. In the continuum case this sum becomes an integral and we define the Berry phase as

$$\gamma(\mathscr{L}) = -\arg\, e^{-i\oint_{\mathscr{L}}\boldsymbol{A}\cdot d\boldsymbol{k}}, \tag{2.23}$$

where the integral is over the closed path $\mathscr{L}$. Just like the discrete case the Berry phase around a closed path for the continuous case is gauge invariant. This is because under a gauge transformation we pick up an additional phase that is a total derivative and therefore it will disappear when integrated

over a closed path. Again, the Berry phase is only well defined modulo 2π seen as when we take the argument of the exponential we restrict its value to between 0 and 2π.

2.3.2 Berry Flux

In the previous section we showed that the Berry phase involves integrating a gauge dependent quantity known as the Berry connection. Therefore it would nice if we could define the Berry phase in terms of gauge invariant quantities like in the discrete case. This can be done by using Stokes theorem which states that one can rewrite an integral over a closed path as the integral over the surface bounded by the closed path. Using this we get that

$$\oint_{\mathscr{L}} d\boldsymbol{k} \cdot \boldsymbol{A} = \int_{\mathscr{R}} d\boldsymbol{S} \cdot \boldsymbol{B} \qquad\qquad \boldsymbol{B} \equiv \nabla_{\boldsymbol{k}} \times \boldsymbol{A} \tag{2.24}$$

where $\mathscr{R}$ is the region enclosed by $\mathscr{L}$ and $d\boldsymbol{S}$ is an infinitesimal surface element. The object $\boldsymbol{B}$ is known as the Berry curvature. It can be shown that the Berry curvature is gauge invariant by noting that $\nabla \times (\nabla f) = 0$ and therefore the extra term that arises from the gauge transformation will disappear. There is a subtlety in using Stokes' theorem here which is that it can only be applied if the region $\mathscr{R}$ is smooth. This can be achieved by separating $\mathscr{R}$ into smaller sections and performing a gauge transformation on each small section such that it is locally smooth. One can then find the Berry flux of $\mathscr{R}$ by summing all the contributions from the smaller sections. We can thus rewrite the Berry phase as

$$\gamma(\mathscr{L}) = -\arg\, e^{-i \int_{\mathscr{R}} d\boldsymbol{S} \cdot \boldsymbol{B}}. \tag{2.25}$$

In the 2D case $d\boldsymbol{S} \cdot \boldsymbol{B}$ reduces to $dk_x dk_y\, B(k_x, k_y)$.

2.3.3 Chern number

We are now ready to define the Chern number for the continuous case in 2D. As stated before we are interested in periodic crystals and therefore we consider a toroidal geometry represented by $\mathscr{T}$. Just like in the discrete case, when we consider a toroidal geometry we have that

$$e^{-i\gamma(\mathscr{L})} = e^{-i \int_{\mathscr{T}} d\boldsymbol{k}\, B} = 1 \tag{2.26}$$

which restricts the integral of the Berry flux to an integer value multiplied by 2π. This can be seen by noting that the continuous case is equivalent to the discrete case when the lattice spacing is tends to zero and therefore the above equation also applies to the continuous case. In eq. (2.26) we have used the short hand notation $\int d\boldsymbol{k} \equiv \int dk_x dk_y$ for convenience; we will used this notation from here on out.

For a more in depth discussion of this please refer to [23].

The Chern number of the system is then defined as the integral of the Berry flux over the torus;

$$C_1 = \frac{1}{2\pi}\int_{\mathscr{T}} d\boldsymbol{k}\, B. \tag{2.27}$$

From eq. (2.26) it can be seen that the Chern number of a system has to be an integer value due to the fact that the integral of the Berry flux over a torus is required to be an integer value multiplied by 2π.

For 2D periodic systems the torus structure represents the Brillouin zone and we can write the Chern number of a specific band as

$$C_1^n = \frac{i}{2\pi}\int_{BZ} d\boldsymbol{k}\Big(\langle \partial_{k_x} u_{\boldsymbol{k},n} | \partial_{k_y} u_{\boldsymbol{k},n}\rangle - \langle \partial_{k_y} u_{\boldsymbol{k},n} | \partial_{k_x} u_{\boldsymbol{k},n}\rangle \Big) \tag{2.28}$$

where the subscript n labels the band considered and the integral is taken over the Brillouin zone. To determine the Chern number of the system one sums the Chern numbers for each populated band.

2.3.4 Alternate Form of the Berry Curvature

There is another form of the Berry curvature which is very useful when calculating it numerically. To see why there is a problem in calculating the Berry curvature using the previous definitions let us look at the Berry curvature when we have a state $|u_{\boldsymbol{k}n}\rangle$ for a 2D system;

$$B^n = \nabla_{\boldsymbol{k}} \times i \langle u_{\boldsymbol{k}n}| \nabla_{\boldsymbol{k}} |u_{\boldsymbol{k}n}\rangle = i\big(\langle \partial_{k_x} u_{\boldsymbol{k}n} | \partial_{k_y} u_{\boldsymbol{k}n}\rangle - \langle \partial_{k_y} u_{\boldsymbol{k}n} | \partial_{k_x} u_{\boldsymbol{k}n}\rangle \big) \tag{2.29}$$

where $\langle \partial_{k_i} u_{\boldsymbol{k}n}| = \partial_{k_i}(\langle u_{\boldsymbol{k}n}|)$. From eq. (2.29) we can see that there are derivatives on the eigenvalues of $\hat{H}(\boldsymbol{k})$. When working numerically the states are in discrete form which can make differentiating them more complicated. It would be better if the derivatives were on another object that we can evaluate analytically which in this case is the Hamiltonian. We can write equation (2.29) as

$$B^n = i\sum_{n'\neq n}\Big(\langle \partial_{k_x} u_{\boldsymbol{k}n} | u_{\boldsymbol{k}n'}\rangle \langle u_{\boldsymbol{k}n'} | \partial_{k_y} u_{\boldsymbol{k}n}\rangle - \langle \partial_{k_y} u_{\boldsymbol{k}n} | u_{\boldsymbol{k}n'}\rangle \langle u_{\boldsymbol{k}n'} | \partial_{k_x} u_{\boldsymbol{k}n}\rangle \Big), \tag{2.30}$$

where we have used the fact that $\sum_{n'} |u_{\boldsymbol{k}n'}\rangle \langle u_{\boldsymbol{k}n'}| = \mathbb{1}$. The $n' = n$ term is neglected because it can be shown to be zero using $\langle u_{\boldsymbol{k}n'} | u_{\boldsymbol{k}n}\rangle = \delta_{n'n}$ and $\langle \partial_{k_i} u_{\boldsymbol{k}n'} | u_{\boldsymbol{k}n}\rangle = -\langle u_{\boldsymbol{k}n'} | \partial_{k_i} u_{\boldsymbol{k}n}\rangle$. If we now consider the Hamiltonian acting on a state

$$\hat{H}(\boldsymbol{k}) |u_{\boldsymbol{k}n}\rangle = E_{\boldsymbol{k}n} |u_{\boldsymbol{k}n}\rangle; \tag{2.31}$$

$$(\partial_{k_i}\hat{H}(\boldsymbol{k}))\,|u_{\boldsymbol{k}n}\rangle + \hat{H}(\boldsymbol{k})\,|\partial_{k_i}u_{\boldsymbol{k}n}\rangle = (\partial_{k_i}E_{\boldsymbol{k}n})\,|u_{\boldsymbol{k}n}\rangle + E_{\boldsymbol{k}n}\,|\partial_{k_i}u_{\boldsymbol{k}n}\rangle\,; \tag{2.32}$$

$$\langle u_{\boldsymbol{k}n'}|\,\partial_{k_i}\hat{H}(\boldsymbol{k})\,|u_{\boldsymbol{k}n}\rangle + \langle u_{\boldsymbol{k}n'}|\,\hat{H}(\boldsymbol{k})\,|\partial_{k_i}u_{\boldsymbol{k}n}\rangle = E_{\boldsymbol{k}n}\,\langle u_{\boldsymbol{k}n'}|\partial_{k_i}u_{\boldsymbol{k}n}\rangle\,. \tag{2.33}$$

In the third equality we have acted from the left with state $\langle u_{\boldsymbol{k}n'}|$ where $n' \neq n$. Due to the Hamiltonian being Hermitian we can act with it to the left or the right and we will get the same answer. As such, acting to the left with $\hat{H}(\boldsymbol{k})$ in equation (2.33) we get that

$$\langle u_{\boldsymbol{k}n'}|\partial_{k_i}u_{\boldsymbol{k}n}\rangle = \frac{\langle u_{\boldsymbol{k}n'}|\,\partial_{k_i}\hat{H}(\boldsymbol{k})\,|u_{\boldsymbol{k}n}\rangle}{E_{\boldsymbol{k}n} - E_{\boldsymbol{k}n'}} \tag{2.34}$$

The above equation can then be used to rewrite the Berry curvature as

$$B^n = i\sum_{n'\neq n}\frac{\langle u_{\boldsymbol{k}n}|\,\partial_{k_x}\hat{H}(\boldsymbol{k})\,|u_{\boldsymbol{k}n'}\rangle\,\langle u_{\boldsymbol{k}n'}|\,\partial_{k_y}\hat{H}(\boldsymbol{k})\,|u_{\boldsymbol{k}n}\rangle}{(E_{\boldsymbol{k}n} - E_{\boldsymbol{k}n'})^2} - \frac{\langle u_{\boldsymbol{k}n}|\,\partial_{k_y}\hat{H}(\boldsymbol{k})\,|u_{\boldsymbol{k}n'}\rangle\,\langle u_{\boldsymbol{k}n'}|\,\partial_{k_x}\hat{H}(\boldsymbol{k})\,|u_{\boldsymbol{k}n}\rangle}{(E_{\boldsymbol{k}n} - E_{\boldsymbol{k}n'})^2}. \tag{2.35}$$

Inputting this new form of the Berry curvature into the definition for the Chern number we get that the Chern number can be written as

$$C_1^n = -\frac{i}{2\pi}\int_{BZ}d\boldsymbol{k}\sum_{n'\neq n}\left[\frac{\langle u_{\boldsymbol{k}n}|\,\partial_{k_x}\hat{H}(\boldsymbol{k})\,|u_{\boldsymbol{k}n'}\rangle\,\langle u_{\boldsymbol{k}n'}|\,\partial_{k_y}\hat{H}(\boldsymbol{k})\,|u_{\boldsymbol{k}n}\rangle}{(E_{\boldsymbol{k}n} - E_{\boldsymbol{k}n'})^2} - \frac{\langle u_{\boldsymbol{k}n}|\,\partial_{k_y}\hat{H}(\boldsymbol{k})\,|u_{\boldsymbol{k}n'}\rangle\,\langle u_{\boldsymbol{k}n'}|\,\partial_{k_x}\hat{H}(\boldsymbol{k})\,|u_{\boldsymbol{k}n}\rangle}{(E_{\boldsymbol{k}n} - E_{\boldsymbol{k}n'})^2}\right]. \tag{2.36}$$

This form of the Chern number is important in proving the relationship between the Hall conductivity and the Chern number [5, 8]. To see this we will look at the form of the Hall conductance. From linear response theory it can be shown that the Hall conductance of a single band in a 2D lattice system is given by [8]

$$\sigma_{xy}^n = i\hbar\sum_{n'\neq n}\int_{BZ}\frac{d\boldsymbol{k}}{(2\pi)^2}\frac{\langle u_{\boldsymbol{k}n}|\,\hat{J}_y\,|u_{\boldsymbol{k}n'}\rangle\,\langle u_{\boldsymbol{k}n'}|\,\hat{J}_x\,|u_{\boldsymbol{k}n}\rangle - \langle u_{\boldsymbol{k}n}|\,\hat{J}_x\,|u_{\boldsymbol{k}n'}\rangle\,\langle u_{\boldsymbol{k}n'}|\,\hat{J}_y\,|u_{\boldsymbol{k}n}\rangle}{(E_{\boldsymbol{k}n'} - E_{\boldsymbol{k}n})^2}. \tag{2.37}$$

Here $\hat{J}_x$ and $\hat{J}_y$ are current operators in the x and y directions respectively and n labels the bands of the system. This looks very similar to eq. (2.36). If we then define the current operator in the following way

$$\hat{\boldsymbol{J}} = \frac{e}{\hbar}\frac{\partial\hat{H}(\boldsymbol{k})}{\partial\boldsymbol{k}} \tag{2.38}$$

and input this into eq. (2.37) we get

$$\sigma_{xy}^{n} = \frac{i\,e^2}{(2\pi)^2\hbar} \sum_{n'\neq n} \int_{BZ} d\boldsymbol{k} \left[\frac{\langle u_{\boldsymbol{k}n} | \, \partial_{k_y} \hat{H}(\boldsymbol{k}) \, | u_{\boldsymbol{k}n'} \rangle \, \langle u_{\boldsymbol{k}n'} | \, \partial_{k_x} \hat{H}(\boldsymbol{k}) \, | u_{\boldsymbol{k}n} \rangle}{(E_{\boldsymbol{k}n'} - E_{\boldsymbol{k}n})^2} - \frac{\langle u_{\boldsymbol{k}n} | \, \partial_{k_x} \hat{H}(\boldsymbol{k}) \, | u_{\boldsymbol{k}n'} \rangle \, \langle u_{\boldsymbol{k}n'} | \, \partial_{k_y} \hat{H}(\boldsymbol{k}) \, | u_{\boldsymbol{k}n} \rangle}{(E_{\boldsymbol{k}n'} - E_{\boldsymbol{k}n})^2} \right] \tag{2.39}$$

where $\partial_{k_i} = \frac{\partial}{\partial k_i}$. Finally, if we compare this to eq. (2.36) we get that

$$\sigma_{xy}^{n} = \frac{-e^2}{2\pi\hbar}\, C_1^n. \tag{2.40}$$

To find the conductance for the whole system one just sums up the conductance of each populated band of the system. This relationship is known as the TKNN formula and was shown by Thouless, Kohomoto, Nightingale and den Nijs [5].

2.4 The Diophantine equation

We have previously defined the Chern number for the discrete case and the continuous case. However, there is another way in which one can determine the Chern number for topological systems with an applied magnetic field. It was shown by Thouless *et al.* that the Chern number of a system with an applied magnetic field obeys a Diophantine equation of the form [5]

$$r \;=\; C_r p \;+\; t_r q. \tag{2.41}$$

Above, r labels the band gap; t_r is restricted to take on integer values; and C_r is the Chern number of the system. The values p and q describe the applied magnetic field per unit cell Φ in terms of $\Phi_0 = 2\pi\hbar/e$ in the following way

$$\Phi \;=\; \frac{p}{q}\,\Phi_0 \tag{2.42}$$

where p and q are integers. In this case q determines the number of bands within the system. For specific models the magnitude of C_r is restricted to lie between two values when p and q take on integer values. In our case we are interested in the Aubry-André mode and the Harper-Hofstadter model and for these models the Chern number is restricted by

$$0 \;\leq\; |C_r| \;\leq\; \frac{q}{2}. \tag{2.43}$$

Using the Diophantine equation one can determine the Chern number of the system analytically and not have to worry about the possible complications from numerics. We will use the Diophantine equation frequently throughout this thesis. The Chern number of the rth band is given by $C_r - C_{r-1}$.

It is worth mentioning briefly that when p/q is set to an irrational value one can approximate the irrational value as a rational one with large p and q. As such, the Diophantine equation can still be used to determine the Chern number in this case as long as p and q take on large enough values. In this case the Chern number is not restricted and can take on any value seen as the irrational value is only truly achieved when $q \to \infty$. We will look more at the case where p/q is an irrational value when we consider quasicrystals later in the thesis.

2.5 Second Chern number

Within this thesis we will look at both 3D time-dependent systems and 4D systems. The topological structure of such systems is represented by the second Chern number and therefore we introduce it in this section.

Earlier we defined the first Chern number for a 2D system in the following way

$$C_1 = \frac{1}{2\pi} \sum_n \int_{\mathrm{BZ}} d\boldsymbol{k}\; B^n = \frac{1}{2\pi} \sum_n \int_{\mathrm{BZ}} d\boldsymbol{k} \left(\partial_{k_x} \boldsymbol{A}_y^n - \partial_{k_y} \boldsymbol{A}_x^n \right) \tag{2.44}$$

where $\boldsymbol{B}^n$ is the Berry curvature for the nth band and $\boldsymbol{A}_j^n$ is the Berry connection for the nth band in the jth direction. Using this notation the second Chern number is defined in the following way [24]

$$C_2 = \frac{1}{32\pi^2} \int_{\mathrm{BZ}} d\boldsymbol{k}\; \epsilon^{ijkl}\; \mathrm{Tr}\Big(\boldsymbol{F}_{ij}\; \boldsymbol{F}_{kl} \Big) \tag{2.45}$$

with

$$\boldsymbol{F}_{ij} = \partial_i \boldsymbol{A}_j^{nm} - \partial_j \boldsymbol{A}_i^{nm} + i\,[\boldsymbol{A}_i^{nm}\,,\, \boldsymbol{A}_j^{nm}]. \tag{2.46}$$

In the above equations ϵ^{ijlk} is the 4D Levi-Civita symbol and we have used the Einstein summation notation for the indices i, j, k, l. In eq. (2.46) n and m label the occupied bands and $\boldsymbol{A}_i^{nm} = i \langle u_{kn} | \partial_{k_i} | u_{km} \rangle$. The trace in eq. (2.45) then traces over the labels n and m. Note that strictly speaking one should define the Chern number for 2D systems as a trace over the Berry connection given in eq. (2.46). In this case the commutator disappears due to the trace of a commutator being zero and we arrive at the definition given in eq. (2.44). However, once the commutator is multiplied by something else it no longer disappears when traced over and thus it has to be included in the definition of the second Chern number.

With this we have defined the second Chern number which determines the topological index of

3D time-dependent systems and 4D systems. We will use this definition later when we define the 3D marker as well as when we investigate the topology of a 3D time-dependent Hamiltonian.

2.6 Edge state modes

So far we have stated that topological states can be distinguished from trivial states by analysing the Chern number of the system. But how does this topological difference affect the system, if at all? And if it does, what is the relation between this phenomenon and the Chern number? The answers to these questions lie within the analysis of edge state modes and the bulk boundary correspondence. To explore these questions we first need to look at what edge state modes are.

Edge state modes are special eigenstates of topological Hamiltonians that traverse the band gap of the system. These eigenstates are exponentially localised on the edges of 2D systems, the ends of 1D systems and the surface of 3D systems. As such, the edge state modes are only visible when the Hamiltonian has open boundary conditions. Examples of edge state modes can be seen in fig. 3.1.

It is possible to see that the eigenstates at the edges of a 2D system play a special role even from a semi-classical perspective. Consider a set of electrons on a two dimensional surface with a magnetic field applied perpendicular to the 2D surface. All electrons undergo cyclotron motion, but the electrons at the edge of the system have half of their path obstructed (see Figure 2.3). Due to this these electrons collide with the wall and skip around the edge of the sample resulting in edge modes circulating in a specific direction.

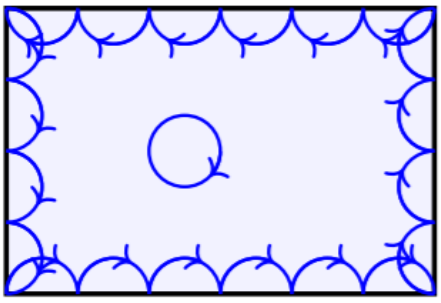

Figure 2.3: Illustration of skipping orbits for a charged particle in a uniform magnetic field. In the bulk, the semi-classical dynamics of a wave packet leads to a circular cyclotron orbit. The reflection of such an orbit from the (hard wall) edge leads to a skipping motion around the sample edge. This figure was take from [1].

While this argument is semi-classical it can be shown quantum mechanically that edge state modes circle around the edge of a 2D system. It can also be shown that a 1D time-dependant system pumps a quantised amount of charge across the system over a full time period. We show both cases below.

We will first show that when a 1D time-dependent system is topological in nature it displays a

quantized current when the system is adiabatically evolved, despite it being an insulator. We start by analysing the current operator for a single band in a 1D system with periodic boundary conditions. Using eq. (2.38) we have

$$\begin{aligned}\langle J(t)\rangle &= \frac{e}{\hbar}\frac{1}{2\pi}\int_{BZ} dk\, \langle u_{kn}(t)|\, \partial_k \hat{H}(k)\, |u_{kn}(t)\rangle \\ &= \frac{e}{\hbar}\frac{1}{2\pi}\int_{BZ} dk \Big(\partial_k \big[\, \langle u_{kn}(t)|\, \hat{H}(k)\, |u_{kn}(t)\rangle \,\big] - \langle \partial_k u_{kn}(t)|\hat{H}(k)\, |u_{kn}(t)\rangle \\ &\qquad\qquad - \langle u_{kn}(t)|\, \hat{H}(k)\, |\partial_k u_{kn}(t)\rangle \Big).\end{aligned} \tag{2.47}$$

The first term is a total derivative and therefore when integrated over the Brillouin zone it gives zero. If we now use the time-dependent Schrödinger equation for our Bloch states, $i\hbar\, |\partial_t u_{kn}\rangle = \hat{H}(k)\, |u_{kn}\rangle$, and its hermitian conjugate we get

$$\langle J(t)\rangle = \frac{ie}{2\pi}\int_{BZ} dk \Big(\langle \partial_t u_{kn}(t)|\partial_k u_{kn}(t)\rangle - \langle \partial_k u_{kn}(t)|\partial_t u_{kn}(t)\rangle \Big). \tag{2.48}$$

At this point we restrict our system to be periodic in time such that $\hat{H}(0) = \hat{H}(T)$ where T is the time period of the system; this is equivalent to making a 2D system periodic in a chosen direction. With this we now integrate both sides of the above equation over a full time period T to get

$$Q = \frac{ie}{2\pi}\int_0^T dt \int_{BZ} dk \Big(\langle \partial_t u_{kn}(t)|\partial_k u_{kn}(t)\rangle - \langle \partial_k u_{kn}(t)|\partial_t u_{kn}(t)\rangle \Big). \tag{2.49}$$

Above, Q is the amount of electric charge flowing through the system over a time period T. Noticing that the time integral and the crystal momentum integral are both closed integrals the above equation looks a lot like the Chern number given in eq. (2.28). As a result, the amount of charge pumped through a 1D time-dependent topological system over a full time period of the system is quantized and we have

$$Q = e\, C_1^n. \tag{2.50}$$

For systems with multiple bands occupied the amount of charge flowing through the system is given by the summation of the Chern numbers for each band multiplied by the charge of the electron. We have thus shown that 1D time-dependent topological systems display quantized pumping effects. This was first shown by Thouless in his paper "Quantization of particle transport" [9].

To consider the 2D case we will consider the 1D time-dependent case and promote the time variable, t, to the crystal momentum variable in the y direction, k_y. Doing this the system now becomes a 2D system with a magnetic field applied perpendicular to its surface (i.e. the system considered earlier for the semi-classical case). This also means that the system is infinite in the y direction and finite in

the x direction. To calculate the current on the edges of the system we can consider the gradient of the edge state modes localised on each side of the system. The easiest way to do this is to consider the energy-spectrum of the system for varying k_y. Doing this it can be seen that the gradient of the right edge state mode is non-zero and positive and the gradient of the left edge state mode is the same as the right but negative (see fig. 3.1). The current along the infinite y edge is given by the gradient of the edge state modes, $\hat{J}_y = \frac{e}{\hbar}\partial_{k_y}\hat{H}(\boldsymbol{k})$. As such, the right edge state mode propagates up in the y direction along the right edge and the left edge state mode propagates down the left edge in the y direction. With this we have shown that the edge state modes propagate along the edge of the system for a 2D topological system. As well as this, the number of propagating edge state modes is determined by the Chern number of the system; this is known as the bulk boundary correspondence [56, 57]. This effect has been observed experimentally in many different ways; for more information on experimental techniques to observe this phenomena we refer the reader the the following reviews [58, 59, 60].

3

Topological Insulator Models

Now that we have established how to analyse the topological index of a system and looked at how topological structure affects different systems we are now ready to introduce the topological insulator models that will be considered within this thesis. The Hamiltonians that we will analyse are the 1D time dependent Aubry-André model; the 2D Harper-Hofstadter model; a 3D time-dependent Hamiltonian which is a combination of the Aubry-André model and the Harper-Hofstadter model; and a quasicrystal Hamiltonian which we call the Rice-Mele quasicrystal Hamiltonian. We start by introducing the 1D Aubry-André model, stating its topological index and showing its energy spectrum. We then introduce the 2D Harper-Hofstadter model and show that it is topologically equivalent to the Aubry-André model. We also show the energy spectrum of this model with open boundary conditions to demonstrate the bulk boundary correspondence. After this, we construct a 3D time-dependent Hamiltonian using the Aubry-André model and the Harper-Hofstadter model, stating its topological index and showing its energy spectrum for both periodic boundary conditions and open boundary conditions. Finally, we introduce the Rice-Mele quasicrystal model.

3.1 Aubry-André model

In this section we introduce the Aubry-André (AA) model, which can also be known as the Harper model or the Aubry-André-Harper model. The time-dependent Aubry-André model is a non-interacting model with a Hamiltonian given by [61, 62]

$$\hat{H}_{AA} = -J\sum_{n}(|n\rangle\langle n+1| + \text{h.c.}) - \Delta\sum_{n}\cos\big(2\pi bn - \phi(t)\big)\,|n\rangle\langle n|\,. \tag{3.1}$$

The first term describes simple hoppings between lattice sites and the second term describes an on-site energy which is time-dependent. The value Δ sets the maximum and minimum value of the on-site energy. The quantity n takes on integer values which label the lattice sites of the system and the time dependence of the system enters through the on-site phase via $\phi(t) = 2\pi t/T$, where T is the period of the potential.

The value $b = p/q$ determines whether the periodicity of the potential aligns with the periodicity of the lattice. In the case where p and q take on integer values the periodicity of the potential is equal to q times that of the lattice; this is known as the commensurate case. For the case where the values of p or q, or both, are irrational the periodicity of the potential can not align with that of the lattice; this is known as the incommensurate case. It was shown that for the incommensurate case where $b = 2/(1+\sqrt{5})$ the AA model has the same topology as the Fibonacci quasicrystal [14]. Because of this the incommensurate AA model is used to study the topological structure of quasicrystal systems.

We will consider the commensurate case $b = p/q$ for now and discuss the incommensurate quasicrystal case later in the thesis. In the commensurate case the unit cell is extended to encompass q lattice sites so that the system can be written as Bloch periodic. In this case we can relabel the lattice in the following way $|n\rangle = |x\rangle \otimes |\alpha\rangle$. Here the state $|\alpha\rangle$ labels the q lattice sites within the unit cell and $|x\rangle$ labels the unit cell. Note that the states $|\alpha\rangle$ can also label other internal degrees of freedom within the unit cell like spin etc., however, for simplicity we neglect them here. Because the system is periodic in x we introduce the plane wave basis states $|k\rangle = \frac{1}{\sqrt{V_{\text{BZ}}}}\sum_k e^{ikx}|x\rangle$ where V_{BZ} is the volume of the Brillouin zone. Using the new definition of the states $|n\rangle$ as well as the plane wave basis states we can rewrite the AA model as

$$\begin{aligned}\hat{H}_{AA} = \sum_{k}|k\rangle\langle k| \otimes \Bigg[&- J\Big(\sum_{\alpha=0}^{q-2}|\alpha+1\rangle\langle\alpha| + e^{ik}|\alpha=0\rangle\langle\alpha=q-1| + h.c.\Big) \\ &- \Delta\sum_{\alpha=0}^{q-1}\cos\big(2\pi b\hat{\alpha} - \phi(t)\big)\,|\alpha\rangle\langle\alpha|\Bigg].\end{aligned} \tag{3.2}$$

Above we have defined $\hat{\alpha} = \mathbb{1}\otimes\sum_\alpha \alpha\,|\alpha\rangle\langle\alpha|$ where $\alpha \in \{0,1,2,..,q-1\}$. The term in the large square

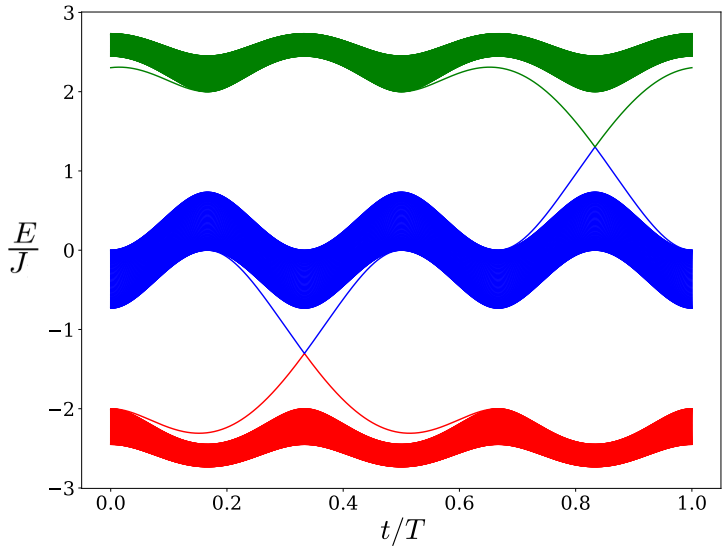

Figure 3.1: The energy spectrum for the non-interacting Aubry-André model with open boundary conditions. The parameters of the model have been set to $\Delta/J = -2$ and $b_1 = 1/3$. The red band labels the lowest N/3 states, the green band labels the highest N/3 states and the blue band labels the remaining N/3 states; where N is the total number of states in the system.

brackets is the Bloch Hamiltonian and is labelled $\hat{H}_{AA}(k)$. As stated earlier, the eigenvectors of the Bloch Hamiltonian give the cell-periodic part of the Bloch states, $|u_{kn}\rangle$.

In Figure 3.1 the energy spectrum of the non-interacting Aubry-André model is shown. We have set $b = 1/3$ and used open boundary conditions to show the edge state modes that traverse between the bands. The colouring of the bands within the energy spectrum indicates how we define the bands of the system. This way each band always contains N/q states, where N is the total number of states and q is the total number of internal degrees of freedom.

If periodic boundary conditions are taken, so that the bands are gapped at all times, it can be shown that the Chern number of each band in Figure 3.1 are as follows; the bottom band has a Chern number of 1, the middle band has a Chern number of -2, and the top band has a Chern number of 1. This can also be show using the Diophantine equation. We stated earlier that for a 1D time-dependent topological system the Chern number determines the amount of electric charge pumped through a system per time cycle. From this, we then expect that if only the bottom band of the system is populated then one unit of electric charge will be transmitted through the system per time cycle.

3.2 Harper-Hofstadter model

Next, we analyse the Harper-Hofstadter (HH) model and show that it has the same Bloch Hamiltonian as the Aubry-André model. Due to this, the Harper-Hofstadter model has the same topological properties as the Aubry-André model. The Hamiltonian of the Harper-Hofstadter model is given by

$$\hat{H}_{HH} = \sum_{n,m} \Big(- J' \left|n, m+1\right\rangle \left\langle n, m\right| - \Delta' \, e^{-i2\pi b' m} \left|n+1, m\right\rangle \left\langle n, m\right| + h.c. \Big) \tag{3.3}$$

where n and m label the lattice sites in the x and y directions respectively. The first term above describes lattice hoppings in the y-direction. The second term describes lattice hoppings in the x-direction with a phase factor dependent on the lattice position in the y-direction. In this model the value of $b' = p/q$ represents an applied magnetic flux per unit cell perpendicular to the system in units of $\Phi_0 = 2\pi\hbar/e$ [61, 8, 1]. This extends the periodicity in the y direction to that of q times the lattice spacing. When p and q are integers the unit cell is extended such that it encompass q lattice sites in the y direction. Now we know the periodicity of the Harper-Hofstadter Hamiltonian we can write its Hamiltonian in Bloch form and compare it to the Bloch form found for the Aubry-André model, assuming that p and q take on integer values.

We can rewrite $\hat{H}_{HH}$ in a slightly different form by using $\left|n, m\right\rangle = \left|\boldsymbol{x}\right\rangle \otimes \left|\alpha\right\rangle$ where $\boldsymbol{x} = \{x, y\}$ labels the unit cell position and α labels the internal degrees of freedom of the unit cell. Using this we get that

$$\begin{aligned} \hat{H}_{HH} = -J' \sum_{\boldsymbol{x}} \left[\left(\sum_{\alpha=0}^{q-2} \left|\boldsymbol{x}\right\rangle \left\langle \boldsymbol{x}\right| \otimes \left|\alpha+1\right\rangle \left\langle \alpha\right| \right) + \left|\boldsymbol{x} + \mathbf{e}_y\right\rangle \left\langle \boldsymbol{x}\right| \otimes \left|\alpha = 0\right\rangle \left\langle \alpha = q-1\right| \right] + h.c. \\ -\Delta' \sum_{\boldsymbol{x}} \sum_{\alpha=0}^{q-1} e^{-i2\pi b' \hat{\alpha}} \left|\boldsymbol{x} + \mathbf{e}_x\right\rangle \left\langle \boldsymbol{x}\right| \otimes \left|\alpha\right\rangle \left\langle \alpha\right| + h.c. \end{aligned} \tag{3.4}$$

Above, $\mathbf{e}_i$ is a vector in the ith direction with a length of the lattice spacing in the ith direction. The states $\left|\alpha = 0\right\rangle$ and $\left|\alpha = q-1\right\rangle$ represent the first and last lattice site in the unit cell respectively and the operator $\hat{\alpha}$ is defined as in the previous section. Therefore, in the above equation we have that the first term represents hoppings within the unit cell; the second term represents hoppings between unit cells in the y direction and the third term represents hoppings between unit cells in the x direction. If we now use the plane wave basis states $\left|\boldsymbol{k}\right\rangle = \frac{1}{\sqrt{V_{\mathrm{BZ}}}} \sum_{\boldsymbol{k}} e^{i\boldsymbol{k}\cdot\boldsymbol{x}} \left|\boldsymbol{x}\right\rangle$, where $\boldsymbol{k} = \{k_x, k_y\}$, in the above

equation we get that

$$\hat{H}_{HH} = \sum_{\boldsymbol{k}} |\boldsymbol{k}\rangle \langle \boldsymbol{k}| \otimes \Big[- J' \Big(\sum_{\alpha=0}^{q-2} |\alpha+1\rangle \langle \alpha| + e^{ik_y} |\alpha = 0\rangle \langle \alpha = q-1| + h.c. \Big) \\ - 2\Delta' \sum_{\alpha=0}^{q-1} \cos\big(2\pi b' \hat{\alpha} - k_x\big) |\alpha\rangle \langle \alpha| \Big] \tag{3.5}$$

Comparing eq. (3.2) and eq. (3.5) it is clear that the Bloch Hamiltonians of the Harper-Hofstadter model and the Aubry-André model are identical if $J = J'$, $\Delta = 2\Delta'$ and $b = b'$; here we identify k_x with the phase $\phi(t)$ from the AA model. Therefore, when these conditions are met, the models have the same Bloch Hamiltonian and are therefore topologically identical meaning the bands have the same Chern numbers.

3.3 3D topological model

Now we have defined the Aubry-André model and the Harper-Hofstadter model we can now develop a 3D time-dependent topological pumping model. We will use this model later to show that one can generate a real-space local topological marker for 3D time-dependent systems which gives the second Chern number of the system.

It has been shown that for a Hamiltonian that decouples in the following way

$$\hat{H} = \hat{H}_a \otimes \mathbb{1} + \mathbb{1} \otimes \hat{H}_b \tag{3.6}$$

the second Chern number of this system is given by the product of the first Chern numbers of $\hat{H}_a$ and $\hat{H}_b$ [27]. Therefore, we define our 3D Hamiltonian by using eq. (3.6) and setting $\hat{H}_a$ equal to the Harper-Hofstadter model and $\hat{H}_b$ equal to the Aubry-André model. Doing this our 3D Hamiltonian is given by

$$\hat{H}_{3D}(t) = \sum_{\boldsymbol{x}} \Big[\Big(- J' \, |\boldsymbol{x} + e_y\rangle \langle \boldsymbol{x}| - \Delta' \, e^{-i2\pi by} |\boldsymbol{x} + \mathbf{e}_x\rangle \langle \boldsymbol{x}| \\ - J(|\boldsymbol{x}\rangle \langle \boldsymbol{x} + \mathbf{e}_z| + \text{h.c.}) \Big) - \Delta \cos\big(2\pi bz - \phi(t)\big) |\boldsymbol{x}\rangle \langle \boldsymbol{x}| \Big]. \tag{3.7}$$

Above $\boldsymbol{x} = \{x, y, z\}$ labels the lattice points and e_i is a vector in the ith direction with a length of the lattice spacing in the ith direction.

Figure 3.2 shows the energy spectrum of $\hat{H}_{3D}$ with periodic boundary conditions for specific values $k_z a_z = \pi/3$ and $\phi(t) = \pi/2$. We have set $b = b' = 1/3$ which extends the unit cell such that it contains 9 lattice sites and thus 9 energy bands in the energy spectrum. From Figure 3.2 it can be seen that both the bottom band and the top band are separated from all other bands. It can be shown that

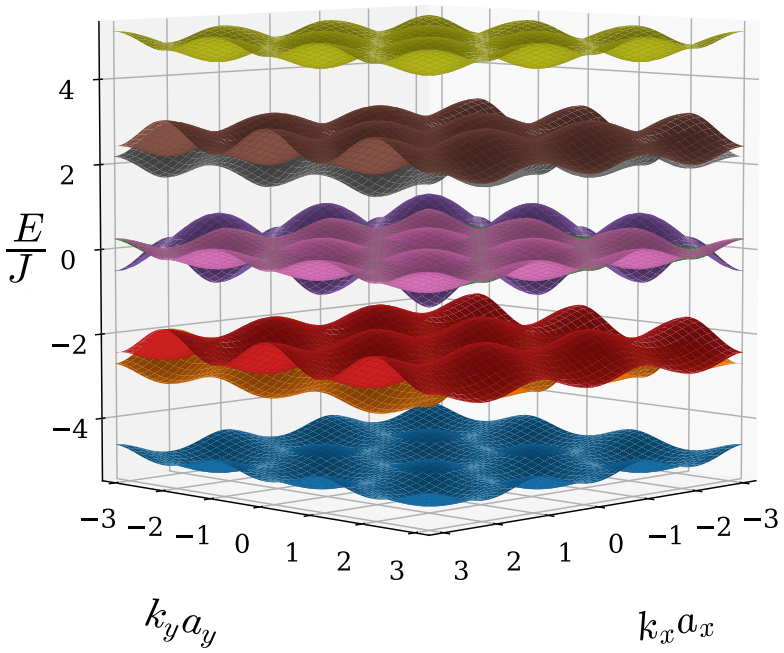

Figure 3.2: The energy spectrum for $\hat{H}_{3D}(t)$ with $k_z = \pi/3$ and $\phi(t) = \pi/2$ where a_x, a_y, a_z are the lattice constants of the system. We have used periodic boundary conditions and set the Brillouin zone to run from $-\pi$ to π in all spatial directions. The parameters have been set to $J/J' = 1$, $\Delta'/J = -1$, $\Delta/J = -2$ and $b = b' = 1/3$.

these bands remain gapped for all values $k_z a_z$ and $\phi(t)$ and, as such, the second Chern number is well defined for these bands. Due to the decoupled nature of $\hat{H}_{3D}$, the second Chern number of the bottom band is given by the product of the first Chern number of the bottom band of the Harper-Hofstadter model and the first Chern number of the bottom band of the Aubry-André model. As such, the second Chern number of the bottom band of $\hat{H}_{3D}$ is 1.

In fig. 3.3 we display the energy spectrum of $\hat{H}_{3D}$ with open boundary conditions. Figure 3.3a displays the energy spectrum with each line coloured to indicate the probability of finding it on the surface of the system. From this figure it is clear that only surface modes lie within or traverse the band gaps of the system. Figure 3.3b displays the same energy spectrum but colours the lines to indicate if it lies on an xz or yz surface plane. This figure shows that most of the modes traversing the band gap from one band to another are located on the xy surface planes of the system. This is due to the structure of the 3D Hamiltonian being a tensor product of the HH model and the AA model with the AA model occupying the z dimension and the time dimension. These figures demonstrate

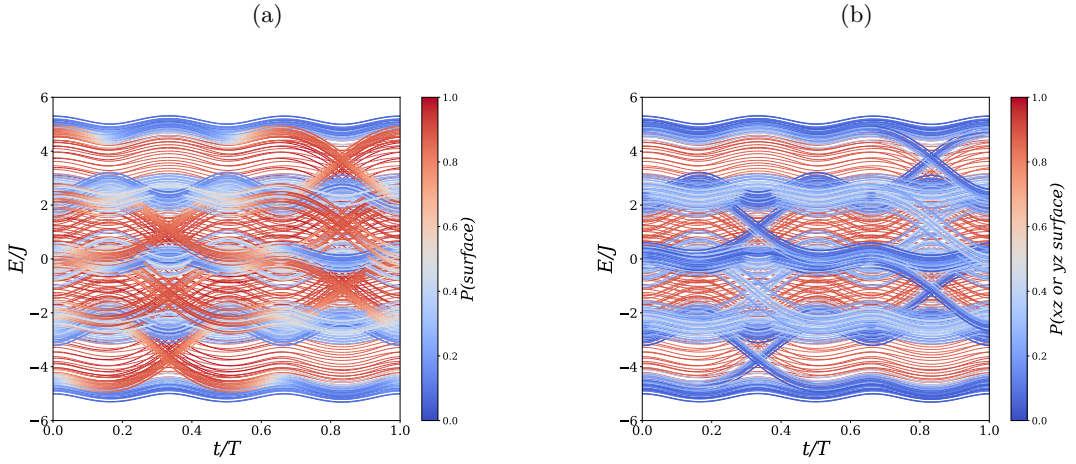

Figure 3.3: The energy spectrum of $\hat{H}_{3D}$ with open boundary conditions. (a) The eigenvalues of $\hat{H}_{3D}$ are coloured to indicate the probability that it is located on the surface of the system. (b) The eigenvalues of $\hat{H}_{3D}$ are coloured to indicate the probability that it is located on a surface of the system in the xz or yz plane

that $\hat{H}_{3D}$ possesses surface modes with complex time dependence.

3.4 Rice-Mele Quasicrystal

In this section we introduce the Rice-Mele quasicrystal. This model allows one to investigate how different aperiodic sequences can give rise to different topological structures. This model was first introduced by Yoshii *et al.* in [51]. Here they applied the Fibonacci sequence to the model and labelled it the Rice-Mele-Fibonacci model. We will be applying different aperiodic sequences in this thesis and therefore we will refer to it as the Rice-Mele quasicrystal model. We also choose not analyse the topological structure of this Hamiltonian or look at the energy spectrum until later when we introduce the aperiodic sequences that will be investigated. This is because both the energy spectrum and the topological structure of the system are highly dependent upon the sequence that is applied.

The Rice-Mele quasicrystal (RMQ) model is very similar to the original Rice-Mele (RM) model and its Hamiltonian is defined as

$$\hat{H}_{RMQ} = \sum_n J\left|n\right\rangle\left\langle n+1\right| + (-1)^{f_n}\delta(t)\left|n\right\rangle\left\langle n+1\right| + h.c. + \sum_n (-1)^{f_n}\gamma(t)\left|n\right\rangle\left\langle n\right|,$$

$$\delta(t) = \delta_0\cos(2\pi t/T) \qquad \gamma(t) = \gamma_0\sin(2\pi t/T). \tag{3.8}$$

Here n labels the lattice sites of the system, J is a fixed hopping value and $\delta(t)$ and $\gamma(t)$ are time-dependent modulating components for the hopping and on-site potential respectively. We choose the

modulating components to have the same period T for our investigation but they do not have to be in general. The key difference between the RM model and the RMQ model lies in the values f_n takes. For the RM model $f_n = n$ which gives the system a periodic nature, however, the RMQ model sets f_n to equal some aperiodic sequence of 0's and 1's with a length equal to that of the system. Later in this thesis we will investigate what happens when f_n is set to the silver mean sequence, the Period-doubling sequence and the Thue-Morse sequence. Due to this model being aperiodic when f_n is set to an aperiodic sequence the Chern number defined in eq. (2.28) is not well defined and we will investigate the topological index of this system using a different method which we will introduce later.

With this we have introduced the topological insulating models that will be considered in this thesis. In the next chapter we will introduce the Chern marker which is a topological marker defined for 2D systems and allows one to determine the topological structure in a local region of the system.

4

Chern marker in 2D and 4D

The Chern marker is a real-space local quantity that can be used to determine the topological index of a system despite this being a global property. This is possible because the topology is a bulk property and therefore for systems with translational invariance a single unit cell contains all the information needed to determine a system's topological index. It is important that this unit cell is located far from the edges of the system so that bulk properties of the system dominate and edge effects can be neglected.

The Chern marker was proposed by Raffaello Bianco and Raffaele Resta for 2D systems in order to develop a way of measuring the topological index of these systems without translational invariance [34]. Due to this property it has been used to analyse topological phases and topological phase transitions of 2D inhomogeneous systems [35, 36, 37, 38, 39, 40, 41, 42, 43]. As well as this, other work has shown that topological currents measured by the Chern marker can arise when the system undergoes a quantum quench [44]. Due to its local nature, one could view the Chern marker as a local topological order parameter similar to traditional local order parameters for other types of phase transitions; however, it is important to stress that the Chern marker does not analyse the breaking of symmetries within the system like an order parameter.

Another useful property of the Chern marker is that it can determine the topological index of a system with open boundary conditions as long as it is calculated within the bulk where the edge state

modes do not contribute. This has recently been show to be very useful as it allows one to predict the topological index of non-Hermitian systems where the boundary conditions are important due to the non-Hermitian skin effect [45].

In this chapter we first introduce the Chern marker for 2D systems and show that it is equal to the Chern number of the system. After this, we then go on to develop a Chern marker for four-dimensional systems and show that it equals the second Chern number of a four-dimensional system.

4.1 Notation

Before we define the Chern marker for 2D systems we first have to introduce some notation that will be used frequently throughout the rest of the thesis. Earlier we introduced Bloch's theorem which allows us to separate out the periodic part of a wave function from the non-periodic part. We restate it here for ease.

$$|\psi_{\boldsymbol{k}n}\rangle = |\boldsymbol{k}\rangle \otimes |u_{\boldsymbol{k}n}\rangle \qquad\qquad |\boldsymbol{k}\rangle = \frac{1}{\sqrt{V_{\mathrm{BZ}}}} \sum_{\boldsymbol{x}} e^{i\boldsymbol{x}\cdot\boldsymbol{k}} |\boldsymbol{x}\rangle \tag{4.1}$$

where $|u_{\boldsymbol{k}n}\rangle$ is the cell-periodic part of Bloch state, n labels the band and $\boldsymbol{k}$ labels the wave vector.

From this we can define the operator $\hat{P}$ which projects into the occupied states for a given Hamiltonian. The projector $\hat{P}$ is defined in the following way

$$\hat{P} = \sum_{n}^{\mathrm{occ}} \int d\boldsymbol{k}\, |\psi_{\boldsymbol{k}n}\rangle \langle\psi_{\boldsymbol{k}n}| = \int d\boldsymbol{k}\, |\boldsymbol{k}\rangle \langle\boldsymbol{k}| \otimes \hat{\mathcal{P}}_{\boldsymbol{k}} \tag{4.2}$$

where the summation over n runs over all occupied states. Here we have taken the continuous limit and therefore we get an integral over $\boldsymbol{k}$. From here onwards all integrals over $\boldsymbol{k}$ are taken over the first Brillouin zone and we sometimes drop the BZ subscript for notational ease. In the second equality we have introduced a new projector $\hat{\mathcal{P}}_{\boldsymbol{k}}$ which we define as

$$\hat{\mathcal{P}}_{\boldsymbol{k}} = \sum_{n}^{\mathrm{occ}} |u_{\boldsymbol{k}n}\rangle \langle u_{\boldsymbol{k}n}| \,. \tag{4.3}$$

The above projector is the translationally invariant part of the projector $\hat{P}$. Note that it is denoted with a scripted letter. Throughout this thesis we will use scripted letters to denote $\boldsymbol{k}$-dependent (translationally invariant) objects and sometimes drop the subscript $\boldsymbol{k}$ for notational convenience. It is important to stress that the projector $\hat{P}$ can also be defined for inhomogeneous systems, but $\hat{\mathcal{P}}_{\boldsymbol{k}}$ requires translational invariance. We also define the complementary operator $\hat{Q} = \mathbb{1} - \hat{P}$, along with $\hat{\mathcal{Q}}_{\boldsymbol{k}} = \mathbb{1} - \hat{\mathcal{P}}_{\boldsymbol{k}}$, which projects in to the unoccupied bands of the system. Because $\hat{P}$ projects into occupied bands and $\hat{Q}$ projects into unoccupied bands the product of the two gives $\hat{P}\hat{Q} = 0$.

Next, we need to define the position operator. Due to the translational invariance of the system there are 2 ways in which we can define the position operator. One way is to define the position operator to label the lattice sites of the system and the other is to define it so that it labels the unit cells of the system. We will use both definitions throughout this thesis but for this section we define it so that it labels the unit cell in the following way

$$\hat{\boldsymbol{x}} = \sum_{\boldsymbol{x}} \boldsymbol{x} \, |\boldsymbol{x}\rangle \, \langle \boldsymbol{x}| \otimes \mathbb{1}. \tag{4.4}$$

Above, $\mathbb{1}$ is the identity matrix with dimension equal to the number of degrees of freedom within the unit cell. Note that the choice of how we define the position operator does not change the results of the Chern marker but just makes our analytical calculations easier.

Lastly, we need to introduce the unit cell trace of an object. Unlike a traditional trace, which traces over the whole system, we want to consider a single unit cell in the system. We do this by defining the unit cell trace in the following way

$$\mathrm{tr}_{\boldsymbol{x}}(\hat{O}) = \sum_{\alpha} \left(\langle \boldsymbol{x}| \otimes \langle \alpha| \right) \hat{O} \left(|\boldsymbol{x}\rangle \otimes |\alpha\rangle \right). \tag{4.5}$$

As stated earlier, $\boldsymbol{x}$ labels the unit cell and α labels the internal states of the unit cell. We have summed over the internal states of the unit cell only meaning that a unit cell trace of an operator analyses that operator within a single unit cell and produces a local object. From this we can then write the full trace of an object as $\mathrm{Tr}\ (\hat{O}) = \sum_{\boldsymbol{x}} \ \mathrm{tr}_{\boldsymbol{x}}\ (\hat{O})$. We are now ready to define the Chern marker for a 2D system.

4.2 2D Chern marker

In this section we will define the 2D marker and show that it is equal to the Chern number of the system. The Chern marker, $\mathcal{M}_2(\boldsymbol{x})$, for a 2D system is defined as [34]

$$\begin{aligned} \mathcal{M}_2(\boldsymbol{x}) &= \frac{2\pi i}{V_{\mathrm{c}}} \, \mathrm{tr}_{\boldsymbol{x}}\Big(\big[\hat{P}\hat{x}\hat{P}, \hat{P}\hat{y}\hat{P} \big] \Big) \\ &= -\frac{4\pi}{V_{\mathrm{c}}} \, \mathrm{Im} \, \mathrm{tr}_{\boldsymbol{x}}(\hat{P}\hat{x}\hat{Q}\hat{y}\hat{P}), \end{aligned} \tag{4.6}$$

where the square brackets denote the commutator and V_c is the volume of the unit cell. In the second line we used $\hat{P} = \mathbb{1} - \hat{Q}$ as well as the fact that position operators commute. To show that the Chern marker is equal to the Chern number of the system we first have to analyse $\hat{P}\hat{x}\hat{Q}$ further.

The following analysis is valid for arbitrary dimensions. We denote the position operators in a

specific direction for a d-dimensional system as $\hat{x}_i$ $(i \in 1, ..., d)$ and use the notation $\partial_i \equiv \partial_{k_i}$ for derivatives with respect to the crystal momentum in a specific direction. To analyse $\hat{P}\,\hat{x}_i\,\hat{Q}$ we use eq. (4.2) to get

$$\hat{P}\hat{x}_i\hat{Q} = \sum_n^{\text{occ}} \sum_m^{\text{unocc}} \int d\boldsymbol{k}\; d\boldsymbol{k}' \, |\psi_{\boldsymbol{k}n}\rangle \langle\psi_{\boldsymbol{k}n}| \, \hat{x}_i \, |\psi_{\boldsymbol{k}'m}\rangle \langle\psi_{\boldsymbol{k}'m}| \,. \tag{4.7}$$

Using Bloch's theorem and the definition of the position operator we find that

$$\hat{P}\hat{x}_i\hat{Q} = \sum_n^{\text{occ}} \sum_m^{\text{unocc}} \int d\boldsymbol{k} \int d\boldsymbol{k}' \;\; |\boldsymbol{k}\rangle \langle\boldsymbol{k}| \, \hat{x}_i \, |\boldsymbol{k}'\rangle \langle\boldsymbol{k}'| \;\otimes\; |u_{\boldsymbol{k}n}\rangle \langle u_{\boldsymbol{k}n}|u_{\boldsymbol{k}'m}\rangle \langle u_{\boldsymbol{k}'m}| \,. \tag{4.8}$$

If we then use the definition of $|\boldsymbol{k}\rangle$ and how the position operator acts on it in the above equation we see that

$$\hat{P}\hat{x}_i\hat{Q} = \sum_n^{\text{occ}} \sum_m^{\text{unocc}} \int \frac{d\boldsymbol{k}}{V_{\text{BZ}}} \int \frac{d\boldsymbol{k}'}{V_{\text{BZ}}} \sum_{\boldsymbol{x},\boldsymbol{x}''} e^{i\boldsymbol{x}\cdot\boldsymbol{k}} e^{-i\boldsymbol{x}''\cdot\boldsymbol{k}'} \sum_{\boldsymbol{x}'} x'_i e^{i\boldsymbol{x}'\cdot(\boldsymbol{k}'-\boldsymbol{k})} \, |\boldsymbol{x}\rangle \langle\boldsymbol{x}''| \otimes |u_{\boldsymbol{k}n}\rangle \langle u_{\boldsymbol{k}n}|u_{\boldsymbol{k}'m}\rangle \langle u_{\boldsymbol{k}'m}| \,. \tag{4.9}$$

We can rewrite the terms in the summation over $\boldsymbol{x}'$ as a partial derivative to get

$$\begin{aligned}\hat{P}\hat{x}_i\hat{Q} = \sum_n^{\text{occ}} \sum_m^{\text{unocc}} \int \frac{d\boldsymbol{k}}{V_{\text{BZ}}} \int \frac{d\boldsymbol{k}'}{V_{\text{BZ}}} \sum_{\boldsymbol{x},\boldsymbol{x}''} e^{i\boldsymbol{x}\cdot\boldsymbol{k}} e^{-i\boldsymbol{x}''\cdot\boldsymbol{k}'} \sum_{\boldsymbol{x}'} -i\partial_{k'_i}(e^{i\boldsymbol{x}'\cdot(\boldsymbol{k}'-\boldsymbol{k})}) \, |\boldsymbol{x}\rangle \langle\boldsymbol{x}''| \\ \otimes |u_{\boldsymbol{k}n}\rangle \langle u_{\boldsymbol{k}n}|u_{\boldsymbol{k}'m}\rangle \langle u_{\boldsymbol{k}'m}| \,.\end{aligned} \tag{4.10}$$

Integrate by parts and use $\frac{1}{V_{\text{BZ}}} \sum_{\boldsymbol{x}'} e^{i\boldsymbol{x}'\cdot(\boldsymbol{k}'-\boldsymbol{k})} = \delta(\boldsymbol{k}'-\boldsymbol{k})$ it can be shown that

$$\hat{P}\hat{x}_i\hat{Q} = \sum_n^{\text{occ}} \sum_m^{\text{unocc}} \int d\boldsymbol{k} \int d\boldsymbol{k}' \, |\boldsymbol{k}\rangle \langle\boldsymbol{k}'| \, \delta(\boldsymbol{k}'-\boldsymbol{k}) \otimes |u_{\boldsymbol{k}n}\rangle \langle u_{\boldsymbol{k}n}| \left(i\partial_{k'_i} |u_{\boldsymbol{k}'m}\rangle\right) \langle u_{\boldsymbol{k}'m}| \,. \tag{4.11}$$

When carrying out the integration by parts we used that a total derivative over a closed manifold vanishes. As well as this, any other terms that arise apart from the one above are zero due to $\langle u_{\boldsymbol{k}n}|u_{\boldsymbol{k}m}\rangle = \delta_{m,n}$. We therefore have that

$$\hat{P}\hat{x}_i\hat{Q} = \sum_n^{\text{occ}} \sum_m^{\text{unocc}} \int d\boldsymbol{k} \Big(|\boldsymbol{k}\rangle \langle\boldsymbol{k}| \otimes i \, |u_{\boldsymbol{k}n}\rangle \langle u_{\boldsymbol{k}n}|\partial_i \, u_{\boldsymbol{k}m}\rangle \langle u_{\boldsymbol{k}m}| \Big). \tag{4.12}$$

If we now use the definition of $\hat{\mathcal{P}}_{\boldsymbol{k}}$ given in eq. (4.3) along with the definition of $\hat{\mathcal{Q}}_{\boldsymbol{k}}$ we get that $\hat{P}\hat{x}_i\hat{Q}$ is given by

$$\hat{P}\hat{x}_i\hat{Q} = \int d\boldsymbol{k} \;\; |\boldsymbol{k}\rangle \langle\boldsymbol{k}| \;\otimes\; i\hat{\mathcal{P}}_{\boldsymbol{k}}(\partial_i \hat{\mathcal{Q}}_{\boldsymbol{k}}). \tag{4.13}$$

Above, we again used the fact that $\langle u_{\boldsymbol{k}n}|u_{\boldsymbol{k}m}\rangle = \delta_{m,n}$. From the definition of $\hat{\mathcal{Q}}_{\boldsymbol{k}}$ it can be seen that

$\partial_i \hat{\mathcal{Q}} = -\partial_i \hat{\mathcal{P}}$. Using this we get the final form of $\hat{P}\hat{x}_i\hat{Q}$ as

$$\hat{P}\hat{x}_i\hat{Q} = \int d\boldsymbol{k}\, |\boldsymbol{k}\rangle \langle \boldsymbol{k}| \otimes (-i)\hat{\mathcal{P}}(\partial_i \hat{\mathcal{P}}). \tag{4.14}$$

The above identity is very useful identity that will be used numerous times throughout this thesis.

Using eq. (4.14) we can now show that the Chern marker for a 2D system is equal to the Chern number of the system. Substituting eq. (4.14) into the definition of the Chern marker given in eq. (4.6) we get that

$$\begin{aligned} \mathcal{M}_2(\boldsymbol{x}) &= -\frac{4\pi}{V_c}\,\mathrm{Im}\int d\boldsymbol{k}\ \langle \boldsymbol{x}|\boldsymbol{k}\rangle \langle \boldsymbol{k}|\boldsymbol{x}\rangle \sum_\alpha \langle \alpha|\, \hat{\mathcal{P}}(\partial_{\boldsymbol{k}_x}\hat{\mathcal{P}})(\partial_{\boldsymbol{k}_y}\hat{\mathcal{P}})\hat{\mathcal{P}}\, |\alpha\rangle \\ &= \frac{2\pi i}{V_c}\int d\boldsymbol{k}\ \langle \boldsymbol{x}|\boldsymbol{k}\rangle \langle \boldsymbol{k}|\boldsymbol{x}\rangle \sum_\alpha \langle \alpha|\, \hat{\mathcal{P}}\big[(\partial_{k_x}\hat{\mathcal{P}}), (\partial_{k_y}\hat{\mathcal{P}})\big]\hat{\mathcal{P}}\, |\alpha\rangle\,. \end{aligned} \tag{4.15}$$

If we then use the fact that $\langle \boldsymbol{x}|\boldsymbol{k}\rangle = \frac{1}{\sqrt{V_{\mathrm{BZ}}}} e^{i\boldsymbol{k}\cdot\boldsymbol{x}}$ along with $V_{\mathrm{BZ}} = \frac{(2\pi)^2}{V_c}$ for a 2D system we get that

$$\mathcal{M}_2(\boldsymbol{x}) = \frac{i}{2\pi}\int d\boldsymbol{k}\ \mathrm{Tr}_\alpha\Big(\hat{\mathcal{P}}\big[(\partial_{k_x}\hat{\mathcal{P}}), (\partial_{k_y}\hat{\mathcal{P}})\big]\hat{\mathcal{P}}\Big). \tag{4.16}$$

Above we have defined the trace over internal degrees of freedom as $\mathrm{Tr}_\alpha(\hat{O}) = \sum_\alpha \langle \alpha|\, \hat{O}\, |\alpha\rangle$. When the objects inside this trace are all translationally invariant operators, which is true above, this trace obeys all the rules of a normal trace. Finally, using the definition of $\hat{\mathcal{P}}$, as well as the cyclic properties of the trace, it can be shown that that the Chern marker defined in 2D takes the form

$$\mathcal{M}_2(\boldsymbol{x}) = \frac{i}{2\pi}\sum_n^{\mathrm{occ}}\int d\boldsymbol{k}\ \epsilon^{ij}\, \langle \partial_i u_{\boldsymbol{k}n}|\partial_j u_{\boldsymbol{k}n}\rangle\,. \tag{4.17}$$

where ϵ^{ij} is the 2D Levi-Civita symbol. Comparing this to eq. (2.28) we notice that the above equation is the summation of the Chern numbers for each band and as such $M_2(\boldsymbol{x})$ is equal to the Chern number of the system.

Above we have shown that the Chern marker is equal to the Chern number of a 2D system. Although, we defined the position operator to label the unit cell it can be shown that the Chern marker is still equal to the Chern number if the position operator is defined to label the lattice sites of the system [34].

To demonstrate the Chern marker numerically we use it to determine the topological indices of the Hofstadter butterfly. The Hofstadter butterfly depicts the energy spectrum of the Harper-Hofstadter model, defined in eq. (3.3), for different values of b' [63]. We have reproduced this energy spectrum in fig. 4.1 for $\Delta'/J' = -1$. It has been shown that within the gaps of the Hofstadter butterfly the Chern number of the system takes on different non-zero values [64]. As such, we use the Chern marker to depict the different topological regimes within the Hofstadter Butterfly.

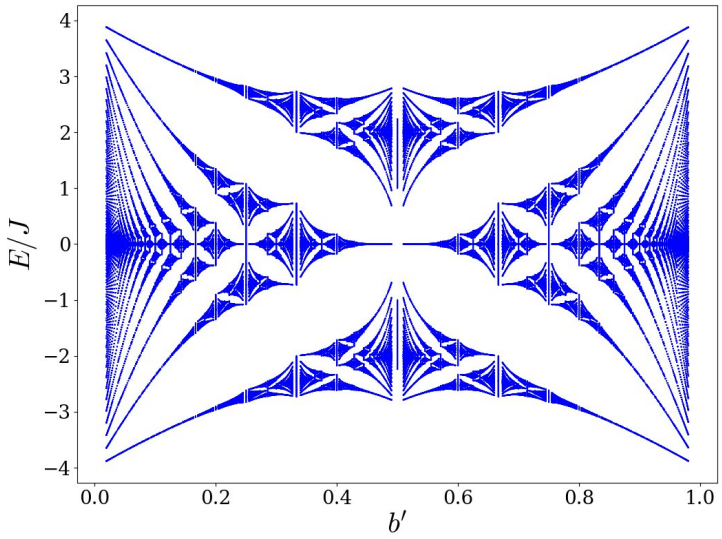

Figure 4.1: The energy spectrum of Harper-Hofstadter model for varying values of b'. The parameters have been set to $\Delta'/J' = -1$. This image is famously known as the Hofstadter butterfly.

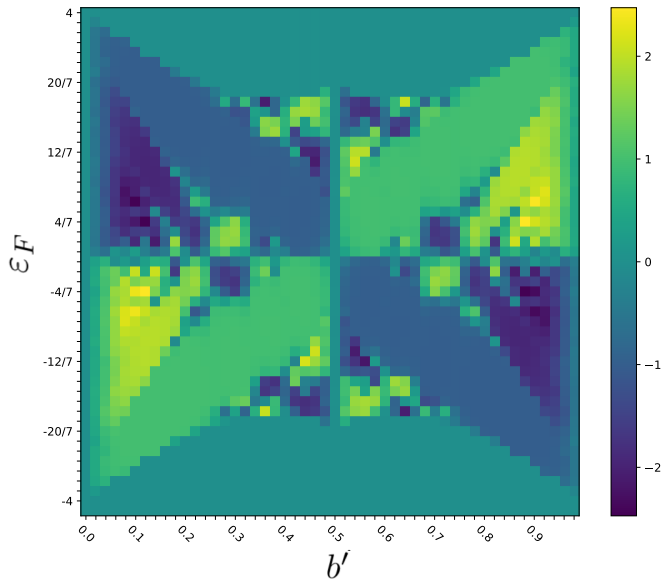

Figure 4.2: The Chern marker for the Harper-Hofstadter model with varying Fermi-energies and values of b'. The parameters of the system were set to $\Delta'/J' = -1$ and the Fermi-energy is given in units of J'.

To achieve this we consider a range of b' values and Fermi-energies, ε_F/J', and calculate the Chern marker of the system for each; the results are shown in fig. 4.2. This figure clearly captures the general shape of the Hofstadter butterfly and shows that for the largest gaps in the Hofstadter butterfly the Chern number of the system has a magnitude of 1 and for the next largest gap the Chern number has a magnitude of 2. The image in fig. 4.2 agrees with the previous findings shown in [64] where the Chern numbers of the system were found using the Diophantine equation which we will introduce later.

As such, we have demonstrated numerically that the Chern marker is an effective way of determining the Chern number of a system. The advantages of the Chern marker are that it is a local measurement and does not require translational invariance. Together these properties make the Chern marker a very useful tool to probe the topological properties of a system.

4.3 Chern marker in 4D

In the previous section we introduced the 2D Chern marker and showed that it is equal to the Chern number. Topological systems in 2D have been studied extensively, but there has also been considerable progress in theoretically understanding phenomena in 4D topological quantum systems such as the quantum Hall effect [27, 28, 29]. For 4D systems the topological index of the system is given by the second Chern marker which we define later in this section [24]. Recent advancements in topological photonics and cold atomic systems have allowed some of these 4D topological effects to be observed experimentally with 2 of the dimensions being 'synthetic dimensions' [30, 31]. Such 4D topological systems can also be related to 3D time-dependent systems by the process of dimensional reduction [24]; however, the properties of the system that emerge due to the topological structure can manifest differently.

With this increased interest in 4D topological systems it is natural to ask whether a similar type of real-space local topological marker exists for 4D systems. In this section we will define the Chern marker for a 4D system and show that it is equal to the second Chern number of the system which describes the topological nature of a 4D system.

Before defining the Chern marker for a 4D system it is useful to rewrite the Chern marker for a 2D system in a slightly different form; this will make the generalisation to four dimensions easier to see. The Chern marker for a 2D system can be written as

$$\mathcal{M}_2(\boldsymbol{x}) = \frac{2\pi i}{V_c}\epsilon^{ij}\sum_{\alpha}\langle \boldsymbol{x},\alpha|\,\hat{P}\hat{x}_i\hat{Q}\hat{x}_j\hat{P}\,|\boldsymbol{x},\alpha\rangle \tag{4.18}$$

where $|\boldsymbol{x},\alpha\rangle = |\boldsymbol{x}\rangle\otimes|\alpha\rangle$ and $\hat{x}_1 = \hat{x}$ and $\hat{x}_2 = \hat{y}$. Here we have used $\hat{P} = \mathbb{1} - \hat{Q}$ along with the fact that the position operators commute with each other. Using the above equation as a template, we

now define the Chern marker in 4D as

$$\mathcal{M}_4(\boldsymbol{x}) = \frac{2\pi^2}{V_c}\epsilon^{ijkl}\sum_{\alpha}\langle \boldsymbol{x},\alpha|\,\hat{P}\hat{x}_i\hat{Q}\hat{x}_j\hat{P}\hat{x}_k\hat{Q}\hat{x}_l\hat{P}\,|\boldsymbol{x},\alpha\rangle\,, \tag{4.19}$$

where ϵ^{ijkl} is the 4D Levi-Civita symbol and $\{\hat{x}_1,\hat{x}_2,\hat{x}_3,\hat{x}_4\} = \{\hat{x},\hat{y},\hat{z},\hat{w}\}$ (with w labelling the fourth spatial dimension). If we now use the identities $\hat{P}\hat{P} = \hat{P}$ and $\hat{Q}\hat{Q} = \hat{Q}$ and substitute the form of $\hat{P}\hat{x}\hat{Q}$ given in eq. (4.14), along with its Hermitian conjugate, into eq. (4.19) we get that

$$\mathcal{M}_4(\boldsymbol{x}) = \frac{2\pi^2}{V_c}\,\epsilon^{ijkl}\int d\boldsymbol{k}\,\langle\boldsymbol{x}|\boldsymbol{k}\rangle\,\langle\boldsymbol{k}|\boldsymbol{x}\rangle\sum_{\alpha}\langle\alpha|\,\hat{\mathcal{P}}(\partial_i\hat{\mathcal{P}})(\partial_j\hat{\mathcal{P}})\hat{\mathcal{P}}(\partial_k\hat{\mathcal{P}})(\partial_l\hat{\mathcal{P}})\hat{\mathcal{P}}\,|\alpha\rangle\,. \tag{4.20}$$

Using $|\langle\boldsymbol{x}|\boldsymbol{k}\rangle|^2 = \frac{1}{V_{BZ}}$ and $V_{BZ} = \frac{(2\pi)^d}{V_c}$ we see that

$$\begin{aligned}\mathcal{M}_4(\boldsymbol{x}) =& \frac{\epsilon^{ijkl}}{8\pi^2}\int d\boldsymbol{k}\,\mathrm{Tr}_\alpha\Big(\hat{\mathcal{P}}(\partial_i\hat{\mathcal{P}})(\partial_j\hat{\mathcal{P}})\hat{\mathcal{P}}(\partial_k\hat{\mathcal{P}})(\partial_l\hat{\mathcal{P}})\Big)\\ =& \frac{\epsilon^{ijkl}}{32\pi^2}\int d\boldsymbol{k}\,\mathrm{Tr}\big(B_{ij}\;B_{kl}\big).\end{aligned} \tag{4.21}$$

Here $B_{jk} = \partial_j\tilde{\mathcal{A}}_k - \partial_k\tilde{\mathcal{A}}_j - i[\tilde{\mathcal{A}}_j,\tilde{\mathcal{A}}_k]$ is the matrix Berry curvature for a 4D system, $\tilde{\mathcal{A}}_j^{nm} = i\,\langle u_{\boldsymbol{k}n}|\partial_j\,u_{\boldsymbol{k}m}\rangle$ is the matrix Berry connection, with n and m labelling the occupied bands, and the trace in the second equality is a trace over the occupied bands. Note earlier we defined the Berry curvature B with out the commutator; this is because it disappears in the 2D case due to the trace of a commutator being zero but does not disappear for the 4D case. The last equality is the definition of the second Chern number [24]. We have thus shown that the Chern marker for a 4D system is equal to the second Chern number of the system. It is also worth pointing out that the Chern marker in 4D can correctly predict the topology of a system even if the occupied bands overlap. This is due to the fact that it is defined using the projectors of the system.

It was stated earlier that the Chern marker in 2D has been used to investigate the topology of 2D non-Hermitian Hamiltonians. It would therefore be interesting to see if the Chern marker in 4D could be used to investigate the topology of 4D non-Hermitian Hamiltonians, however, this will not be investigated in this thesis.

5

Bott index

At this point we have defined the Chern number of a system using the TKNN form. This, however, is not the only way in which the topological index of a system can be calculated. Another way is by calculating the Bott index. In this chapter we will introduce the Bott index and show analytically that it is equivalent to the Chern number of the system, both for the discrete case and the continuous case. We will also show that one can define a local version of the Bott index and analyse how this object is related to the Chern marker. Lastly, we will discuss the pros and cons of both the local Bott index and the Chern marker.

5.1 Bott Index and Chern Number

When investigating the bulk properties of systems with translational invariance one generally takes periodic boundary conditions. As a result the position operator becomes multivalued. To see this consider a 2D system with length L_x and L_y in the x and y directions respectively and periodic boundary conditions in each direction. This system is invariant under the transformations $\hat{x} \to \hat{x} + L_x$ and $\hat{y} \to \hat{y} + L_y$. This means that any point with the position $\boldsymbol{x}$ can also be labelled by $\boldsymbol{x} + n\,L_x\hat{\boldsymbol{i}} + m\,L_y\hat{\boldsymbol{j}}$, where $n, m \in \mathbb{Z}$. Here $\hat{\boldsymbol{i}}$ and $\hat{\boldsymbol{j}}$ are unit vectors in the x and y directions respectively. This is clearly not desirable. When we act on the wave function, $\psi(\boldsymbol{x})$, with a position operator we therefore

only wish to know the spatial position modulo $\boldsymbol{L}$, where $\boldsymbol{L} = \{L_x, L_y\}$. Our current definition of the position operator does not do this, but we can construct something that does. We define the position operators for a 2D periodic system as

$$\hat{\boldsymbol{x}}_p = -i\frac{\boldsymbol{L}}{2\pi}\ln\left(e^{i\hat{\boldsymbol{x}}\,2\pi/\boldsymbol{L}}\right) \tag{5.1}$$

where $\hat{\boldsymbol{x}}$ is given by eq. (4.4) and ln is the natural logarithm. From this the components of $\hat{\boldsymbol{x}}_p$ are given by

$$\hat{x}_p = -i\frac{L_x}{2\pi}\ln\left(e^{i\hat{x}\,2\pi/L_x}\right) \qquad , \qquad \hat{y}_p = -i\frac{L_y}{2\pi}\ln\left(e^{i\hat{y}\,2\pi/L_y}\right). \tag{5.2}$$

We are now in a position to define the Bott index and start to analyse its relationship with the Chern number. Let us first discuss why the Bott index is useful and what it exactly measures. The Bott index was initially derived in a mathematical sense to determine if a pair of matrices that do not commute exactly are either close to commuting or far from commuting. It was later adapted to the aspect of topological insulators by Loring and Hastings where they used the Bott index to measure if the state was in a topological regime or a trivial one [65, 66, 67]. For a mathematical perspective of the Bott index and references to the original work see [68]. The Bott index can be used to distinguish trivial states from topological states because, as we showed with the Chern marker, the projected position operators, $\hat{P}\hat{x}_i\hat{P}$, of a topological system do not commute, but those of a trivial system do commute. Another benefit of using the Bott index is it can be used on systems that contain disorder which breaks translational invariance within the system [65], just like the Chern marker, where as the Chern number cannot. With this we will now introduce the Bott index and show it is equal to the Chern number in the periodic case.

The Bott index is defined for a 2D system in the following way

$$\mathcal{B} = -\frac{1}{2\pi}\mathrm{Im}\mathrm{Tr}\ln(UVU^\dagger V^\dagger), \tag{5.3}$$

where U and V are defined as

$$U = \hat{P}e^{i\hat{x}\,2\pi/L_x}\hat{P} + \hat{Q}, \tag{5.4}$$

$$V = \hat{P}e^{i\hat{y}\,2\pi/L_y}\hat{P} + \hat{Q}. \tag{5.5}$$

Because the system we are considering is translationally invariant we can decompose the projectors

using eq. (4.2). Doing this we find that the Bott index takes the form

$$\mathcal{B} = -\frac{1}{2\pi}\mathrm{Im\ Tr\ ln}\Big(\sum_{\boldsymbol{k}_1\boldsymbol{k}_2\boldsymbol{k}_3\boldsymbol{k}_4\boldsymbol{k}_5} |\boldsymbol{k}_1\rangle\langle\boldsymbol{k}_1| e^{i\hat{x}2\pi/L_x} |\boldsymbol{k}_2\rangle\langle\boldsymbol{k}_2| e^{i\hat{y}2\pi/L_y} |\boldsymbol{k}_3\rangle\langle\boldsymbol{k}_3| e^{-i\hat{x}2\pi/L_x} |\boldsymbol{k}_4\rangle \\ \langle\boldsymbol{k}_4| e^{-i\hat{y}2\pi/L_y} |\boldsymbol{k}_5\rangle\langle\boldsymbol{k}_5| \otimes \hat{\mathcal{P}}_{\boldsymbol{k}_1}\hat{\mathcal{P}}_{\boldsymbol{k}_2}\hat{\mathcal{P}}_{\boldsymbol{k}_3}\hat{\mathcal{P}}_{\boldsymbol{k}_4}\hat{\mathcal{P}}_{\boldsymbol{k}_5} + \hat{Q}\Big). \tag{5.6}$$

Here we have defined the Bott index for a discrete system and will take the continuum limit later; we have also chosen the position operators to label the unit cells rather than the lattice sites. In the above equation we have not decoupled the internal and external degrees of freedom of $\hat{Q}$ to keep the equation condensed. We can analyse how the exponential acts on $|\boldsymbol{k}\rangle$ by using eq. (2.5) which we restate here for ease;

$$|\boldsymbol{k}\rangle = \frac{1}{\sqrt{N}}\sum_{\boldsymbol{x}} e^{i\boldsymbol{x}\cdot\boldsymbol{k}} |\boldsymbol{x}\rangle\,. \tag{5.7}$$

Above we have defined $|\boldsymbol{k}\rangle$ for the discrete case with N being the number of unit cells in the system. Doing this we get that

$$\begin{aligned} e^{i\hat{x}\ 2\pi/L_x}\ |\boldsymbol{k}\rangle &= \frac{1}{\sqrt{N}}\sum_{\boldsymbol{x}} e^{\{i\,x\,(2\pi/L_x+k_x)+i\,y\,k_y\}} |\boldsymbol{x}\rangle \\ &= \left|\boldsymbol{k} + 2\pi/L_x\hat{\boldsymbol{i}}\right\rangle. \end{aligned} \tag{5.8}$$

Using this in eq. (5.6) the Bott index becomes

$$\mathcal{B} = -\frac{1}{2\pi}\mathrm{Im\ Tr\ ln}\Big(\sum_{\boldsymbol{k}}\ \Big[|\boldsymbol{k}\rangle\langle\boldsymbol{k}| \otimes \hat{\mathcal{P}}_{\boldsymbol{k}}\hat{\mathcal{P}}_{\boldsymbol{k}-\frac{2\pi}{L_x}\hat{\boldsymbol{i}}}\hat{\mathcal{P}}_{\boldsymbol{k}-\frac{2\pi}{L_x}\hat{\boldsymbol{i}}-\frac{2\pi}{L_y}\hat{\boldsymbol{j}}}\hat{\mathcal{P}}_{\boldsymbol{k}-\frac{2\pi}{L_y}\hat{\boldsymbol{j}}}\hat{\mathcal{P}}_{\boldsymbol{k}}\Big] + \hat{Q}\Big). \tag{5.9}$$

From this equation we can explore the relation between the Bott index and the Chern number for both the continuous regime and the discrete regime.

We will first analyse the continuous regime where we have $L_x \to \infty$ and $L_y \to \infty$. Due to this we can Taylor expand $\hat{\mathcal{P}}_{\boldsymbol{k}-\frac{2\pi}{L_x}\hat{\boldsymbol{i}}}$ in terms of $\hat{\mathcal{P}}_{\boldsymbol{k}}$. The expansions are given below

$$\hat{\mathcal{P}}_{\boldsymbol{k}-\frac{2\pi}{L_x}\hat{\boldsymbol{i}}} = \hat{\mathcal{P}}_{\boldsymbol{k}} - \partial_{k_x}\hat{\mathcal{P}}_{\boldsymbol{k}}\,\delta_x + \frac{1}{2}\partial_{k_x}\partial_{k_x}\hat{\mathcal{P}}_{\boldsymbol{k}}\,\delta_x^2 + ... \tag{5.10}$$

$$\hat{\mathcal{P}}_{\boldsymbol{k}-\frac{2\pi}{L_x}\hat{\boldsymbol{i}}-\frac{2\pi}{L_y}\hat{\mathbf{j}}} = \hat{\mathcal{P}}_{\boldsymbol{k}} - \partial_{k_x}\hat{\mathcal{P}}_{\boldsymbol{k}}\,\delta_x - \partial_{k_y}\hat{\mathcal{P}}_{\boldsymbol{k}}\,\delta_y + \frac{1}{2}\partial_{k_x}\partial_{k_x}\hat{\mathcal{P}}_{\boldsymbol{k}}\,\delta_x^2 + \frac{1}{2}\partial_{k_y}\partial_{k_y}\hat{\mathcal{P}}_{\boldsymbol{k}}\,\delta_y^2 + \partial_{k_x}\partial_{k_y}\hat{\mathcal{P}}_{\boldsymbol{k}}\,\delta_x\delta_y + ... \tag{5.11}$$

where $\delta_x = 2\pi/L_x$ and $\delta_y = 2\pi/L_y$. From here on we will also assume that $L_x = L_y$, which is possible because we are going to take the limit $L_x, L_y \to \infty$, and consider terms up to order $\mathcal{O}(\delta^2)$ where $\delta = min\{\delta_x, \delta_y\}$. Using these expansions and the projector identities $P(\partial_i P)P = 0$ and $P(\partial_i\partial_j P)P = -P(\partial_i P)(\partial_j P)P - P(\partial_j P)(\partial_i P)P$, and carrying out a lot of simple algebra, it can be shown that the

Bott index is given by

$$\mathcal{B} = -\frac{1}{2\pi}\mathrm{Im}\,\mathrm{Tr}\ln\Bigg(\int_{\mathrm{BZ}} d\boldsymbol{k}\ \ket{\boldsymbol{k}}\bra{\boldsymbol{k}}\otimes\Big(\hat{\mathcal{P}}_{\boldsymbol{k}}+\hat{Q}_{\boldsymbol{k}}+\hat{\mathcal{P}}_{\boldsymbol{k}}\big[\partial_{k_x}\hat{\mathcal{P}}_{\boldsymbol{k}},\partial_{k_y}\hat{\mathcal{P}}_{\boldsymbol{k}}\big]\hat{\mathcal{P}}_{\boldsymbol{k}} + \frac{1}{2}\hat{\mathcal{P}}_{\boldsymbol{k}}(\partial_{k_x}\partial_{k_x}\hat{\mathcal{P}}_{\boldsymbol{k}})\hat{\mathcal{P}}_{\boldsymbol{k}}+\frac{1}{2}\hat{\mathcal{P}}_{\boldsymbol{k}}(\partial_{k_y}\partial_{k_y}\hat{\mathcal{P}}_{\boldsymbol{k}})\hat{\mathcal{P}}_{\boldsymbol{k}}\Big)\Bigg). \tag{5.12}$$

Above we have taken the limit $L_x, L_y \to \infty$ and therefore the summation and the delta objects become an integral. The next key thing to realise is that the projector is Hermitian and self-adjoint and therefore the second derivative is also Hermitian and self-adjoint meaning that the imaginary parts of the last two terms in equation (5.12) are zero. We have thus shown that the Bott index is given by

$$\mathcal{B} = -\frac{1}{2\pi}\mathrm{Im}\,\mathrm{Tr}\ln\Big(\mathbb{1}+\int_{\mathrm{BZ}} d\boldsymbol{k}\,\ket{\boldsymbol{k}}\bra{\boldsymbol{k}}\otimes\hat{\mathcal{P}}\big[\partial_{k_x}\hat{\mathcal{P}},\partial_{k_y}\hat{\mathcal{P}}\big]\hat{\mathcal{P}}\Big). \tag{5.13}$$

where above we have dropped the subscript $\boldsymbol{k}$ for ease of notation. The next step is to look at the expansion of the logarithm. The expansion gives

$$\ln(1+A) = A - \frac{1}{2}A^2 + ... \tag{5.14}$$

Thus, when working to order $\mathcal{O}(\delta^2)$, the Bott index is given by

$$\mathcal{B} = -\frac{1}{2\pi}\mathrm{Im}\,\mathrm{Tr}\Big(\int_{\mathrm{BZ}} d\boldsymbol{k}\ \ket{\boldsymbol{k}}\bra{\boldsymbol{k}}\otimes\hat{\mathcal{P}}\big[\partial_{k_x}\hat{\mathcal{P}},\partial_{k_y}\hat{\mathcal{P}}\big]\hat{\mathcal{P}}\Big). \tag{5.15}$$

Using the definition of $\hat{\mathcal{P}}$ one can show that

$$\int_{\mathrm{BZ}} d\boldsymbol{k}\,\ket{\boldsymbol{k}}\bra{\boldsymbol{k}}\otimes\hat{\mathcal{P}}\big[\partial_{k_x}\hat{\mathcal{P}},\partial_{k_y}\hat{\mathcal{P}}\big]\hat{\mathcal{P}} = \sum_n^{\mathrm{occ}}\int_{\mathrm{BZ}} d\boldsymbol{k}\,\ket{\psi_{\boldsymbol{k}n}}\bra{\psi_{\boldsymbol{k}n}}\left(\braket{\partial_{k_x}u_{\boldsymbol{k}n}}{\partial_{k_y}u_{\boldsymbol{k}n}} - \braket{\partial_{k_y}u_{\boldsymbol{k}n}}{\partial_{k_x}u_{\boldsymbol{k}n}}\right) \tag{5.16}$$

Using this and the cyclic properties of the trace we get that

$$\mathcal{B} = -\frac{1}{2\pi}\mathrm{Im}\sum_n^{\mathrm{occ}}\int_{\mathrm{BZ}} d\boldsymbol{k}\left(\braket{\partial_{k_x}u_{\boldsymbol{k}n}}{\partial_{k_y}u_{\boldsymbol{k}n}} - \braket{\partial_{k_y}u_{\boldsymbol{k}n}}{\partial_{k_x}u_{\boldsymbol{k}n}}\right) \tag{5.17}$$

Using the definition of the Berry curvature given in eq. (2.29) we see that the Bott index is in fact the Chern number,

$$\mathcal{B} = \frac{1}{2\pi}\sum_n^{\mathrm{occ}}\int_{\mathrm{BZ}} d\boldsymbol{k}\,\boldsymbol{B}^n_{xy} = C_1 \tag{5.18}$$

A more in depth comparison has also been carried out in [69]. It should be noted that above we defined the Bott index with a minus sign out front. This ensures that the Bott index is equivalent to the Chern

number as we previously defined it. If the Chern number is defined with a minus sign out front, which some times it is, then the minus sign in the definition of the Bott index should be removed to ensure that the Bott index and the Chern number are equivalent.

We will now show that a similar relationship exists for the discrete case. Starting from equation (5.9) we need to analyse the chain of $\hat{\mathcal{P}}$ projectors in terms of the periodic states, $|u_{\boldsymbol{k}n}\rangle$. Doing this one gets

$$\begin{aligned}&\hat{\mathcal{P}}\,\hat{\mathcal{P}}_{\boldsymbol{k}+\delta_x\hat{\boldsymbol{i}}}\,\hat{\mathcal{P}}_{\boldsymbol{k}+\delta_x\hat{\boldsymbol{i}}+\delta_y\hat{\boldsymbol{j}}}\,\hat{\mathcal{P}}_{\boldsymbol{k}+\delta_y\hat{\boldsymbol{j}}}\,\hat{\mathcal{P}}\\ &\qquad=\\ &\sum_n |u_{\boldsymbol{k},n}\rangle\left\langle u_{\boldsymbol{k},n}\middle|u_{\boldsymbol{k}+\delta_x\hat{\boldsymbol{i}},n}\right\rangle\left\langle u_{\boldsymbol{k}+\delta_x\hat{\boldsymbol{i}},n}\middle|u_{\boldsymbol{k}+\delta_x\hat{\boldsymbol{i}}+\delta_y\hat{\boldsymbol{j}},n}\right\rangle\left\langle u_{\boldsymbol{k}+\delta_x\hat{\boldsymbol{i}}+\delta_y\hat{\boldsymbol{j}},n}\middle|u_{\boldsymbol{k}+\delta_y\hat{\boldsymbol{j}},n}\right\rangle\left\langle u_{\boldsymbol{k}+\delta_y\hat{\boldsymbol{j}},n}\middle|u_{\boldsymbol{k},n}\right\rangle\langle u_{\boldsymbol{k},n}|\,.\end{aligned} \tag{5.19}$$

The right hand side of the above equation contains a loop around a plaquette in $\boldsymbol{k}$-space and therefore measures the phase around this loop. This is very similar to the discrete version of the Berry flux given in eq. (2.14). As such, we define F_{k_x,k_y} as

$$F_{k_x,k_y} = -\arg\left\langle u_{\boldsymbol{k}}\middle|u_{\boldsymbol{k}+\delta_x\hat{\boldsymbol{i}}}\right\rangle\left\langle u_{\boldsymbol{k}+\delta_x\hat{\boldsymbol{i}}}\middle|u_{\boldsymbol{k}+\delta_x\hat{\boldsymbol{i}}+\delta_y\hat{\boldsymbol{j}}}\right\rangle\left\langle u_{\boldsymbol{k}+\delta_x\hat{\boldsymbol{i}}+\delta_y\hat{\boldsymbol{j}}}\middle|u_{\boldsymbol{k}+\delta_y\hat{\boldsymbol{j}}}\right\rangle\left\langle u_{\boldsymbol{k}+\delta_y\hat{\boldsymbol{j}}}\middle|u_{\boldsymbol{k}}\right\rangle. \tag{5.20}$$

Using this we then get that

$$\hat{\mathcal{P}}\hat{\mathcal{P}}_{\boldsymbol{k}-\delta_x\hat{\boldsymbol{i}}}\hat{\mathcal{P}}_{\boldsymbol{k}-\delta_x\hat{\boldsymbol{i}}-\delta_y\hat{\boldsymbol{j}}}\hat{\mathcal{P}}_{\boldsymbol{k}-\delta_y\hat{\boldsymbol{j}}}\hat{\mathcal{P}} = \hat{\mathcal{P}}e^{-iF_{k_x,k_y}}. \tag{5.21}$$

The summation of all the plaquettes in the system should give us the loop around the whole system which is the Berry phase as discussed earlier. Substituting equation (5.21) into equation (5.9) we now have that the Bott index is given by

$$\mathcal{B} = -\frac{1}{2\pi}\mathrm{Im}\,\mathrm{Tr}\ln\Big(\hat{P}\sum_{\boldsymbol{k}} e^{-iF_{k_x,k_y}} + \hat{Q}\Big). \tag{5.22}$$

From here we need to use the identity $\ln(a\hat{P}+\hat{Q}) = \ln(a)\hat{P}$. The proof of this identity is given below.

$$\begin{aligned}&e^{\ln(a)\hat{P}} = \sum_{n=0}^{\infty}\frac{\ln(a)^n}{n!}\hat{P}^n = \mathbb{1} + \hat{P}\sum_{n=1}^{\infty}\frac{\ln(a)^n}{n!} = \mathbb{1} + \hat{P}(e^{\ln(a)}-1) = \mathbb{1} - \hat{P} + \hat{P}a = \hat{Q} + \hat{P}a\\ &\Rightarrow \ln(a)\hat{P} = \ln(\hat{Q}+\hat{P}a).\end{aligned} \tag{5.23}$$

Using this identity the Bott index now becomes

$$\mathcal{B} = -\frac{1}{2\pi}\mathrm{Im}\mathrm{Tr}\Big(\ln\Big(\sum_{\boldsymbol{k}} e^{-iF_{k_x,k_y}}\Big)\hat{P}\Big). \tag{5.24}$$

This then reduces to the form of the discrete Chern number defined in eq. (2.17),

$$\mathcal{B} = \frac{1}{2\pi} \sum_{k_x,k_y} F_{k_x,k_y} = C_1 \tag{5.25}$$

With this we now confirm that F_{k_x,k_y} is the Berry flux through a plaquette of the discrete system. It is important to stress that no approximation has been made here and the Bott index reduces exactly to the discrete Chern number.

We have thus shown that the Bott index and the Chern number are equivalent in both the continuous and discrete regimes for a system. Just like the Chern marker, the Bott index is well defined for systems without translational invariance where the Chern number is not well defined. In the next section we will introduce a local version of the Bott Index and show that it is equivalent to the Chern marker.

5.2 Local Bott index and Chern marker

In the previous section we introduced the Bott index, showing that it is equal to the Chern number of the system. From the definition of the Bott index, given in eq. (5.3), we can define a local Bott index as

$$\mathcal{B}(\boldsymbol{x}) = -\frac{L_x L_y}{2\pi} \operatorname{Im} \operatorname{tr}_{\boldsymbol{x}} \Big(\ln(UVU^\dagger V^\dagger) \Big) \qquad\qquad \mathcal{B} = \frac{1}{L_x L_y} \sum_{\boldsymbol{x}} \mathcal{B}(\boldsymbol{x}) \tag{5.26}$$

where L_x and L_y are the lengths of the system in the x and y directions respectively. The local Bott index then analyses the topological index of a single unit cell rather than the whole system. With this we will now investigate the relation between the Chern marker and the local Bott index. It is easy to show that $UVU^\dagger V^\dagger$ is invariant under the transformations;

$$U = \hat{P} e^{i\hat{x}\delta_x} \hat{P} + \hat{Q} \;\rightarrow\; U' = \hat{P} e^{i(\hat{x}-C_x)\delta_x} \hat{P} + \hat{Q}, \tag{5.27}$$

$$V = \hat{P} e^{i\hat{y}\delta_y} \hat{P} + \hat{Q} \;\rightarrow\; V' = \hat{P} e^{i(\hat{y}-C_y)\delta_y} \hat{P} + \hat{Q} \tag{5.28}$$

where δ_x and δ_y were previously defined and C_x and C_y are real constants. If we then chose C_x and C_y such that $(\hat{x} - C_x)\delta_x << 1$ and $(\hat{y} - C_y)\delta_y << 1$ we change the exponential to be an exponential of a small quantity allowing us to expand to leading order. Carrying out this expansion it can be shown that

$$U'V'U^{\dagger'}V^{\dagger'} = 1 + \big[\hat{P}(\hat{x}-C_x)\hat{P}, \hat{P}(\hat{y}-C_y)\hat{P}\big]\delta_{xy} - \hat{P}(\hat{x}-C_x)\hat{P}(\hat{x}-C_x)\hat{P}\delta_x^2 - \hat{P}(\hat{y}-C_y)\hat{P}(\hat{y}-C_y)\hat{P}\delta_y^2 \tag{5.29}$$

to order $\mathcal{O}(\delta^2)$. Above, $\delta_{xy} = \delta_x \delta_y$ and the square brackets represent the commutator. Next, we expand the logarithm of $U'V'U^{\dagger'}V^{\dagger'}$ to order $\mathcal{O}(\delta^2)$ and get an expression for the local Bott index of the form

$$\begin{aligned}\mathcal{B}(\boldsymbol{x}) = -\frac{L_x L_y}{2\pi} \operatorname{Im} \operatorname{tr}_{\boldsymbol{x}} \Big(&\big[\hat{P}(\hat{x} - C_x)\hat{P}, \hat{P}(\hat{y} - C_y)\hat{P}\big]\delta_{xy} \\ &- \hat{P}(\hat{x} - C_x)\hat{P}(\hat{x} - C_x)\hat{P}\delta_x^2 - \hat{P}(\hat{y} - C_y)\hat{P}(\hat{y} - C_y)\hat{P}\delta_y^2 \Big).\end{aligned} \tag{5.30}$$

The last two terms in the brackets give zero when you take their imaginary part. As well as this, if one expands out the brackets of the first term, any term with a C_x or C_y will disappear due to the commutator and the fact that C_x and C_y are constants and therefore commute with the projectors. From this we then find that to order $\mathcal{O}(\delta^2)$ the local Bott index is given by

$$\mathcal{B}(\boldsymbol{x}) = -\frac{L_x L_y}{2\pi} \operatorname{Im} \operatorname{tr}_{\boldsymbol{x}} \Big(\big[\hat{P}\hat{x}\hat{P}, \hat{P}\hat{y}\hat{P}\big] \Big) \delta_{xy}. \tag{5.31}$$

Finally, using the definition of δ_{xy} we get that

$$\mathcal{B}(\boldsymbol{x}) = 2\pi i \operatorname{tr}_{\boldsymbol{x}} \Big(\big[\hat{P}\hat{x}\hat{P}, \hat{P}\hat{y}\hat{P}\big] \Big) = \mathcal{M}_2(\boldsymbol{x}) \tag{5.32}$$

We have therefore shown that the local Bott index is equal to the Chern marker up to order $\mathcal{O}(\delta^2)$. As such, if L_x and L_y are large then the Chern marker is a good approximation of the Bott index.

Both the Bott index and the Chern marker can accurately predict the system's topological index with open boundary conditions when they are measured far from the edges of the system. This ensures that we are determining the topological index of the bulk and edge state modes do not contribute to the calculation. If periodic boundary conditions are taken then the edge state modes are not present and the position operator is given by $\hat{\boldsymbol{x}}_p$, defined in eq. (5.1). In this case the components of the position operator are discontinuous at certain point in the system. The discontinuous nature of the x component of $\hat{\boldsymbol{x}}_p$ can be seen in fig. 5.1. In this case the Bott index correctly calculates the topological index wherever the local trace is taken. However, this is not the case for the Chern marker which has

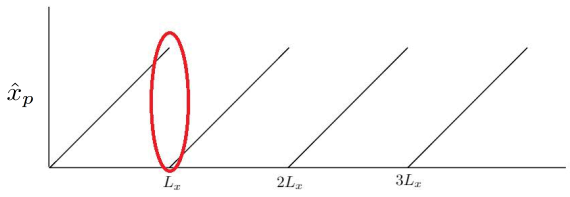

Figure 5.1: Plot showing the discontinuous nature of the x component of the position operator, $\hat{\boldsymbol{x}}_p$. Here, L_x is the system size in the x direction. The red ellipse highlights the discontinuous region.

to be calculated away from the discontinuities in $\hat{\boldsymbol{x}}_p$ in order to correctly predict the topological index of the system. This is due to the fact that around the discontinuities the first order expansion given in eq. (5.29) is not a good approximation and higher order terms need to be considered.

In this section we have shown how to define the local Bott index and have also shown that it is equivalent to the Chern marker in the large system limit. We also pointed out that when open boundary conditions are taken one has to evaluate both the Bott index and the Chern marker far from the edges of the system to ensure they capture the correct value for the topological index. If periodic boundary conditions are taken then the local Bott index correctly predicts the topological index everywhere, but the Chern marker has to be evaluated away from the discontinuities in the position operator.

6

Topological pumping in one dimension

As stated earlier, 1D topological pumps are characterised by the fact that they transmit an integer amount of electrons across the system when evolved over a full time cycle. The number of electrons transported across the system is determined by the first Chern number. As such, the current in the bulk of the system is quantized. As well as this, because the Fermi-energy of the system lies within a band gap of the system the current is robust against perturbations. This is a very attractive electrical property.

Topological pumping in one dimensional time-dependent systems has been explored experimentally in photonic systems [14, 15, 16] and cold atomic gas systems [10, 11, 12, 13], as well as in magneto-mechanical meta-materials and elastic lattice systems [17, 18]. The pumping within these systems can be understood by calculating numerically the change in polarisation, or equivalently the Zak phase, over a time cycle. Alternatively, one can describe the pumping through the shift in the Wannier centres deep within the bulk [20, 70, 23]. The topological index of the system can be discerned from these methods by considering their change over a full time period. One can also use the TKNN form of the Chern number to find the topological index by treating the time dimension as a spatial dimension.

However, most of these methods generally require translational invariance and therefore do not have the same desirable properties that a local topological marker has.

In this chapter our aim is to develop a 1D real-space local topological marker, labelled the 1D marker, that describes the topological pumping of 1D time-dependent systems. To do this we consider the non-interacting Aubry-André model, given in eq. (3.1), and first demonstrate the pumping through the shift in the Wannier centres deep within the bulk. We then develop the 1D marker and show that its change over a full time period is equal to the first Chern number of the system. After this, we show numerically that the evolution of the 1D marker for the Aubry-André model is the same as the Wannier-centre evolution. We also investigate how the 1D marker is affected by the size of the system for the Aubry-André model, highlighting the limit at which the change in the 1D marker starts to fail to represent the topological index of the system. Next, we add different types of disorder to the non-interacting Aubry-André model and use the 1D marker to investigate how this affects the topological index of the system both locally and as a whole. Lastly, we use the 1D marker to investigate the topological phase transitions of the generalised Aubry-André model when the parameters of the system are varied. We find that the system displays numerous phase transitions, some of which are phase transitions between a topological regime and a non-topological regime. All the numerical analysis within this chapter is done on a finite system with open boundary conditions.

6.1 Wannier centre evolution

In this section we introduce Wannier functions and their relation to the polarisation of the system. We then use the Aubry-André model to show numerically that the Wannier centres shift by an integer number of unit cells equal to the Chern number of the system. This behaviour is well known from the modern theory of polarisation [23].

The Aubry-André model has both spatial and temporal translational invariance in the bulk when the value of b is set to a rational fraction. As a result, in this case, the eigenstates of the Aubry-André Hamiltonian are described by Bloch states that are delocalised in real space. One can generate a localised state by superimposing numerous Bloch states with different k values; the more Bloch states used the more localised the new state will be. This is the premise of Wannier functions. A Wannier function is defined as [71, 70]

$$|\mathcal{W}_{xn}\rangle = \frac{1}{V_{\mathrm{BZ}}} \int dk\, e^{-ikx} \, |\psi_{kn}\rangle \,. \tag{6.1}$$

This has a gauge freedom which is used to ensure that the Wannier functions are as localised as possible. The exponential acts to translate the localised state from the origin of the system to the unit cell labelled by the vector x. It can be shown that the Wannier functions form an orthonormal basis

and if we take its Fourier transform we get that

$$|\psi_{kn}\rangle = \sum_x e^{ikx} |\mathcal{W}_{xn}\rangle \,. \tag{6.2}$$

If we then substitute this into the definition of the projector given in eq. (4.2) we see that the projector can be written in terms of the Wannier functions in the following way

$$\hat{P} = \sum_n^{\text{occ}} \int dk \, |\psi_{kn}\rangle \langle \psi_{kn}| = \sum_n^{\text{occ}} \sum_x |\mathcal{W}_{xn}\rangle \langle \mathcal{W}_{xn}| \,. \tag{6.3}$$

Because in our analysis we consider a local trace within the bulk of the system, the edge state modes can be ignored and eq. (6.3) can be used. Ref. [70] gives a more in-depth introduction to Wannier functions and their applications.

It has been shown that Wannier functions can be used to calculate the change in the polarisation of a system via the Wannier centres [20]. To demonstrate this we consider the Wannier centre in the unit cell located at the origin of the system. Using eq. (6.1) and similar techniques used in Section 4.2, it can be seen that

$$\mathcal{W}_{0n} = \sum_n^{\text{occ}} \langle \mathcal{W}_{0n}| \hat{x} |\mathcal{W}_{0n}\rangle = \frac{i}{V_{\text{BZ}}} \sum_n^{\text{occ}} \int dk \, \langle u_{kn}| \partial_{k_x} |u_{kn}\rangle \,. \tag{6.4}$$

The above equation shows the clear link between the polarisation of the system and the Wannier centre near the origin of the system. It can also be shown that the Wannier centre located in an arbitrary unit cell represented by x is given by

$$\mathcal{W}_{xn} = \sum_n^{\text{occ}} \langle \mathcal{W}_{xn}| \hat{x} |\mathcal{W}_{xn}\rangle = x + \frac{i}{V_{\text{BZ}}} \sum_n^{\text{occ}} \int dk \, \langle u_{kn}| \partial_{k_x} |u_{kn}\rangle \,. \tag{6.5}$$

Here x labels the unit cell of the system. From this we see that, because the system is invariant under a time translation T, the change in the Wannier centres over a full time period is given by the Chern number of the time-dependent system;

$$\mathcal{W}_{xn}(T) - \mathcal{W}_{xn}(0) = \frac{i}{V_{\text{BZ}}} \sum_n^{\text{occ}} \int_0^T dt \int dk \left[\left\langle \frac{d}{dt} u_{kn} \middle| \partial_{k_x} u_{kn} \right\rangle - \left\langle \partial_{k_x} u_{kn} \middle| \frac{d}{dt} u_{kn} \right\rangle \right] = C_1^n, \tag{6.6}$$

where C_1^n is the first Chern number of the nth band. It is important to point out that when calculating the time evolution of the Wannier centre numerically there will be a discontinuity with a magnitude equal to the size of the unit cell present. This discontinuity corresponds to the Wannier centre exiting the far end of the unit cell and reentering at the start of the unit cell and is related to the fact that

the polarisation of the system can only be determined modulo 2π. Ignoring this discontinuity one can determine the Chern number of the system.

It was shown by Marzari and Vanderbilt that for 1D systems one can determine the optimally localised Wannier functions by finding the eigenfunctions of the projected position operator $\hat{P}\hat{x}\hat{P}$ [71]. As such, if one wants to analyse the Wannier centres this can be done by finding the eigenvalues of $\hat{P}\hat{x}\hat{P}$. This method applies to both the single band and multiband case. Using this method we can numerically calculate the evolution of the Wannier centres, and thus the polarisation, of the system over a time cycle.

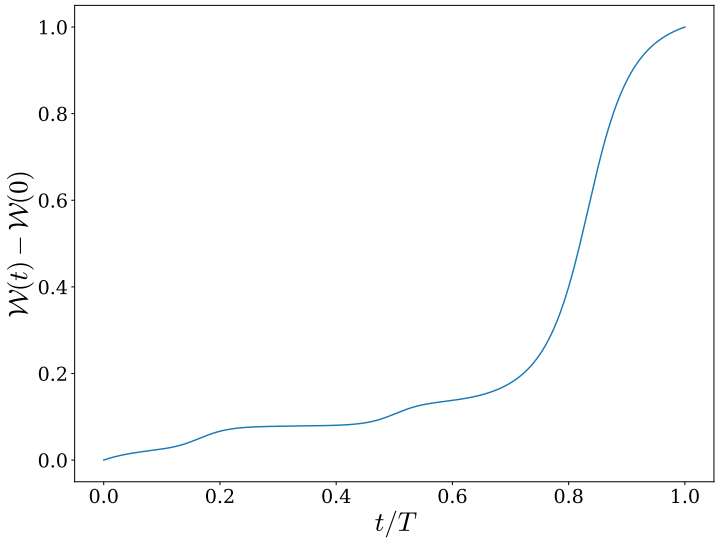

Figure 6.1: The change in a Wannier center, $\mathcal{W}$, deep within the bulk of the system over a full time period for the lowest band of the time-dependent Aubry-André model. The parameters have been set to $\Delta/J = -2$; $b = 1/3$ and the finite system is composed of 40 unit cells. Here we have ignored the discontinuity that arises when the Wannier centre leaves and reenters the unit cell.

Figure 6.1 shows the evolution of a Wannier centre deep within the bulk of the system for the Aubry-André model with only the lowest band populated. We have set $b = 1/3$ and $\Delta/J = -2$ and used the eigenvalues of $\hat{P}\hat{x}\hat{P}$ to determine the Wannier-centre values. We have also ignored the discontinuity that arises when the Wannier centre leaves and reenters the unit cell. It can be seen that the Wannier centre shifts by one lattice constant when evolved over a time period and therefore the first Chern number is 1.

We have thus confirmed numerically that the Chern number of the lowest band of the Aubry-André model is 1 as well as determining how the polarisation of the lowest band evolves over a time period. We will use this evolution later to compare with how the 1D marker evolves over time.

6.2 Adiabatic evolution and operator Berry connection

In this section we introduce the adiabatic evolution operator which is a key concept needed for the derivation of the 1D marker. This allows one to adiabatically evolve the projection operator, $\hat{P}$, in time. We then use this operator to define the operator Berry connection and show how this is related to the conventional Berry connection. We will also use this evolution operator later in this thesis to derive the 3D marker.

Topological pumping systems are normally analysed in the adiabatic regime and as such we restrict ourselves to analysing the dynamics of systems within this regime. The adiabatic regime ensures that if a system begins in the instantaneous ground state it will remain in this state under the following conditions; there is a sufficient gap between the instantaneous ground state and all other states, and the system is evolved slowly enough such that excitations across this gap cannot take place. To ensure we remain within the adiabatic regime we use the adiabatic evolution operator, which is an effective time-evolution operator, to evolve the system in time. Using this operator, as opposed to the true time-evolution operator, is a matter of convenience and all results will hold for the true time-evolution of the system as long as one remains within the adiabatic regime.

To derive the form of the adiabatic evolution operator we start by stating the relation we desire;

$$\hat{P}(t) = \hat{U}\hat{\bar{P}}\hat{U}^{\dagger}. \tag{6.7}$$

The operator $\hat{U}$ is the adiabatic evolution operator which adiabatically connects the initial projector $\hat{\bar{P}}$ to the projector $\hat{P}(t)$ which projects onto the occupied instantaneous eigenstates at time t. The bar on an operator denotes that it is evaluated at time $t = 0$. The adiabatic evolution operator $\hat{U}$ obeys

$$i\frac{d}{dt}\hat{U} = \hat{h}\hat{U} \tag{6.8}$$

with the initial condition $\hat{U}(t = 0) = 1$. Above, $\hat{h}$ is an effective Hamiltonian which describes the evolution of the system in the adiabatic regime. To find the form of $\hat{h}$ we take the time derivative of eq. (6.7) and substitute in eq. (6.8) and its Hermitian conjugate. Doing this we get

$$\dot{\hat{P}} = -i[\hat{h}, \hat{P}], \tag{6.9}$$

where $\dot{\hat{P}} = \frac{d}{dt}\hat{P}$. We then use this to get the relations

$$\dot{\hat{P}}\hat{P} = -i(\hat{h}\hat{P} - \hat{P}\hat{h}\hat{P}) \tag{6.10}$$

$$\hat{P}\dot{\hat{P}} = -i(\hat{P}\hat{h}\hat{P} - \hat{P}\hat{h}). \tag{6.11}$$

Using these it can be shown that

$$i([\dot{\hat{P}}, \hat{P}])\hat{P} = \hat{h}\hat{P} - \hat{P}\hat{h}\hat{P}. \tag{6.12}$$

From eq. (6.9) we know that $\hat{h}$ has to be given by some function of $\dot{\hat{P}}\hat{P}$, $\hat{P}\dot{\hat{P}}$. It can also be shown using the projector relation $\dot{\hat{P}} = \frac{d}{dt}(\hat{P}^2) = \hat{P}\dot{\hat{P}} + \dot{\hat{P}}\hat{P}$ it can be shown that $\hat{P}\dot{\hat{P}}\hat{P} = 0$. As such, the last term in eq. (6.12) has to give zero and therefore the form of $\hat{h}$ is given by [72, 73]

$$\hat{h} = i[\dot{\hat{P}}, \hat{P}]. \tag{6.13}$$

One can also show that the above equation satisfies eq. (6.9) by using the explicit form of the projector. We have thus shown that one can construct the adiabatic evolution operator by solving eq. (6.8) using $\hat{h}$ defined above. Further more, this adiabatic evolution retains the correct Berry phase information of the original time-dependent Hamiltonian.

We would like to point out that so far we have not assumed anything but adiabatic evolution and therefore the results up to this point apply to any Hamiltonian as long as it stays within the adiabatic regime. If, however, one has a translationally invariant system then $\hat{h}$ can be simplified to

$$\hat{h} = \int d\boldsymbol{k}\, |\boldsymbol{k}\rangle \langle \boldsymbol{k}| \otimes \hat{\mathfrak{h}}_{\boldsymbol{k}} \tag{6.14}$$

where the translationally invariant part of the effective Hamiltonian is given by $\hat{\mathfrak{h}}_{\boldsymbol{k}} = i[\dot{\hat{\mathcal{P}}}, \hat{\mathcal{P}}]$. As a result, the adiabatic evolution operator simplifies to

$$\hat{U} = \int d\boldsymbol{k}\, |\boldsymbol{k}\rangle \langle \boldsymbol{k}| \otimes \hat{\mathcal{U}}_{\boldsymbol{k}}. \tag{6.15}$$

Throughout this chapter we will only consider time-dependent systems that preserve discrete translational invariance and therefore eq. (6.14) and eq. (6.15) will apply. With this we can write $\hat{\mathcal{U}}_{\boldsymbol{k}}$ explicitly as

$$\hat{\mathcal{U}} = \sum_n |u_{\boldsymbol{k}n}(t)\rangle \langle u_{\boldsymbol{k}n}(0)| \tag{6.16}$$

where the cell periodic states $|u_{\boldsymbol{k}n}(t)\rangle$ are the instantaneous eigenstates of the Bloch Hamiltonian and can be used to generate the projectors $\hat{\mathcal{P}}_{\boldsymbol{k}}(t) = \sum_n^{\text{occ}} |u_{\boldsymbol{k}n}(t)\rangle \langle u_{\boldsymbol{k}n}(t)|$ and $\hat{\mathcal{Q}}_{\boldsymbol{k}(t)} = \sum_n^{\text{unocc}} |u_{\boldsymbol{k}n}(t)\rangle \langle u_{\boldsymbol{k}n}(t)|$.

There is a subtlety with the above equation which is that the cell periodic states above do not in general correspond to the eigenvectors of the Bloch Hamiltonian of the original system but can be made up of a collection of eigenvectors of the original Hamiltonian.

To show this subtlety we label the eigenstates of the original Bloch Hamiltonian as $|\tilde{u}_{n\boldsymbol{k}}\rangle$ and therefore $\hat{\mathcal{P}}_{\boldsymbol{k}} = \sum_n^{\text{occ}} |\tilde{u}_{n\boldsymbol{k}}\rangle \langle \tilde{u}_{n\boldsymbol{k}}|$ and similar for $\hat{\mathcal{Q}}_{\boldsymbol{k}}$. We then define a collection of states within the occupied space as $|u_{\boldsymbol{k}n}\rangle = \sum_{n'}^{\text{occ}} V_{n'n} |\tilde{u}_{\boldsymbol{k}n}\rangle$ where $V_{n'n}$ are elements of a unitary matrix. One can show straightforwardly that $\hat{\mathcal{P}}_{\boldsymbol{k}}$ is unchanged when $|u_{\boldsymbol{k}n}\rangle$ is replaced with $|\tilde{u}_{\boldsymbol{k}n}\rangle$. We can then use this symmetry to bring $\mathfrak{h}_{\boldsymbol{k}}$ into a more simple form. We chose V such that $\langle u_{\boldsymbol{k}n}|\partial_t u_{\boldsymbol{k}n'}\rangle = 0$ for any n and n' corresponding to occupied states. Such a unitary matrix can be found by by solving the following matrix differential equation

$$i\partial_t V_{nn'} = -\sum_{n''}^{\text{occ}} C_{nn''} V_{n''n'} \tag{6.17}$$

with $V_{nn'}(t=0) = \delta_{nn'}$ and $C_{nn''} = i\langle \tilde{u}_{\boldsymbol{k}n}|\partial_t \tilde{u}_{\boldsymbol{k}n''}\rangle$. In practice one does not have to solve the above equation but only know that such a unitary matrix exists. This procedure can also be repeated to find $|u_{\boldsymbol{k}n}\rangle$ for the unoccupied states of the system. With this we can now write $\mathfrak{h}_{\boldsymbol{k}}$ in the following way

$$\mathfrak{h}_{\boldsymbol{k}} = i[\dot{\hat{\mathcal{P}}}_{\boldsymbol{k}}, \hat{\mathcal{P}}_{\boldsymbol{k}}] = i\dot{\hat{\mathcal{P}}}_{\boldsymbol{k}}\hat{\mathcal{P}}_{\boldsymbol{k}} + i\dot{\hat{\mathcal{Q}}}_{\boldsymbol{k}}\hat{\mathcal{Q}}_{\boldsymbol{k}} = i\sum_n |\partial_t u_{\boldsymbol{k}n}\rangle \langle u_{\boldsymbol{k}n}| \tag{6.18}$$

where in the last equality we have used the fact that $\langle u_{\boldsymbol{k}n}|\partial_t u_{\boldsymbol{k}n'}\rangle = 0$ when n and n' label occupied bands or when they label unoccupied bands which is enforced by our choice of the unitary matrix V. We have thus shown that while the states defining the adiabatic evolution operator in eq. (6.16) are not the eigenvectors of Bloch Hamiltonian one can still use these to determine observables of the system. The above considerations are only important when one is considering multiple occupied bands and are not necessary when a single band is occupied.

With the adiabatic evolution operator defined, we now use it to define the operator Berry connection in the following way

$$\hat{\mathcal{A}}_i = \int d\boldsymbol{k}\, |\boldsymbol{k}\rangle \langle \boldsymbol{k}| \otimes \hat{\mathcal{A}}_i \qquad \text{with} \qquad \hat{\mathcal{A}}_i = i\,\hat{\bar{\mathcal{P}}}\hat{\mathcal{U}}^\dagger(\partial_i \hat{\mathcal{U}})\hat{\bar{\mathcal{P}}}. \tag{6.19}$$

Again, the bar on $\hat{\bar{\mathcal{P}}}$ denotes that it is evaluated at $t = 0$. This expression has similarities with the Berry connection used in Ref. [74]. It is clear from the name of $\hat{\mathcal{A}}_i$ that we are implying that it is some how connected to the conventional Berry connection given by $\tilde{\mathcal{A}}_i^{nm} = i\langle u_{\boldsymbol{k}n}|\partial_i\, u_{\boldsymbol{k}m}\rangle$, where n and m label occupied bands. To show that it is, we use eq. (6.16) along with the definition of $\hat{\mathcal{P}}$ in eq. (6.19) and get

$$\hat{\mathcal{A}}_i = \sum_{nm}^{\text{occ}} |u_{\boldsymbol{k}n}(0)\rangle \langle u_{\boldsymbol{k}m}(0)| \left(\tilde{\mathcal{A}}_i^{nm}(t) - \tilde{\mathcal{A}}_i^{nm}(0)\right). \tag{6.20}$$

From this we see that the operator Berry connection gives the change in the conventional Berry connection between an initial time $t = 0$ and some later time t. With this we are now ready to define the 1D marker.

6.3 The 1D marker

We now derive the 1D marker, which is a real-space local topological marker that determines the first Chern number of a system. Within this section all local traces will be taken within the bulk of the system such that edge state modes can be ignored.

In the previous section we determined the evolution of the Wannier centre by finding the eigenvalues of the matrix $\hat{P}\hat{x}\hat{P}$. This may motivate one to consider the local trace of this matrix as a potential candidate for the 1D marker. We consider this below and get

$$\mathrm{tr}_x(\hat{P}\hat{x}\hat{P}) = \mathrm{tr}_x(\hat{x}\hat{P}) - \mathrm{tr}_x(\hat{Q}\hat{x}\hat{P}). \tag{6.21}$$

Analysing the second term from the above equation using the form of $\hat{P}\hat{x}\hat{Q}$ given in eq. (4.12) we get that

$$\begin{aligned}\mathrm{tr}_x(\hat{Q}\hat{x}\hat{P}) &= \sum_n^{\mathrm{occ}} \sum_m^{\mathrm{unocc}} \sum_\alpha \int dk \Big(|\langle k|x\rangle|^2 \otimes i \langle \alpha|u_{kn}\rangle \langle u_{kn}|\partial_i u_{km}\rangle \langle u_{km}|\alpha\rangle \Big) \\ &= \sum_n^{\mathrm{occ}} \sum_m^{\mathrm{unocc}} \frac{i}{V_{\mathrm{BZ}}} \int dk \mathrm{Tr}_\alpha \big(|u_{kn}\rangle \langle u_{kn}|\partial_i u_{km}\rangle \langle u_{km}| \big)\end{aligned} \tag{6.22}$$

where $\mathrm{Tr}_\alpha(\hat{O}) = \sum_\alpha \langle\alpha|\hat{O}|\alpha\rangle$ is a trace over all the internal degrees of freedom of the unit cell. Because this trace only includes the internal states $|u_{kn}\rangle$ of the unit cell and its derivatives the cyclic permutation properties of the full trace also apply here. Using the fact that $\langle u_{km}|u_{kn}\rangle = 0$ for $n \neq m$ we see that the above equation gives zero and therefore we get that

$$\mathrm{tr}_x(\hat{P}\hat{x}\hat{P}) = xN_c \tag{6.23}$$

where N_c denotes the number of particles within the unit cell; for the case where only one band is populated $N_c = 1$. This shows that the local trace of the matrix $\hat{P}\hat{x}\hat{P}$ is constant for all snapshots in time and therefore the pumping within the system is not reflected in this local quantity.

However, we could try to evolve the matrix $\hat{P}\hat{x}\hat{P}$ with adiabatic time evolution operators and then take the local trace. This way the history of the system is retained. We will now therefore consider

$$\mathcal{M}_1(x,t) = \frac{1}{V_c}\mathrm{tr}_x\big(\hat{U}^\dagger\hat{P}(t)\hat{x}\hat{P}(t)\hat{U}\big) = \frac{1}{V_c}\mathrm{tr}_x\big(\hat{\tilde{P}}\hat{U}^\dagger\hat{x}\hat{U}\hat{\tilde{P}}\big). \tag{6.24}$$

It turns out that the above quantity does indeed possess the desired time dependence and we will therefore identify it as the 1D marker. The prefactor $\frac{1}{V_c}$, where V_c is the volume of the unit cell (or the lattice constant in 1D), has been included to make the 1D marker dimensionless. From this point, for ease of notation, we will suppress the time notation and denote $\hat{P}(t)$ as just $\hat{P}$.

We now show that the change in the 1D marker over a full time period gives the first Chern number of the system. To do this we start by analysing $\hat{U}^\dagger \hat{x} \hat{U}$ using eq. (6.15) to get

$$\hat{U}^\dagger \hat{x} \hat{U} = \int dk dk' \, |k\rangle \langle k| \, \hat{x} \, |k'\rangle \langle k'| \otimes \hat{\mathcal{U}}_k^\dagger \hat{\mathcal{U}}_{k'}. \tag{6.25}$$

We showed earlier that $\langle k| \, \hat{x} \, |k'\rangle = \frac{1}{V_{\text{BZ}}} \sum_x -i\partial_{k'}(e^{i(k'-k)x})$. Using this in the above equation and integrating by parts we get

$$\hat{U}^\dagger \hat{x} \hat{U} = \int \frac{dk dk'}{V_{\text{BZ}}} \sum_x e^{i(k'-k)x} \, |k\rangle \, i\partial_{k'} \langle k'| + \int \frac{dk dk'}{V_{\text{BZ}}} \sum_x e^{i(k'-k)x} \, |k\rangle \langle k'| \otimes i\hat{\mathcal{U}}_k^\dagger \partial_{k'} \hat{\mathcal{U}}_{k'}, \tag{6.26}$$

where we have used the fact that the total derivative vanishes due to the periodicity of the system in the bulk. Using the definition of $|k\rangle$ given in eq. (2.5) as well as the identity $\frac{1}{V_{\text{BZ}}} \sum_x e^{i(k'-k)x} = \delta(k'-k)$ it can be shown that

$$\hat{U}^\dagger \hat{x} \hat{U} = \hat{x} + \int dk \, |k\rangle \langle k| \otimes i\hat{\mathcal{U}}_k^\dagger \partial_k \hat{\mathcal{U}}_k. \tag{6.27}$$

Using the above equality and eq. (6.19) it is easy to show that

$$\hat{\hat{P}} \hat{U}^\dagger \hat{x} \hat{U} \hat{\hat{P}} = \hat{\hat{P}} \hat{x} \hat{\hat{P}} + \hat{A}. \tag{6.28}$$

This establishes a direct relationship between the evolved position operator and the change in the Berry connection over time. A similar relationship exists in the semi-classical dynamics of wave-packets in lattice systems [75]. Noting that the 1D marker is defined as the local trace of the right hand side of eq. (6.28) it can then be seen that

$$\mathcal{M}_1(x,t) = \frac{N_c}{V_c} x + \frac{1}{2\pi} \int dk \, \text{Tr}_\alpha(\hat{\mathcal{A}}). \tag{6.29}$$

It was shown in eq. (6.20) that $\hat{\mathcal{A}}$ is related to the change of the Berry connection over time. Using this relation it can then be seen that the 1D marker is given by

$$\mathcal{M}_1(x,t) = \frac{N_c}{V_c} x + \frac{i}{2\pi} \sum_n^{\text{occ}} \int dk \, \Big(\langle u_{kn}(t)| \, \partial_k u_{kn}(t)\rangle - \langle u_{kn}(0)| \, \partial_k u_{kn}(0)\rangle \Big), \tag{6.30}$$

where x labels the unit cell at time $t = 0$. The second term in the above equation gives the change

in the polarisation of the system between some initial time $t = 0$ and some later time t. Using the relation between the polarisation and the Wannier centre given in eq. (6.5) one can relate the change in the 1D marker to the change in the Wannier centre between time $t = 0$ and t via the following equation

$$\mathcal{M}_1(x,t) - \mathcal{M}_1(x,0) = \frac{1}{V_c}\Big(\mathcal{W}_x(t) - \mathcal{W}_x(0)\Big). \tag{6.31}$$

From this it is evident that the change in the 1D marker over a full time period, T, gives the Chern number of the system.

We have thus shown that the 1D marker, $\mathcal{M}_1(x,t)$, possesses the correct time dependence to describe the topological pumping within 1D time-dependent systems when it is evaluated in the bulk of the system. Due to its real-space localisation, the 1D marker can be used to investigate the topological structure of 1D time-dependent systems with disorder or other spatial inhomogeneities applied.

Upon reflection, it is not too surprising that the local trace of $\hat{P}\hat{x}\hat{P}$ fails to describe the polarisation of the system. This is due to the fact that one can describe this quantity in terms of the charge density alone and it is known that to determine the polarisation of the system one requires more information than just the charge density of the system. The time evolution present in $\mathcal{M}_1$ provides the required history-dependence needed to determine the polarisation of the system.

6.4 Numerical investigation of the 1D marker

In the previous section we defined the 1D marker and showed that its time evolution, evaluated in the bulk of a system, can be related to the time evolution of the Wannier centres. It is then natural to confirm this relation numerically, which we will do in this section using the Aubry-André model. As well as this, we investigate the change in the 1D marker over a full time period near the edges of the system where the equality between the change in the 1D marker and the first Chern number breaks down.

We start this section with an overview of the numerical procedure used to calculate 1D marker. To calculate $\mathcal{M}_1(x,t)$, one starts by discretising the time interval between 0 and T using sufficiently small time steps Δt. Then, for each discrete time point, the projector $\hat{P}(t)$ is calculated from the instantaneous eigenvalues of $\hat{H}(t)$. Using $\hat{P}$ at times $t-\Delta t$ and $t+\Delta t$, $\dot{\hat{P}}$ can then be calculated using the finite difference method. With both $\hat{P}(t)$ and $\dot{\hat{P}}(t)$ the effective Hamiltonian $\hat{h}$ can be constructed using eq. (6.13). With the initial condition $\hat{U}(0) = \mathbb{1}$, the time evolution operator for subsequent times can be computed using $\hat{U}(t+\Delta t) = e^{-i\hat{h}(t)\Delta t}\hat{U}(t)$, which contains an error of order $(\Delta t)^2$ but remains unitary up to numerical accuracy. Lastly, one uses eq. (6.24) to calculate $\mathcal{M}_1(x,t)$. The convergence in the time spacing of Δt should be checked.

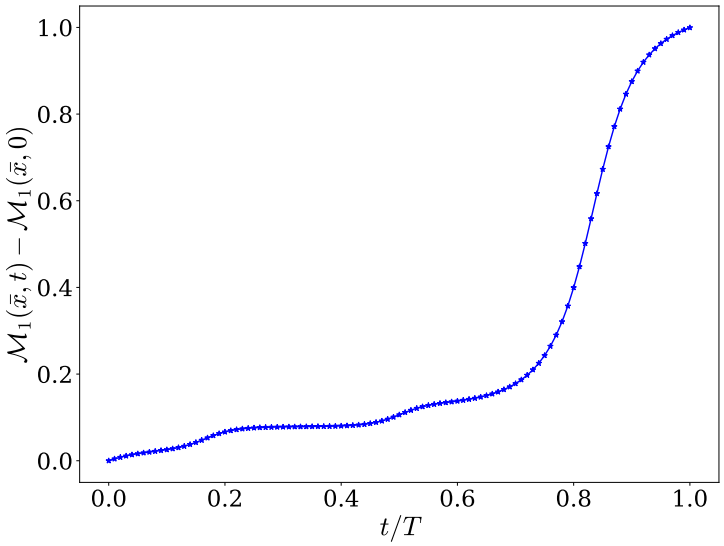

Figure 6.2: The change in the 1D marker $\mathcal{M}_1(x,t)$ over a full time period for the lowest band of the Aubry-Andre model with same parameters as Figure 6.1. The local trace was taken over the 20th unit cell, $x = 20$, for a system size of 40 unit cells.

With the numerical procedure outlined we now analyse the evolution of $\mathcal{M}_1(x,t)$ over a time period. Equation (6.31) highlights the relation between the evolution of the 1D marker and the evolution of the Wannier centres showing that, in the bulk, the evolution of the 1D marker should be identical to the evolution of the Wannier centres when the volume of the unit cell is set to unity, $V_c = 1$.

Figure 6.2 shows the evolution of $\mathcal{M}_1$ over time for a finite system with open boundary conditions. We have set the volume of the unit cell to unity and used a system size of 40 unit cells. We have taken the local trace over the 20th unit cell of the system to ensure $\mathcal{M}_1$ is evaluated within the bulk of the system. From this figure it can be seen that that the evolution of $\mathcal{M}_1$ and the evolution of the Wannier centre, shown in Figure 6.1, is very similar and comparing the two directly shows that they match quantitatively. This numerically confirms eq. (6.31). It should also be noted that one does not have to worry about discontinuities when evaluating the 1D local topological marker due to its local nature.

The agreement between the change in $\mathcal{M}_1(x,t)$ over a full time period and the first Chern number deteriorates when the local trace of $\mathcal{M}_1$ is taken over a unit cell close to the boundary of the system. This is due to the fact that the approximation of treating the system as translationally invariant breaks down towards the edges of the system. In fact it can easily be shown that the sum of the local 1D

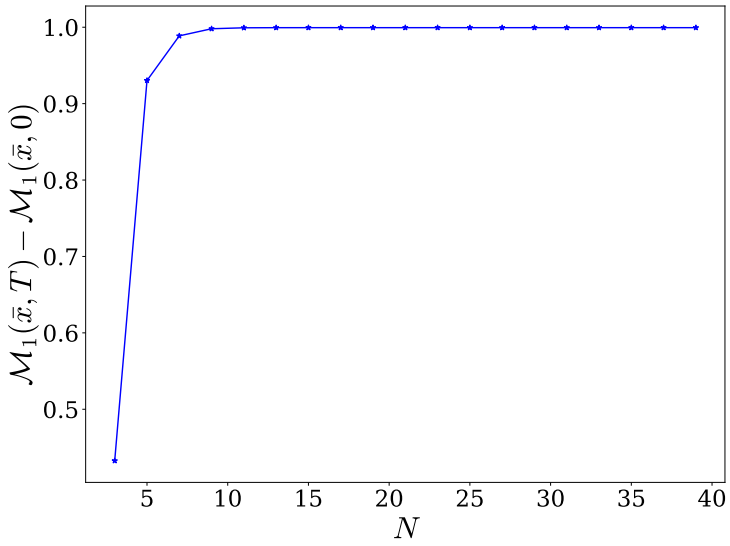

Figure 6.3: The change in the 1D marker $\mathcal{M}_1(x,t)$ over a full time period for varying systems sizes for the lowest band of the Aubry-Andre model with same parameters as Figure 6.1. N is the total number of unit cells within the system. The local trace was taken over the centre most unit cell of the system.

marker over the whole system, $\sum_x \mathcal{M}_1(x)$, is time independent. This is shown in the following way

$$\sum_x \mathcal{M}_1(x,t) = \frac{1}{V_c}\sum_x \mathrm{tr}_x\big(\hat{U}^\dagger \hat{P}\hat{x}\hat{P}\hat{U}\big) = \frac{1}{V_c}\mathrm{Tr}\big(\hat{U}^\dagger \hat{P}\hat{x}\hat{P}\hat{U}\big) = \frac{1}{V_c}\sum_x \mathrm{tr}_x\big(\hat{P}\hat{x}\hat{P}\big). \tag{6.32}$$

Using eq. (6.23) it can be seen that the last equality in eq. (6.32) is time independent, confirming that the sum of the local 1D marker over the whole system is time independent.

Given the above argument, it is then natural to ask where the 1D marker has to be evaluated to give an accurate representation of the first Chern number. To address this question we evaluate the 1D marker within the centre most unit cell of the Aubry-André model for varying system sizes. Figure 6.3 shows how the change of $\mathcal{M}_1(x,t)$ over a full time period depends on the size of the system. From this figure it can be seen that the change in $\mathcal{M}_1$ increases rapidly until it approaches the value of 1, which happens around a system size of $N = 9$. This then shows that, for the Aubry-André model with $\Delta/J = -2$ and $b = 1/3$, $\mathcal{M}_1$ correctly predicts the topology of the system if one analyses a unit cell 5 lattice vectors or more from the edges of the system and thus translational invariance can be assumed in this case. Because the bulk can be defined as the area in which edge state modes have negligible effect, fig. 6.3 then suggests that the probability density of the edge state modes rapidly decay away from the edges of the system and have a negligible effect at distances of 5 unit cells or greater from the

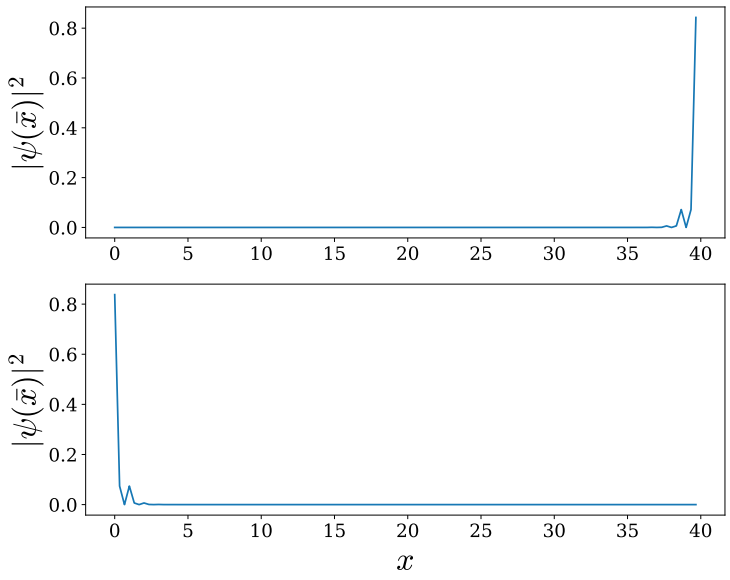

Figure 6.4: A plot showing the amplitude squared of the edge state modes shown in red in Figure 3.1 for $t/T = 0.82$ (top) and $t/T = 0.84$ (bottom). The Aubry-André model was set with same parameters as Figure 6.1 for a system size of 40 unit cells.

edge of the system. We analyse this in Figure 6.4 by plotting the probability density of the edge state mode highlighted in red in Figure 3.1 at 2 different times; one at $t/T = 0.82$ when the edge state mode is localised on the right of the system, and one at $t/T = 0.84$ when the edge state mode is localised on the left of the system. From this it can be seen that the edge state modes of the Aubry-André model do rapidly decay. Further analysis shows that this decay is exponential in nature and by 5 unit cells in from the systems edges the probability density of the edge state modes are 5×10^{-5} or less. This supports the statement that 5 unit cells from the edge of the system the edge state modes have negligible effect and therefore translational invariance can be assumed.

We have thus confirmed that the 1D marker accurately reflects the polarisation of a 1D time-dependent topological system when analysed in the bulk, with the bulk of the system being defined such that the edge state modes of the system are negligible. We have also confirmed that the change in $\mathcal{M}_1$ over a full time period accurately reflects the topological index of the system given by the Chern number.

6.5 Disorder and the 1D marker

It was mentioned earlier that, due to its local nature, the 1D marker could be used to investigate disorder within a system. Within this section we will apply disorder to the Aubry-André model and show that the topological index of the system is robust to disorder when the bands of the system remain gapped.

To analyse how disorder affects the topological index of a system, we first introduce disorder into the Aubry-André model by adding a random on-site potential in the following way

$$\hat{H}_\omega = \hat{H}_{AA} + W \sum_n \omega_n |n\rangle \langle n| , \tag{6.33}$$

where ω_n takes on random values between $-\frac{1}{2}$ and $\frac{1}{2}$ and W is a constant which sets the strength of the random disorder. By setting W to different values this allows us to control the strength of the disorder and analyse how the topology is affected by different disorder strengths.

Figure 6.5 shows the change of the 1D marker, $\mathcal{M}_1$, over a time period averaged over 100 different random matrices for a range of disorder strengths, W. We set the Fermi-energy to $\varepsilon_F/J = -1.3$ such that we project into the same gap considered in fig. 6.1. It also shows the corresponding average band gap size as well as the percentage of random matrices which caused the band gap to close. This analysis was carried out on a system size of 40 unit cells with $\Delta/J = -2$ and $b = 1/3$. From this figure we see that the topology of the system remains unaffected until the disorder strength is $W/J = 2.3$. At this disorder strength the on-site energy term due to disorder can take on a magnitude of 1.15, which is comparable to the size of the band gap when $W/J = 0$. As such, at this disorder strength the random disorder is strong enough to close the band gap. From this figure we therefore see that the value of the 1D marker is only affected by disorder strengths which are comparable to the band gap size at $W/J = 0$. This then suggests that the topological pumping of the system is robust against random disorder as long as the disorder strength is not comparable to the band gap at $W/J = 0$.

The 1D marker also allows us to investigate how a point defect in the system affects the topology of the system locally. This investigation is only possible with the 1D marker due to its local nature. To carry out this investigation we again use the Aubry-André model and add an on-site energy shift of size W to a lattice point within the system. This is achieved by using $\hat{H}_\omega$ and setting $\omega_n = \delta_{n,m}$ where m labels the site in which you wish to place the point defect.

Figure 6.6 shows the change in $\mathcal{M}_1(x,t)$ over a time period for each unit cell within the system for the Aubry-André model with a point defect located on the first site of the 20th unit cell. The point defect has a disorder strength of $W/J = 0.2$. This figure shows that the change in $\mathcal{M}_1(x,t)$ in the bulk of the system is quantized to 1 throughout the bulk and the topology of the system is not affected by a

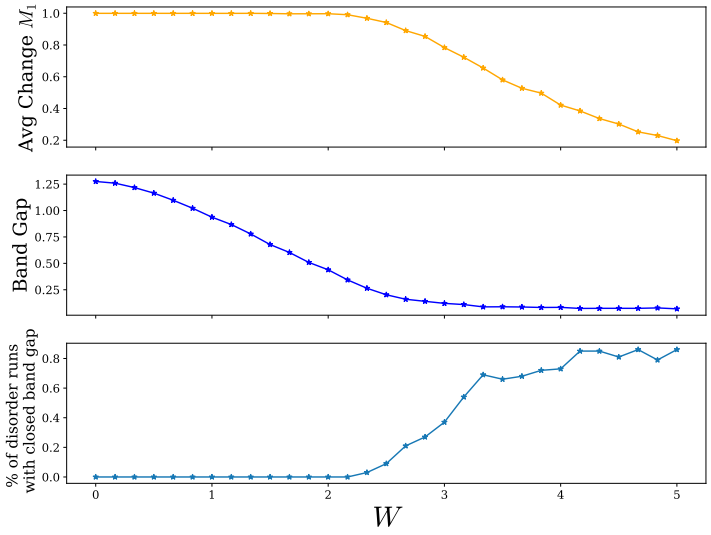

Figure 6.5: A plot showing the change in $\mathcal{M}_1$ over a full time period for $\hat{H}_\omega$ with varying disorder strength, W, which is measured in units of J. For each value of W $\mathcal{M}_1$ was averaged over 100 different disorder matrices. The plot also shows the corresponding average size of the band gap along with the percentage of disorder matrices which caused the band gap to close. The parameters of the Aubry-André model were the same as in fig. 6.1 and the system size was set to 40 unit cells. The Fermi-Energy was set to $\varepsilon_F/J = -1.3$ such that we consider the same gap considered in fig. 6.1.

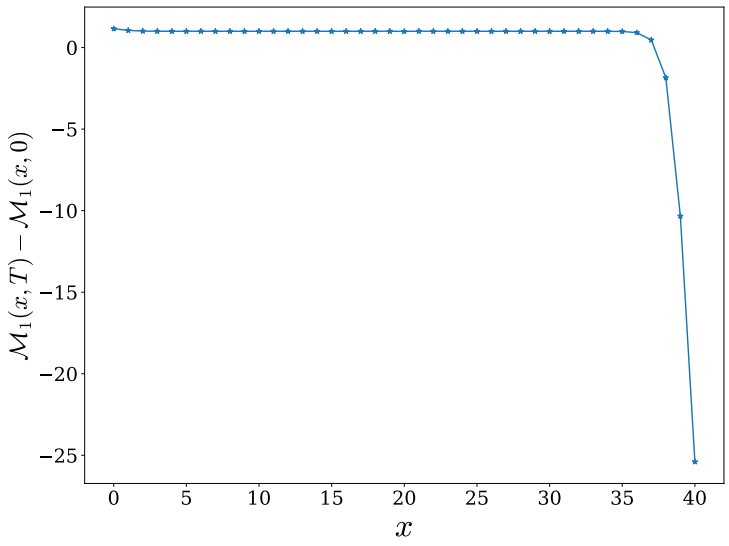

Figure 6.6: The energy spectrum of the Aubry-André model with a point defect of strength $W = 0.2$ located on the first site of the 20th unit cell. The parameters of the system and the Fermi-energy are the same as in Figure 6.5 and the system contains 40 cells.

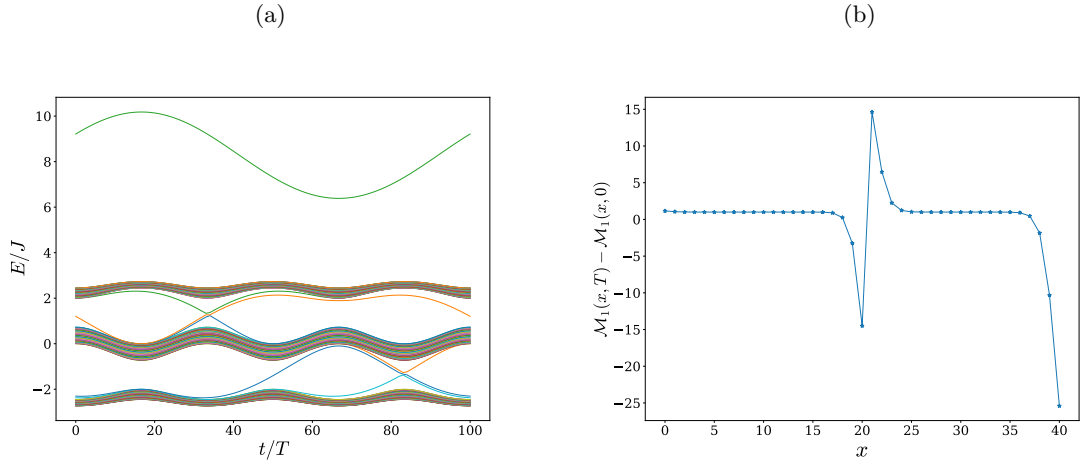

Figure 6.7: (a) The energy spectrum of the Aubry-André model with a point defect of strength $W/J = 8$ located on the first site of the 20th unit cell. The parameters of the system are the same as in Figure 6.1 and the system contains 40 cells. (b) The change in $\mathcal{M}_1$ over a time period for each unit cell within the system for the Aubry-André model with a point defect located on the first site of the 20th unit cell. The disorder strength, parameters and system size are the same as in (a) and the Fermi-energy was set to $\varepsilon_F/J = -1.3$.

disorder strength of $W/J = 0.2$. Next, we will analyse the change in $\mathcal{M}_1(x,t)$ throughout the system for a larger disorder strength and see how this affects the local topology.

Figure 6.7a shows the energy spectrum for the Aubry-André model with a point defect of strength $W/J = 8$ and Figure 6.7b shows the corresponding change in $\mathcal{M}_1(x,t)$ over a full time period for each unit cell. The energy spectrum shows that there are now three modes which traverse the bottom band gap, however, it can be shown that only two are localised on the edges of the system and the other is delocalised across the whole system. To calculate the change in $\mathcal{M}_1(x,t)$ over a time period for this model the projector $\hat{P}$ is projected into all the eigenstates below the Fermi-energy $\varepsilon_F/J = -1.3$. Figure 6.7b shows that around the point defect the change in $\mathcal{M}_1(x,t)$ is no longer quantized, however, the change in $\mathcal{M}_1$ away from the defect remains quantized to the topology of the system. This then suggests that the pumping behaviour still exists far from the defect. It is also interesting to point out that the average of $\mathcal{M}_1$ over the bulk of the system is still equal to the topology of the system and therefore may suggest that topological pumping through the system remains even when strong local disorder is applied to the system. It is clear that further investigation is needed to fully understand how strong disorder affects the topological structure of the system as well as how it affects the topological properties that can arise.

In this section we have shown that if one adds disorder to to a 1D time-dependent topological system through a random disorder matrix then the system retains its topological pumping until the disorder strength is strong enough to close the band gap. We have also shown that if one adds a point like

defect to the system only the topological index around the defect is affected and the topological index far from the defect remains quantized. We also pointed out that the average value of the topological index over the bulk remains quantized even in the presence of a strong local defect, however, further investigation is needed to determine if topological pumping through the system remains in the presence of a strong point like defect.

6.6 Topological phase transitions of the generalised Aubry-André model

In previous sections we have chosen to investigate the topological structure of the Aubry-André model using the 1D marker. There exists a more general version of the Aubry-André model aptly named the generalised Aubry-André (GAA) model. This model was first introduced by Ganeshan *et al.* and possesses cosine modulations, identical to the one present in the AA model, for both the hopping terms and the on-site terms of the Hamiltonian. It has been shown that this model can display topological properties when just the on-site cosine modulation is considered or just the hopping cosine modulation is considered [50]. It is then interesting to ask whether richer topological behaviour can arise in the GAA model compared to the Aubry-André model along with whether the topological properties of this system can be tuned by the hopping strength and other parameters of the system. In this section we will show that the topological index of the GAA model is dependent on the ratio between the amplitude of the hopping modulation and the amplitude of the on-site modulation as well as dependent on the ratio between the time periods of each modulation.

We start by introducing the generalised Aubry-André model Hamiltonian below;

$$H_{GAA} = \sum_n \Big[J + V_2 \cos\Big(2\pi b n + \frac{2\pi t}{T_2}\Big)\Big] |n+1\rangle \langle n| + h.c. \\ + \sum_n V_1 \cos\Big(2\pi b n + \frac{2\pi t}{T_1}\Big) |n\rangle \langle n| \tag{6.34}$$

Here J is a fixed hopping parameter, V_2 and T_2 set the amplitude and the time period of the hopping cosine modulation respectively, V_1 and T_1 set the amplitude and the time period of the on-site cosine modulation respectively and b determines whether the cosine modulations are commensurate with the lattice structure. We will set $b = 1/3$ throughout this section and therefore consider modulations that are commensurate with the lattice structure. Because the system has two cosine modulations with different time periods the full time period of the system is given by the lowest common multiple of T_1 and T_2.

With the GAA Hamiltonian defined we will now use the 1D marker to investigate the topological

index of each gap for varying values of V_2/V_1, T_2/T_1 and J. We first analyse the system with $J = 1$ and vary the ratios V_2/V_1 and T_2/T_1. Figure 6.8 shows the topological phase diagrams for the GAA model when these parameters are varied. The value of the change in $\mathcal{M}_1$ over a full time period is indicated by the colour in the phase diagram with the colour bar assigning each colour a numerical value.

Figure 6.8a is the topological phase diagram for the GAA model with the bottom band populated only with $J = 1$. We can see from this diagram that for most of the values of V_2/V_1 and T_2/T_1 the change in $\mathcal{M}_1$ over a full time period is -1. When the V_2/V_1 is small the change in $\mathcal{M}_1$ varies from the value -1 but does not seem to settle on a specific value. When the value of $\mathcal{M}_1$ does not equal an integer this indicates that the gap in the system has closed. This closing of the gap is required for the topological index of the system to change value. As such, the behaviour seen for small values of V_2/V_1 indicates that if a gap opens up it is small and can close again with a small change in the parameters of the system. This then tells us that while the value of the topological index may deviate from -1 for small V_2/V_1 its new topological index is not stable.

Figure 6.8b shows the topological phase diagram of the GAA model with the bottom band and the second to bottom band populated and $J = 1$. Again, we see that for the majority of values of V_2/V_1 and T_2/T_1 the change in $\mathcal{M}_1$ over a full time period is 1. We also see that the change in $\mathcal{M}_1$ for small values of V_2/V_1 varies from the value 1, but again this new value is not stable. However, this is not the case for $T_2/T_1 = 2$. In this case when V_2/V_1 takes on values between 0.1 and 0.4 the change in $\mathcal{M}_1$ is equal to 2 meaning that the topological index of the system for these parameters is 2. We also see that when V_2/V_1 takes on values between 0.5 and 1 the change in $\mathcal{M}_1$ deviates from this integer value and when V_2/V_1 takes on values greater than 1 the change in $\mathcal{M}_1$ equals 1 meaning the topological index of the system is 1. This is an example of a topological phase transition where the system has a topological index of 2 and by varying the parameters of the system the topological gap closes and then reopens with a different topological index of 1.

The phase diagrams shown in fig. 6.8 above considered the GAA model with $J = 1$ meaning that even if $V_2 = 0$ the Hamiltonian still has a non-zero hopping term. We observed that for this case the topological index of the system was largely the same for different values of the parameters. It is then interesting to ask whether more interesting topological phase transitions would exist if $J = 0$ such that the hopping term of the GAA Hamiltonian was solely determined by the cosine modulation. The topological phase transitions of the GAA model with $J = 0$ are shown in fig. 6.9. It can immediately be seen that setting $J = 0$ causes the system to exhibit a much more varied array of topological values.

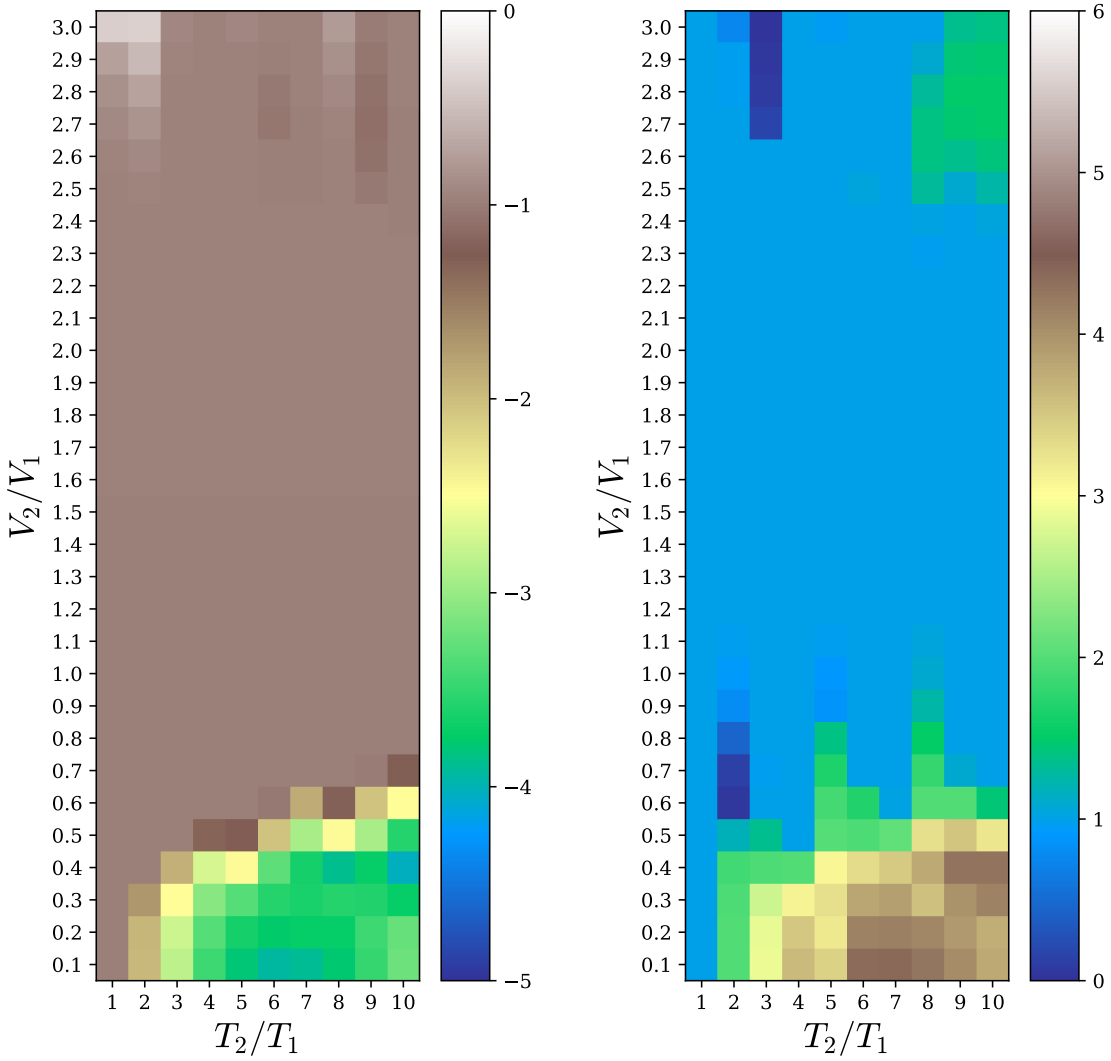

(a) (b)

Figure 6.8: Topological phase diagrams of the Generalised Aubry-André model with $J = 1$. The topological index of the system is indicated by colour. We vary the ratio of the amplitudes V_2/V_1 along with the ratio of the time periods T_2/T_1. (a) The topological phase diagram for GAA model with the bottom band populated. (b) The topological phase diagram for GAA model with the bottom two bands populated.

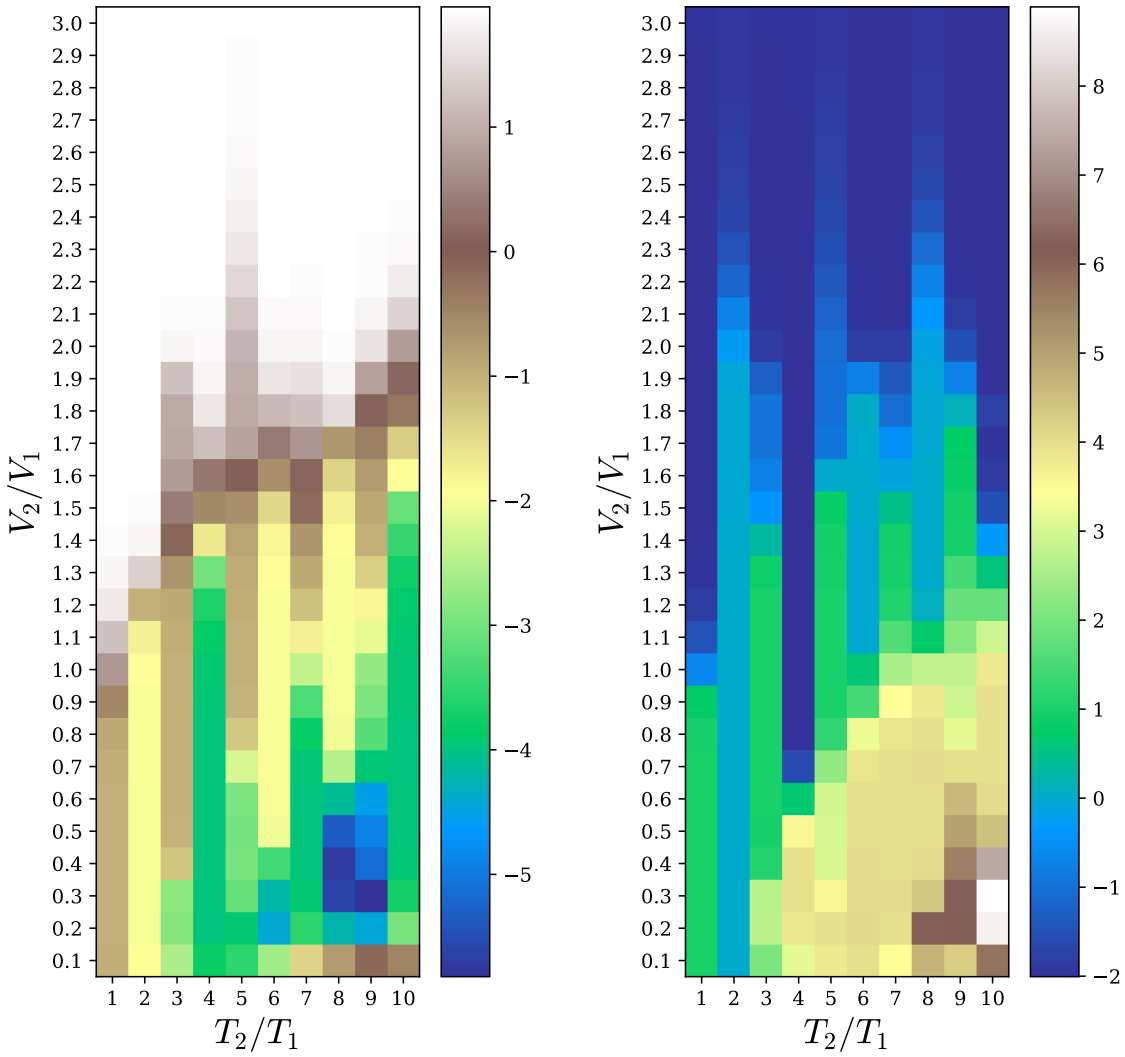

Figure 6.9: Topological phase diagrams of the Generalised Aubry-André model with $J = 0$. The topological index of the system is indicated by colour. We vary the ratio of the amplitudes V_2/V_1 along with the ratio of the time periods T_2/T_1. (a) The topological phase diagram for GAA model with the bottom band populated. (b) The topological phase diagram for GAA model with the bottom two bands populated.

Figure 6.9a shows the topological phase diagram for the GAA model with the bottom band populated. We see that for values of V_2/V_1 greater than 2.4 the change in $\mathcal{M}_1$ over a full time period is equal to 2 for any T_2/T_1 and therefore the topological index of the system is 2 when V_2/V_1 is greater than 2.4. It can also be seen that the topological index of the system for values of V_2/V_1 lower than this is highly dependent on the value of T_2/T_1. These topological indices also seem to be stable in places given that they persist for large ranges of V_2/V_1. For example, when $T_2/T_1 = 6$ and V_2/V_1 is varied one can see a clear phase transition between a system with a topological index of -2 to a system with a topological index of 2. More complex phase transitions happen for $T_2/T_1 = 3$ and $T_2/T_1 = 5$ where the system undergoes two phase transitions and three phase transitions respectively. For the case where $T_2/T_1 = 3$ the system has a topological index of -1 when V_2/V_1 takes on values between 0.5 and 1.2; a topological index of 1 when V_2/V_1 is between 1.6 and 1.9; and a topological index of 2 when V_2/V_1 is greater than 2.1. For the case where $T_2/T_1 = 5$ the topological index of the system is -3 when V_2/V_1 takes on values between 0.3 and 0.6; a topological index of -1 when V_2/V_1 is between 0.9 and 1.4; a topological index of 1 when V_2/V_1 is between 1.7 and 1.9; and a topological index of 2 when V_2/V_1 is greater than 2.5.

Figure 6.9b shows the topological phase diagram for the GAA model with two bands populated and $J = 0$. Like fig. 6.9a, this phase diagram also contains more phase transitions than the $J = 1$ case. What is unique about this case though, is that we have phase transitions between topologically trivial phases and topologically non-trivial phases; this behaviour is not seen when only the bottom band of the system is populated. A specific example of this behaviour can be seen when $T_2/T_1 = 2$. In this case the topological index of the system is 0 for values of V_2/V_1 less than 1.8 and the topological index of the system is -2 for values of V_2/V_1 greater than 2.7. Another very interesting case is when $T_2/T_1 = 6$. In this case we see that for V_2/V_1 between 0.2 and 0.7 the topological index of the system is 4; for V_2/V_1 between 1.1 and 1.8 the topological index is 0; and for V_2/V_1 greater than 2.1 the topological index of the system is -2. Both these cases could prove very useful when using topological properties of a system to control the flow of particles or light.

At this point it is useful to further investigate the phase transitions seen for specific values of T_2/T_1 from both fig. 6.9a and fig. 6.9b. We will first analyse the topological phase transitions seen when V_2/V_1 is varied and $T_2/T_1 = 5$ with only the bottom band of the GAA model populated. This analysis is shown in Figure 6.10. The top graph in this figure shows how the change in $\mathcal{M}_1$ over a full time period varies for increasing values of V_2/V_1. From this graph we see that when V_2/V_1 lies between 0.3 and 0.65 the topological index of the system is -3. As V_2/V_1 is increased above 0.65 the system goes through a topological phase transition in which the band gap closes and then reopens. This can be seen from the middle graph which plots the size of the energy gap between the first and second energy bands of the GAA model. When the gap reopens the topological index of this gap has a value of -1.

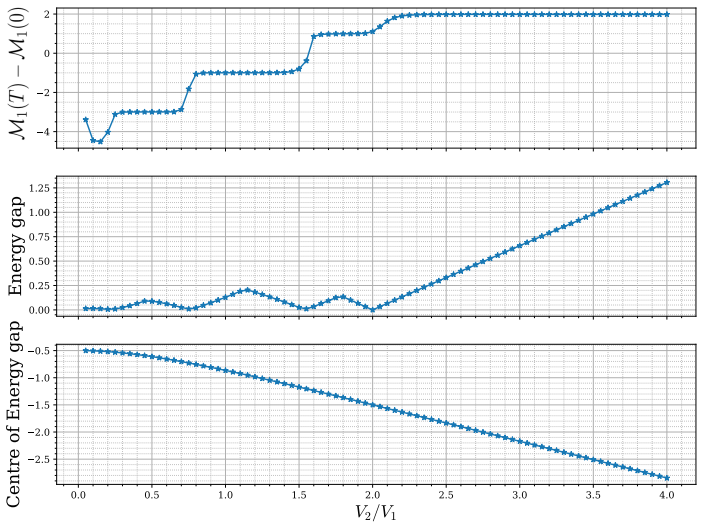

Figure 6.10: Analysis of the phase transitions when the bottom band of the GAA model is populated with $J = 0$ and $T_2/T_1 = 5$. The top graph displays the change in $\mathcal{M}_1$ over a full time period for varying values of V_2/V_1. The middle graph shows the size of the energy gap above the bottom band of the system. The bottom graph plots the energy at the centre of this band gap.

Two other topological phase transitions can be seen where the topological index changes from -1 to 1 and then from 1 to 2 for increasing values of V_2/V_1 where each time the band gap closes. The bottom graph plots the energy value at the centre of the band gap. This graph shows that for increasing values of V_2/V_1 the energy gap shifts downwards. This does not matter for systems with a fixed filling factor but would be important for systems that populate all states below a set Fermi-energy.

Next, we analyse the topological phase transition seen when $T_2/T_1 = 2$ with the bottom two bands populated; this analysis is depicted in fig. 6.11. From this figure we see that when V_2/V_1 is less than 1.9 the system has a topological index of 0 and therefore does not display topological pumping. We also see that at $V_2/V_1 = 2$ the energy gap closes and the system goes through a topological phase transition. When V_2/V_1 is greater than 2.1 the band gap has reopened and the change in $\mathcal{M}_1$ is -2 indicating that the topological index of the system is now -2. Again, we also see that the centre of the band gap gradually changes, increasing in energy value as V_2/V_1 is is increased.

Lastly, we analyse the case where $T_2/T_1 = 6$ and the bottom 2 bands of the GAA model are populated. This analysis is depicted in fig. 6.12. This figure shows that the system has a topological index of 4 when V_2/V_1 lies between 0.2 and 0.7. At the point 0.9 the band gap closes and the system undergoes a topological phase transition. After this the band gap reopens and when $V_2/V_1 =$ lies between 1 and 1.9 the system has a topological index of 0 meaning it is topologically trivial in nature

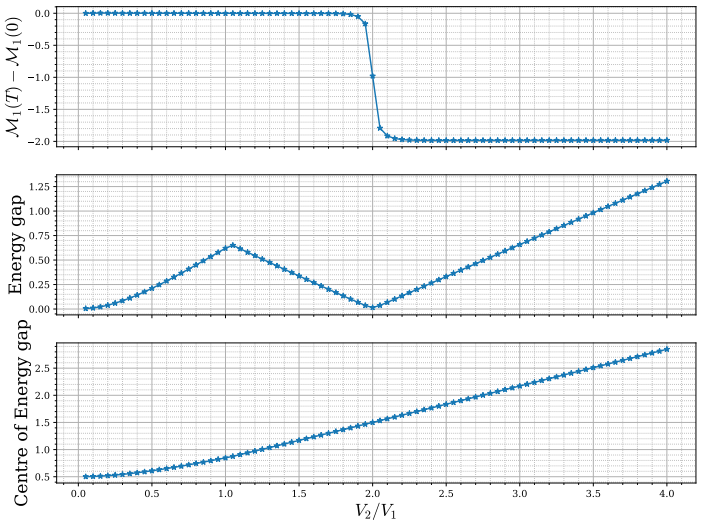

Figure 6.11: Analysis of the phase transition when the bottom two bands of the GAA model are populated with $J = 0$ and $T_2/T_1 = 2$. The top graph displays the change in $\mathcal{M}_1$ over a full time period for varying values of V_2/V_1. The middle graph shows the size of the energy gap above the bottom two bands of the system. The bottom graph plots the energy at the centre of this band gap.

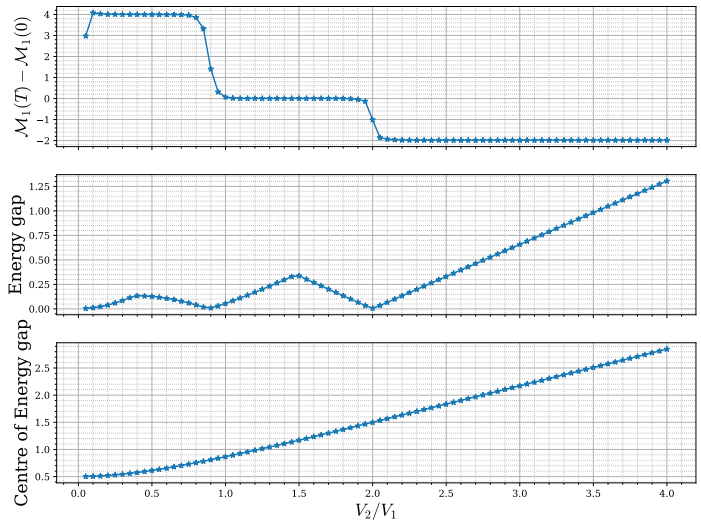

Figure 6.12: Analysis of the phase transition when the bottom two bands of the GAA model are populated with $J = 0$ and $T_2/T_1 = 6$. The top graph displays the change in $\mathcal{M}_1$ over a full time period for varying values of V_2/V_1. The middle graph shows the size of the energy gap above the bottom two bands of the system. The bottom graph plots the energy at the centre of this band gap.

and the system exhibits no pumping. At the point $V_2/V_1 = 2$ the band gap closes again and the system undergoes another topological phase transition. When the band gap reopens the topological index of the system is -2 and remains at this value for all values of V_2/V_1 greater than 2.1. The bottom graph again shows that the centre of the band gap increases in energy for increasing V_2/V_1.

In this section we have shown that the GAA model displays interesting and potentially useful topological phase transitions when the value J is set to zero so that only a cosine modulation determines the hopping term of the Hamiltonian. It was also shown that when the bottom 2 bands of the system are populated topological phase transitions exist between the topologically trivial case and the topologically non trivial case. The most interesting case was found to be when $T_2/T_1 = 6$ with the lowest two bands populated. In this case the system can possess a positive, a negative, or a trivial topological index which means that the quantized current flowing through the system can be pumped forwards or backwards or be stopped altogether. This high degree of current control could be very useful in engineering practices that require moving objects with a high degree of positional accuracy. This property may also be useful in the controlling of photons within optical systems.

7

Topological pumping in three dimensions

The advancement in experimental techniques to investigate four-dimensional topological physics, as well as the advancement in the understanding of topological structure in higher dimensions, has opened the door to the possibility of exploring topological pumping in three dimensional time-dependent systems. It is known that both 4D topological systems and 3D time-dependent topological systems are characterised by the second Chern number of the system [24, 31, 76]. However, unlike 1D topological pumping systems, it is not fully clear what is being pumped in the 3D case when there is no magnetic or electric field applied to the system.

The development of hybrid Wannier functions has also contributed to the understanding of topological pumping in three dimensions. However, due to their delocalization in two of the three spatial dimensions, this technique is not always useful when investigating inhomogeneous or non-Hermitian topological systems. As such, the development of a 3D real-space local topological marker, just like the 1D marker, would allow the investigation and characterisation of 3D time-dependent Hamiltonians that are inhomogeneous in nature. This local marker could also shed further light on what exactly is pumped in the 3D case when no magnetic or electric fields are present.

Like in the 1D case, throughout this chapter we will consider time-dependent Hamiltonians that do not break discrete translational invariance in the bulk. As such, the translationally invariant forms of the projectors and the adiabatic evolution operator can be used along with the definition of the position operators that label the unit cell of the system.

Within this chapter we start by reviewing previous relevant work and motivate the development of the 3D marker. We then develop the 3D marker in such a way that, in the bulk, its change over a pumping period gives the second Chern number of a system. With the 3D marker defined, we then introduce the Chern-Simons axion coupling and show that the 3D marker is directly proportional to the change in the Chern-Simons axion coupling over time. This relationship has parallels with the relationship previously found between the polarisation and the 1D marker. Finally, we support our analytical findings with numerical calculations and investigate when the agreement between the 3D marker and the second Chern number breaks down.

7.1 Extensive Chern-Simons axion coupling

We start this chapter by motivating the derivation of the 3D marker. We do this by showing that the extensive Chern-Simons axion coupling, θ_0, which has been previously used to demonstrate pumping in 3D topological models [26, 76], fails to describe the topological structure of finite decoupled Hamiltonians.

As we showed earlier, the projected position operators, $\hat{P}\hat{x}_i\hat{P}$, do not commute for topological systems and as a result the Wannier transform can only be carried out in one dimension. Hybrid Wannier functions do just this resulting in Wannier sheets for 3D systems rather than the normal Wannier centres for 1D systems. Hybrid Wannier functions have been used to explore topological pumping in 3D systems by using them to investigating the following expression under periodic boundary conditions in 2 directions and open boundary conditions in the third direction [76];

$$\theta_0 = -\frac{4\pi^2}{3i}\epsilon^{ijk}\mathrm{Tr}\big(\hat{P}\hat{x}_i\hat{P}\hat{x}_j\hat{P}\hat{x}_k\big), \tag{7.1}$$

where ϵ_{ijk} is the Levi-Civita symbol. It was found that, for this model, the change in θ_0 over a full time period was equal to the second Chern number. But interestingly, this expression is always zero for finite decoupled Hamiltonians even if the system has a non-zero second Chern number. We demonstrate this below.

It has been shown that for a Hamiltonian which decouples in the following way

$$\hat{H} = \hat{H}_a \otimes \mathbb{1} + \mathbb{1} \otimes \hat{H}_b \tag{7.2}$$

the second Chern number of this system is equal to the first Chern number of $\hat{H}_a$ multiplied by the first Chern number of $\hat{H}_b$ [27].

To show that θ_0 is always zero for these types of Hamiltonians we consider the following Hamiltonian

$$\hat{H} = \hat{H}_{xy} + \hat{H}_z \tag{7.3}$$

where the operators $\hat{x}$ and $\hat{y}$ act on the Hilbert space of $\hat{H}_{xy}$ and the operator $\hat{z}$ acts on the Hilbert space of $\hat{H}_z$. The eigenvectors of this Hamiltonian then take the form

$$|\psi_n\rangle = |\phi_l\rangle \otimes |\chi_m\rangle \tag{7.4}$$

with n labelling the bands of $\hat{H}$ and l and m labelling the corresponding occupied bands of $\hat{H}_{xy}$ and $\hat{H}_z$ respectively. We have suppressed the $\boldsymbol{k}$ dependence in the above equation for notational conciseness and will do so through out this section. The eigenvalues of this system obey

$$E = E_{xy} + E_z \tag{7.5}$$

where E is given by the eigenvalues of $\hat{H}$, E_{xy} is given by the eigenvalues of $\hat{H}_{xy}$ and E_z is given by the eigenvalues of $\hat{H}_z$. With this we can then define the projector $\hat{P}$ of the system as

$$\hat{P} = \sum_{l,m} a_{lm} |\phi_l\rangle \langle\phi_l| \otimes |\chi_m\rangle \langle\chi_m| . \tag{7.6}$$

The summation runs over all values of l and m and a_{lm} takes on values of 0 if the corresponding band labelled by n is unoccupied and 1 if the corresponding band labelled by n is occupied; one can determine a_{lm} by using eq. (7.5). Next, it can be shown using the cyclic properties of the trace that

$$\epsilon^{ijk}\mathrm{Tr}(\hat{P}\hat{x}_i\hat{P}\hat{x}_j\hat{P}\hat{x}_k) = 3\Big(\mathrm{Tr}(\hat{P}\hat{x}\hat{P}\hat{y}\hat{P}\hat{z}) - \mathrm{Tr}(\hat{P}\hat{y}\hat{P}\hat{x}\hat{P}\hat{z})\Big). \tag{7.7}$$

We now analyse $\mathrm{Tr}(\hat{P}\hat{x}\hat{P}\hat{y}\hat{P}\hat{z})$ using eq. (7.6) and find that

$$\begin{aligned}
\mathrm{Tr}\big(\hat{P}\hat{x}\hat{P}\hat{y}\hat{P}\hat{z}\big) &= \sum_{l,l',m} a_{lm}a_{l'm} \langle\phi_l| \hat{x} |\phi_{l'}\rangle \langle\phi_{l'}| \hat{y} |\phi_l\rangle \langle\chi_m| \hat{z} |\chi_m\rangle \\
&= \sum_{l,l',m} a_{lm}a_{l'm} \langle\phi_l| \hat{y} |\phi_{l'}\rangle \langle\phi_{l'}| \hat{x} |\phi_l\rangle \langle\chi_m| \hat{z} |\chi_m\rangle \\
&= \mathrm{Tr}\big(\hat{P}\hat{y}\hat{P}\hat{x}\hat{P}\hat{z}\big).
\end{aligned} \tag{7.8}$$

From this, it can be seen that $\epsilon^{ijk}\mathrm{Tr}(\hat{P}\hat{x}_i\hat{P}\hat{x}_j\hat{P}\hat{x}_k)$ is zero for any finite decoupled Hamiltonian at any

time t and therefore the change in eq. (7.1) over a time period is always zero for any finite decoupled Hamiltonian. However, as shown in [27], decoupled Hamiltonians can have non-zero topology. As such, we find that the change in θ_0 cannot describe the topology of finite decoupled Hamiltonians.

The fact that the change in θ_0 coupling does not correctly describe the topology of finite decoupled Hamiltonians, along with the benefits of a real-space local topological marker, then motivates the development of the 3D marker.

7.2 The 3D marker

With the motivation for the 3D marker established, we now move on to define the 3D marker. We start by defining the object $\mathcal{R}$, which is a natural extension of the 1D marker, and show that the change of this quantity over a time period is equal to the second Chern number of the system plus extra terms. With this we then define the 3D marker such that its change over a pumping period is equal to the second Chern number of the system.

To derive the 3D marker we start by defining $\mathcal{R}$ as

$$\mathcal{R} = -i\,\epsilon^{ijk}\mathrm{tr}_{\boldsymbol{x}}(\hat{\bar{P}}\hat{U}^\dagger\hat{x}_i\hat{U}\hat{\bar{P}}\hat{U}^\dagger\hat{x}_j\hat{U}\hat{\bar{P}}\hat{U}^\dagger\hat{x}_k\hat{U}\hat{\bar{P}}), \tag{7.9}$$

where $\hat{\bar{P}}$ is the projector at time $t = 0$. Neglecting the constant, the above equation is a viable extension of the 1D marker to three dimensions. To simplify notation slightly we define $\hat{X}_i \equiv \hat{P}\hat{x}_i\hat{P}$ and remind the reader that $\hat{P} = \hat{U}\hat{\bar{P}}\hat{U}^\dagger$. We can then rewrite $\mathcal{R}$ as

$$\mathcal{R} = -\frac{i}{2}\epsilon^{ijk}\mathrm{tr}_{\boldsymbol{x}}(\hat{U}^\dagger\hat{X}_i\hat{U}\hat{U}^\dagger[\hat{X}_j,\hat{X}_k]\hat{U}), \tag{7.10}$$

where the square brackets in the above equation denote the commutator. The commutator above can be written as

$$-i\big[\hat{X}_i,\hat{X}_j\big] = i\Big(\hat{P}\hat{x}_i\hat{Q}\hat{x}_j\hat{P} - \hat{P}\hat{x}_j\hat{Q}\hat{x}_i\hat{P}\Big) \tag{7.11}$$

where we have used $\hat{P} = \mathbb{1} - \hat{Q}$. If we then use the form of $\hat{P}\hat{x}_i\hat{Q}$ given in eq. (4.14), it can be shown that

$$-i\big[\hat{X}_i,\hat{X}_j\big] = \int d\boldsymbol{k}\,|\boldsymbol{k}\rangle\,\langle\boldsymbol{k}|\otimes i\,\hat{\mathcal{P}}\Big[\partial_i\hat{\mathcal{P}},\partial_j\hat{\mathcal{P}}\Big]\hat{\mathcal{P}}. \tag{7.12}$$

It is useful to define

$$\hat{F}_{ij} \equiv -i\big[\hat{X}_i,\hat{X}_j\big] \qquad \text{and} \qquad \hat{\mathcal{F}}_{ij} \equiv i\,\hat{\mathcal{P}}\Big[\partial_i\hat{\mathcal{P}},\partial_j\hat{\mathcal{P}}\Big]\hat{\mathcal{P}}, \tag{7.13}$$

where $\hat{\mathcal{F}}_{ij}$ is the translationally invariant part of $\hat{F}_{ij}$. With this notation

$$\mathcal{R} = \frac{1}{2}\epsilon_{ijk}\mathrm{tr}_{\boldsymbol{x}}\Big(\hat{U}^\dagger \hat{X}_i \hat{U}\hat{U}^\dagger \hat{F}_{jk}\hat{U}\Big). \tag{7.14}$$

Next, using $\hat{U}^\dagger \hat{X}_i \hat{U} = \hat{\tilde{P}}\hat{x}_i\hat{\tilde{P}} + \hat{A}_i$ which is found from using $\hat{P} = \hat{U}\hat{\tilde{P}}\hat{U}^\dagger$ in eq. (6.28), we find that

$$\mathcal{R} = \frac{\epsilon^{ijk}}{2}\Big(\mathrm{tr}_{\boldsymbol{x}}(\hat{\tilde{P}}\hat{x}_i\hat{\tilde{P}}\hat{U}^\dagger\hat{F}_{jk}\hat{U}) + \mathrm{tr}_{\boldsymbol{x}}(\hat{A}_i\hat{U}^\dagger\hat{F}_{jk}\hat{U})\Big). \tag{7.15}$$

We will now show that the first term in the brackets is time independent. To do this, we first analyse $\hat{\tilde{P}}\hat{x}_i\hat{\tilde{P}}$ to get

$$\hat{\tilde{P}}\hat{x}_i\hat{\tilde{P}} = -i\int_{BZ} d\boldsymbol{k}\, d\boldsymbol{k'}\, |\boldsymbol{k}\rangle\, \partial_{k_i'}\Big(\delta(\boldsymbol{k'}-\boldsymbol{k})\Big)\, \langle \boldsymbol{k'}| \otimes \hat{\tilde{\mathcal{P}}}_{\boldsymbol{k}}\hat{\tilde{\mathcal{P}}}_{\boldsymbol{k'}}, \tag{7.16}$$

where we have used $\langle \boldsymbol{k}|\, x_a\, |\boldsymbol{k'}\rangle = -i\partial_{k_i}\big(\delta(\boldsymbol{k'}-\boldsymbol{k})\big)$, which can be shown using the definition of $|\boldsymbol{k}\rangle$ given in eq. (2.5). If we then integrate by parts and again use the definition given in eq. (2.5) we get that

$$\hat{\tilde{P}}\hat{x}_i\hat{\tilde{P}} = x_i\int d\boldsymbol{k}\, |\boldsymbol{k}\rangle\, \langle \boldsymbol{k}| \otimes \hat{\tilde{\mathcal{P}}}_{\boldsymbol{k}} \;-\; i\int d\boldsymbol{k}\, |\boldsymbol{k}\rangle\, \langle \boldsymbol{k}| \otimes \hat{\tilde{\mathcal{P}}}_{\boldsymbol{k}}\Big(\partial_{k_i}\hat{\tilde{\mathcal{P}}}_{\boldsymbol{k}}\Big), \tag{7.17}$$

where x_i is the ith component of the vector labelling the unit cell position. From the definition of $\hat{F}_{jk}$ given in eq. (7.13), as well as the definition of $\hat{U}$ given in eq. (6.15), it can also be seen that

$$\hat{U}^\dagger\hat{F}_{jk}\hat{U} = \int d\boldsymbol{k}\, |\boldsymbol{k}\rangle\, \langle \boldsymbol{k}| \otimes \hat{\mathcal{U}}^\dagger\hat{\mathcal{F}}_{jk}\hat{\mathcal{U}}, \tag{7.18}$$

where above we have dropped the subscript $\boldsymbol{k}$ for notational convenience. Combining eq. (7.17) and eq. (7.18) it can be shown that

$$\hat{\tilde{P}}\hat{x}_i\hat{\tilde{P}}\hat{U}^\dagger\hat{F}_{jk}\hat{U} = x_i\int d\boldsymbol{k}\, |\boldsymbol{k}\rangle\, \langle \boldsymbol{k}| \otimes \hat{\tilde{\mathcal{P}}}\hat{\mathcal{U}}^\dagger\hat{\mathcal{F}}_{jk}\hat{\mathcal{U}} \;-\; i\int d\boldsymbol{k}\, |\boldsymbol{k}\rangle\, \langle \boldsymbol{k}| \otimes \hat{\tilde{\mathcal{P}}}(\partial_{k_i}\hat{\tilde{\mathcal{P}}})\hat{\mathcal{U}}^\dagger\hat{\mathcal{F}}_{jk}\hat{\mathcal{U}}. \tag{7.19}$$

If we then use $\mathcal{F}_{jk} = \hat{\mathcal{P}}\mathcal{F}_{jk}\hat{\mathcal{P}}$, as well as $\hat{\mathcal{U}}\hat{\mathcal{P}} = \hat{\tilde{\mathcal{P}}}\hat{\mathcal{U}}$, the second term in the above equation contains $\hat{\tilde{\mathcal{P}}}(\partial_i\hat{\tilde{\mathcal{P}}})\hat{\tilde{\mathcal{P}}}$ which we previously stated is equal to zero. As such, we get that

$$\hat{\tilde{P}}\hat{x}_i\hat{\tilde{P}}\hat{U}^\dagger\hat{F}_{jk}\hat{U} = x_i\int d\boldsymbol{k}\, |\boldsymbol{k}\rangle\, \langle \boldsymbol{k}| \otimes \hat{\mathcal{U}}^\dagger\hat{\mathcal{F}}_{jk}\hat{\mathcal{U}}. \tag{7.20}$$

From this, the first term in eq. (7.15) becomes

$$\mathrm{tr}_{\boldsymbol{x}}\big(\hat{\tilde{P}}\hat{x}_i\hat{\tilde{P}}\hat{U}^\dagger\hat{F}_{jk}\hat{U}\big) = x_i\int\frac{d\boldsymbol{k}}{V_{\mathrm{BZ}}}\mathrm{Tr}_\alpha\big(\hat{\mathcal{U}}^\dagger\hat{\mathcal{F}}_{jk}\hat{\mathcal{U}}\big) = x_i\int\frac{d\boldsymbol{k}}{V_{\mathrm{BZ}}}\mathrm{Tr}_\alpha\big(\hat{\mathcal{F}}_{jk}\big). \tag{7.21}$$

In the second equality above we used the fact that when the trace over internal degrees of freedom, Tr_α, contains only transitionally invariant operators it possesses the cyclical properties of the full trace. Using the definition of $\hat{\mathcal{F}}_{jk}$, it can be shown that $\mathrm{Tr}_\alpha\big(\hat{\mathcal{F}}_{jk}\big) = \mathrm{Tr}\big(\tilde{\boldsymbol{B}}_{jk}\big)$, where $\tilde{\boldsymbol{B}}_{jk} = \partial_j\tilde{\mathcal{A}}_k - \partial_k\tilde{\mathcal{A}}_j - i[\tilde{\mathcal{A}}_j, \tilde{\mathcal{A}}_k]$ is the matrix Berry curvature, $\tilde{\mathcal{A}}_j^{nm} = i\,\langle u_{\boldsymbol{k}n}|\partial_j\, u_{\boldsymbol{k}m}\rangle$ is the matrix Berry connection with n and m labelling the occupied bands and the trace over these objects is a trace over matrices. Using this, we get that

$$\mathrm{tr}_{\boldsymbol{x}}\big(\hat{\bar{P}}\hat{x}_i\hat{\bar{P}}\hat{U}^\dagger\hat{F}_{jk}\hat{U}\big) = x_i\int\frac{d\boldsymbol{k}}{V_{\mathrm{BZ}}}\mathrm{Tr}\big(\partial_j\tilde{\mathcal{A}}_k - \partial_k\tilde{\mathcal{A}}_j\big). \tag{7.22}$$

We can now analyse the time dependence of the above equation. Any time dependence in the above equation has to come from the trace seen as x_i labels the initial unit cell. As such, we will now analyse $\frac{d}{dt}\mathrm{Tr}\big(\partial_j\tilde{\mathcal{A}}_k - \partial_k\tilde{\mathcal{A}}_j\big)$. Performing integration by parts, it can be shown that

$$\begin{aligned}\frac{d}{dt}\mathrm{Tr}\big(\partial_j\tilde{\mathcal{A}}_k - \partial_k\tilde{\mathcal{A}}_j\big) = \partial_j\Big(\big\langle\tfrac{d}{dt}u_{\boldsymbol{k}n}\big|\partial_k u_{\boldsymbol{k}n}\big\rangle - \big\langle\partial_k u_{\boldsymbol{k}n}\big|\tfrac{d}{dt}u_{\boldsymbol{k}n}\big\rangle\Big)\\ - \partial_k\Big(\big\langle\tfrac{d}{dt}u_{\boldsymbol{k}n}\big|\partial_j u_{\boldsymbol{k}n}\big\rangle - \big\langle\partial_j u_{\boldsymbol{k}n}\big|\tfrac{d}{dt}u_{\boldsymbol{k}n}\big\rangle\Big).\end{aligned} \tag{7.23}$$

In the above equation each term is a total derivative with respect to a direction in $\boldsymbol{k}$-space and therefore if we integrate the above equation over the Brillouin zone we get zero due to the translational invariance of the system. With this we have show that the first term in eq. (7.15) is time independent.

Using this result we now see that when one takes the time derivative of $\mathcal{R}$ the first term disappears and we get

$$\frac{d}{dt}\mathcal{R} = \frac{\epsilon^{ijk}}{2}\mathrm{tr}_{\boldsymbol{x}}\Big(\Big(\frac{d}{dt}\hat{A}_i\Big)\hat{U}^\dagger\hat{F}_{jk}\hat{U} + \hat{A}_i\frac{d}{dt}\Big(\hat{U}^\dagger\hat{F}_{jk}\hat{U}\Big)\Big). \tag{7.24}$$

All the terms in local trace above can be written in a translationally invariant form and doing this we get that

$$\frac{d}{dt}\mathcal{R} = \frac{\epsilon^{ijk}}{2}\int\frac{d\boldsymbol{k}}{V_{\mathrm{BZ}}}\mathrm{Tr}_\alpha\Big(\Big(\frac{d}{dt}\hat{\mathcal{A}}_i\Big)\hat{\mathcal{U}}^\dagger\hat{\mathcal{F}}_{jk}\hat{\mathcal{U}} + \hat{\mathcal{A}}_i\frac{d}{dt}\Big(\hat{\mathcal{U}}^\dagger\hat{\mathcal{F}}_{jk}\hat{\mathcal{U}}\Big)\Big). \tag{7.25}$$

To analyse the above equation we first analyse $\frac{d}{dt}\hat{\mathcal{A}}_i$. Using eq. (6.19), it can be shown that

$$\begin{aligned}\frac{d}{dt}\hat{\mathcal{A}}_i &= i\frac{d}{dt}\Big(\hat{\bar{\mathcal{P}}}\hat{\mathcal{U}}^\dagger(\partial_i\hat{\mathcal{U}})\hat{\bar{\mathcal{P}}}\Big)\\ &= i\hat{\bar{\mathcal{P}}}\big(\frac{d}{dt}\hat{\mathcal{U}}^\dagger\big)(\partial_i\hat{\mathcal{U}})\hat{\bar{\mathcal{P}}} + i\hat{\bar{\mathcal{P}}}\hat{\mathcal{U}}^\dagger\partial_i\big(\frac{d}{dt}\hat{\mathcal{U}}\big)\hat{\bar{\mathcal{P}}}.\end{aligned} \tag{7.26}$$

If we use $i\frac{d}{dt}\hat{\mathcal{U}} = \mathfrak{h}\hat{\mathcal{U}}$, which can be shown by combining eq. (6.8) with eq. (6.14) and eq. (6.15), and its Hermitian conjugate in the equation above we find that

$$\frac{d}{dt}\hat{\mathcal{A}}_i = i\,\hat{\mathcal{U}}^\dagger\hat{\mathcal{P}}\partial_i\Big([\dot{\hat{\mathcal{P}}},\hat{\mathcal{P}}]\Big)\hat{\mathcal{P}}\hat{\mathcal{U}} = i\,\hat{\mathcal{U}}^\dagger\hat{\mathcal{P}}[\dot{\hat{\mathcal{P}}},\partial_i\hat{\mathcal{P}}]\hat{\mathcal{P}}\hat{\mathcal{U}} = \hat{\mathcal{U}}^\dagger\,\hat{\mathcal{F}}_{ti}\,\hat{\mathcal{U}}, \tag{7.27}$$

where in the last equality we have defined $\hat{\mathcal{F}}_{ti} \equiv i\,\hat{\mathcal{P}}[\frac{d}{dt}\hat{\mathcal{P}},\partial_i\hat{\mathcal{P}}]\hat{\mathcal{P}}$. Using the above equation in the first

term of eq. (7.25) we see that

$$\frac{\epsilon^{ijk}}{2}\int\frac{d\boldsymbol{k}}{V_{\mathrm{BZ}}}\mathrm{Tr}_\alpha\Big(\frac{d}{dt}(\hat{\mathcal{A}}_i)\hat{\mathcal{U}}^\dagger\hat{\mathcal{F}}_{jk}\hat{\mathcal{U}}\Big)=\frac{V_c}{16\pi^3}\epsilon^{ijk}\int d\boldsymbol{k}\mathrm{Tr}_\alpha\big(\hat{\mathcal{F}}_{ti}\hat{\mathcal{F}}_{jk}\big). \tag{7.28}$$

The above equation is proportional to the second Chern number, given in eq. (2.45), when integrated over a full time period, T [24].

With this, we next move on to evaluate the second term in eq. (7.25). To do this we use the identity

$$\hat{\mathcal{U}}^\dagger\hat{\mathcal{F}}_{ij}\hat{\mathcal{U}}=\hat{\tilde{\mathcal{P}}}(\partial_i\hat{\mathcal{A}}_j-\partial_j\hat{\mathcal{A}}_i-i[\hat{\mathcal{A}}_i,\hat{\mathcal{A}}_j])\hat{\tilde{\mathcal{P}}}+\hat{\tilde{\mathcal{F}}}_{ij} \tag{7.29}$$

which is proved in appendix A. Above, the last term is just $\hat{\mathcal{F}}_{ij}$ evaluated at time $t=0$ and is therefore defined as $\hat{\tilde{\mathcal{F}}}_{ij}\equiv i\,\hat{\tilde{\mathcal{P}}}[\partial_i\hat{\tilde{\mathcal{P}}},\partial_j\hat{\tilde{\mathcal{P}}}]\hat{\tilde{\mathcal{P}}}$. Using the above identity in the second term of eq. (7.25) we get

$$\frac{\epsilon^{ijk}}{2}\int\frac{d\boldsymbol{k}}{V_{\mathrm{BZ}}}\mathrm{Tr}_\alpha\Big(\hat{\mathcal{A}}_i\frac{d}{dt}(\hat{\mathcal{U}}^\dagger\hat{\mathcal{F}}_{jk}\hat{\mathcal{U}})\Big)=\frac{\epsilon^{ijk}}{2}\int\frac{d\boldsymbol{k}}{V_{\mathrm{BZ}}}\mathrm{Tr}_\alpha\Big(\hat{\mathcal{A}}_i\partial_j\partial_t\hat{\mathcal{A}}_k-\hat{\mathcal{A}}_i\partial_k\partial_t\hat{\mathcal{A}}_j-i\hat{\mathcal{A}}_i\partial_t[\hat{\mathcal{A}}_j,\hat{\mathcal{A}}_k]\Big), \tag{7.30}$$

where above we used $\hat{\tilde{\mathcal{P}}}\hat{\mathcal{A}}_i=\hat{\mathcal{A}}_i$. If we then perform integration by parts on the first two terms, noticing that the total derivatives are zero due to translational invariance, and use the cyclic properties of Tr_α we find that

$$\frac{\epsilon^{ijk}}{2}\int\frac{d\boldsymbol{k}}{V_{\mathrm{BZ}}}\mathrm{Tr}_\alpha\Big(\hat{\mathcal{A}}_i\frac{d}{dt}(\hat{\mathcal{U}}^\dagger\hat{\mathcal{F}}_{jk}\hat{\mathcal{U}})\Big)=\frac{\epsilon^{ijk}}{2}\int\frac{d\boldsymbol{k}}{V_{\mathrm{BZ}}}\mathrm{Tr}_\alpha\Big((\partial_t\hat{\mathcal{A}}_i)(\partial_j\hat{\mathcal{A}}_k)-(\partial_t\hat{\mathcal{A}}_i)(\partial_k\hat{\mathcal{A}}_j)-i\hat{\mathcal{A}}_i\partial_t[\hat{\mathcal{A}}_j,\hat{\mathcal{A}}_k]\Big). \tag{7.31}$$

Due to the fact that $\partial_t\hat{\mathcal{A}}_i=\hat{\tilde{\mathcal{P}}}(\partial_t\hat{\mathcal{A}}_i)\hat{\tilde{\mathcal{P}}}$, we can use eq. (7.29) along with eq. (7.27) to rewrite the first two terms in the above equation and get

$$\frac{\epsilon^{ijk}}{2}\int\frac{d\boldsymbol{k}}{V_{\mathrm{BZ}}}\mathrm{Tr}_\alpha\Big(\hat{\mathcal{A}}_i\frac{d}{dt}(\hat{\mathcal{U}}^\dagger\hat{\mathcal{F}}_{jk}\hat{\mathcal{U}})\Big)=\frac{\epsilon^{ijk}}{2}\int\frac{d\boldsymbol{k}}{V_{\mathrm{BZ}}}\mathrm{Tr}_\alpha\Big(\hat{\mathcal{F}}_{ti}\hat{\mathcal{F}}_{jk}-(\partial_t\hat{\mathcal{A}}_i)\hat{\tilde{\mathcal{F}}}_{jk}-\frac{2i}{3}\partial_t(\hat{\mathcal{A}}_i\hat{\mathcal{A}}_j\hat{\mathcal{A}}_k)\Big). \tag{7.32}$$

In the above equation we used the properties of the Levi-Civita symbol and the cyclic property of the trace to obtain the last term. The last two terms can be written as total derivatives in time and will therefore disappear when integrated over the full time period T. As well as this, the first term is proportional to the second Chern number of the system. If we now substitute eq. (7.28) and eq. (7.32) into eq. (7.25) we find that

$$\frac{d}{dt}\mathcal{R}=\frac{V_c}{8\pi^3}\epsilon^{ijk}\int d\boldsymbol{k}\mathrm{Tr}_\alpha\big(\hat{\mathcal{F}}_{ti}\hat{\mathcal{F}}_{jk}\big)-\frac{V_c}{16\pi^3}\epsilon^{ijk}\int d\boldsymbol{k}\frac{d}{dt}\mathrm{Tr}_\alpha\Big(\hat{\mathcal{A}}_i\hat{\tilde{\mathcal{F}}}_{jk}+\frac{2i}{3}\hat{\mathcal{A}}_i\hat{\mathcal{A}}_j\hat{\mathcal{A}}_k\Big). \tag{7.33}$$

This equation shows that, with the right prefactor, the time derivative of $\mathcal{R}$ contains a term that is

related to the second Chern number of the system plus an extra term. With this, we then define $\mathcal{R}'$ as

$$\mathcal{R}' = \mathcal{R} + \frac{\epsilon^{ijk}}{2}\mathrm{tr}_{\boldsymbol{x}}\Big(\hat{A}_i\hat{\tilde{F}}_{jk} + \frac{2i}{3}\hat{A}_i\hat{A}_j\hat{A}_k\Big) \tag{7.34}$$

so that the time derivative of $\mathcal{R}'$ contains just the term that is related to the second Chern number. From this we choose to define the 3D marker as

$$\mathcal{M}_3(\boldsymbol{x}) = \frac{\pi}{2V_c}\epsilon^{ijk}\,\mathrm{tr}_{\boldsymbol{x}}\Big(\hat{A}_i\hat{U}^\dagger\hat{F}_{jk}\hat{U} + \hat{A}_i\hat{\tilde{F}}_{jk} + \frac{2i}{3}\hat{A}_i\hat{A}_j\hat{A}_k\Big). \tag{7.35}$$

With this definition, when $\mathcal{M}_3(\boldsymbol{x})$ is analysed within the bulk of the system, we have that

$$\begin{aligned}\int_0^T dt\frac{d}{dt}\mathcal{M}_3(\boldsymbol{x}) &= \frac{1}{8\pi^2}\epsilon^{ijk}\int_0^T dt\int d\boldsymbol{k}\;\mathrm{Tr}_\alpha\big(\hat{\mathcal{F}}_{ti}\hat{\mathcal{F}}_{jk}\big)\\ &= \frac{1}{32\pi^2}\epsilon^{\mu\nu\sigma\rho}\int_0^T dt\int d\boldsymbol{k}\;\mathrm{Tr}_\alpha\big(\hat{\mathcal{F}}_{\mu\nu}\hat{\mathcal{F}}_{\sigma\rho}\big) = C_2\end{aligned} \tag{7.36}$$

where C_2 is the second Chern number and Greek indices are summed over both space and time components. In arriving at the last equality the cyclic property of the trace, as well as the anti-symmetry of $\hat{F}_{ij}$, was used. We are using a convention such that $\epsilon_{t\,k_x\,k_y\,k_z} = -\epsilon_{k_x\,k_y\,k_z\,t} = 1$. We have thus shown that the change in the 3D marker, defined in eq. (7.35), over a full time period gives the second Chern number of a 3D time-dependent system.

7.3 Relation between the 3D marker and Axion coupling

In the previous section we showed that the change in the 3D marker over a full time period gives the second Chern number. This then suggests that it is closely connected to the Chern-Simons axion coupling which is given by

$$\theta_{\mathrm{CS}} = \frac{1}{4\pi}\int_{\mathrm{BZ}} d\boldsymbol{k}\,\epsilon^{ijk}\,\mathrm{Tr}\Big(\tilde{\mathcal{A}}_i\partial_j\tilde{\mathcal{A}}_k - \frac{2i}{3}\tilde{\mathcal{A}}_i\tilde{\mathcal{A}}_j\tilde{\mathcal{A}}_k\Big). \tag{7.37}$$

When comparing the Chern-Simons axion coupling to the 3D marker it is interesting to point out that the 3D marker is constructed solely from the projector that projects into the occupied states of the system. As a result, the 3D marker is gauge invariant due to the projector being gauge invariant. On the contrary, it has been shown that the Chern-Simons axion coupling, which is the integrated Chern-Simons three-form, is only gauge invariant modulo 2π [77].

As well as this, to evaluate the axion coupling one has to be able to describe the states $|u_{\boldsymbol{k}n}\rangle$ as a smooth function of $\boldsymbol{k}$ across the entire Brillouin zone. It is generally assumed that as long as all

the first Chern numbers of the system are zero then there are no topological obstructions and one can evaluate the axion coupling. For a more in depth discussion of these types of subtleties see [78]. Therefore, to allow us to compare the 3D marker to the Chern-Simons axion coupling, we will assume for this section that the states $|u_{\boldsymbol{k}n}\rangle$ can be described as a smooth function of $\boldsymbol{k}$ across the Brillouin zone so eq. (7.37) can be evaluated; note, however, that the 3D marker does not require this condition.

When evaluated deep within the bulk, the 3D marker takes the form

$$\mathcal{M}_3 = \frac{\epsilon^{ijk}}{16\pi^2}\int_{\mathrm{BZ}} d\boldsymbol{k}\ \mathrm{Tr}_\alpha\Big(\hat{\mathcal{A}}_i\hat{\mathcal{U}}^\dagger\hat{\mathcal{F}}_{jk}\hat{\mathcal{U}} + \hat{\mathcal{A}}_i\hat{\tilde{\mathcal{F}}}_{jk} + \frac{2i}{3}\hat{\mathcal{A}}_i\hat{\mathcal{A}}_j\hat{\mathcal{A}}_k\Big). \tag{7.38}$$

To connect this to the axion coupling we will use the relation between $\hat{\mathcal{A}}_i$ and $\tilde{\mathcal{A}}_i$ given in eq. (6.20), which we restate here for convenience;

$$\hat{\mathcal{A}}_i = \sum_{nm}^{\mathrm{occ}} |u_{\boldsymbol{k}n}(0)\rangle\,\langle u_{\boldsymbol{k}m}(0)|\,\Big(\tilde{\mathcal{A}}_i^{nm}(t) - \tilde{\mathcal{A}}_i^{nm}(0)\Big). \tag{7.39}$$

A similar equation can be shown for $\hat{\mathcal{F}}_{ij}$ giving

$$\hat{\mathcal{F}}_{ij} = \sum_{nm}^{\mathrm{occ}} |u_{\boldsymbol{k}n}(t)\rangle\ \tilde{\boldsymbol{B}}_{ij}^{nm}(t)\ \langle u_{\boldsymbol{k}m}(t)|\ , \tag{7.40}$$

where $\tilde{\boldsymbol{B}}_{jk} = \partial_j\tilde{\mathcal{A}}_k - \partial_k\tilde{\mathcal{A}}_j - i[\tilde{\mathcal{A}}_j, \tilde{\mathcal{A}}_k]$ is the matrix Berry curvature. With these equations it can be shown that

$$\begin{aligned}\mathcal{M}_3 = \frac{\epsilon^{ijk}}{16\pi^2}\int_{\mathrm{BZ}} d\boldsymbol{k}\ \mathrm{Tr}\Big(&\Big(\tilde{\mathcal{A}}_i(t) - \tilde{\mathcal{A}}_i(0)\Big)\Big(\tilde{\boldsymbol{B}}_{jk}(t) + \tilde{\boldsymbol{B}}_{jk}(0)\Big)\\ &+ \frac{2i}{3}\Big(\tilde{\mathcal{A}}_i(t) - \tilde{\mathcal{A}}_i(0)\Big)\Big(\tilde{\mathcal{A}}_j(t) - \tilde{\mathcal{A}}_j(0)\Big)\Big(\tilde{\mathcal{A}}_k(t) - \tilde{\mathcal{A}}_k(0)\Big)\Big)\end{aligned} \tag{7.41}$$

where the trace is a trace over matrices. Expanding out the second line in the above equation, we get that

$$\begin{aligned}\mathcal{M}_3 = \frac{\epsilon^{ijk}}{16\pi^2}\int_{\mathrm{BZ}} d\boldsymbol{k}\ \mathrm{Tr}\Big(&\big(\tilde{\mathcal{A}}_i(t) - \tilde{\mathcal{A}}_i(0)\big)\big(\tilde{\boldsymbol{B}}_{jk}(t) + \tilde{\boldsymbol{B}}_{jk}(0)\big)\\ &+ \frac{2i}{3}\Big(\tilde{\mathcal{A}}_i(t)\tilde{\mathcal{A}}_j(t)\tilde{\mathcal{A}}_k(t) - \tilde{\mathcal{A}}_i(0)\tilde{\mathcal{A}}_j(0)\tilde{\mathcal{A}}_k(0)\Big)\\ &+ i\tilde{\mathcal{A}}_i(t)\big[\tilde{\mathcal{A}}_j(0), \tilde{\mathcal{A}}_k(0)\big] - i\tilde{\mathcal{A}}_i(0)\big[\tilde{\mathcal{A}}_j(t), \tilde{\mathcal{A}}_k(t)\big].\end{aligned} \tag{7.42}$$

If we then write out the Berry curvature terms explicitly we find that

$$\begin{aligned}\mathcal{M}_3 = \frac{\epsilon^{ijk}}{8\pi^2}\int_{\mathrm{BZ}} d\boldsymbol{k}\mathrm{Tr}\Big(&\tilde{\mathcal{A}}_i(t)\partial_j\tilde{\mathcal{A}}_k(t) - \tilde{\mathcal{A}}_i(0)\partial_j\tilde{\mathcal{A}}_k(0) + \partial_i\Big(\tilde{\mathcal{A}}_j(0)\tilde{\mathcal{A}}_k(t)\Big)\\ &- \frac{2i}{3}\Big(\tilde{\mathcal{A}}_i(t)\tilde{\mathcal{A}}_j(t)\tilde{\mathcal{A}}_k(t) - \tilde{\mathcal{A}}_i(0)\tilde{\mathcal{A}}_j(0)\tilde{\mathcal{A}}_k(0)\Big).\end{aligned} \tag{7.43}$$

Because we are analysing the system deep within the bulk we can assume translational invariance and therefore the total derivative term disappears. If we then compare the above equation to eq. (7.37) it can be shown that

$$\mathcal{M}_3 = \frac{1}{2\pi}\big(\theta_{\mathrm{CS}}(t) - \theta_{\mathrm{CS}}(0)\big). \tag{7.44}$$

This equation shows that the 3D marker deep within the bulk of the system at time t corresponds to the change in the integral of the Chern-Simons three form over time. This then explains why the Chern-Simons axion coupling has a 2π ambiguity but the 3D marker does not. One thing to note, however, is that the 3D marker is both gauge invariant and also does not require translational invariance to be evaluated; as such, it could be viewed as a more fundamental quantity. This relation is very similar to the change in the 1D marker over time being equal to the change in polarisation over time.

7.4 Numerical investigation of the 3D marker

In the previous section we showed analytically that the 3D marker is related to the change in the integral of Chern-Simons three form over time and that its change over a full time period gives the second Chern number of the system. In this section we confirm this relation numerically. Specifically, we will use the 3D marker to analyse the topological structure of the decoupled Hamiltonian, $\hat{H}_{3D}$, given in eq. (3.7), showing that it correctly predicts the second Chern number of this system. Note however that the 3D marker, when evaluated in the bulk of a system, should correctly predict the topological structure of any type of system as long as it obeys adiabatic time evolution.

It was shown in Figure 3.2 that the bottom band of $\hat{H}_{3D}$ is gapped for $k_z a_z = \pi/3$ and $\phi(t) = \pi/2$ and stated that this gap remains open for all values of $k_z a_z$ and $\phi(t)$. As such, we will analyse the bottom band of $\hat{H}_{3D}$ using the 3D marker. It was also stated that the second Chern number of a decoupled Hamiltonian is given by the product of first Chern numbers of the reduced Hamiltonians [27]. To confirm this we recall from eq. (7.4) that the eigenvectors of a decoupled Hamiltonian are separable and, from eq. (7.6), that the projector for a decoupled Hamiltonian is given by

$$\hat{P} = \sum_{l,m} a_{lm} \left|\phi_l\right\rangle \left\langle\phi_l\right| \otimes \left|\chi_m\right\rangle \left\langle\chi_m\right|, \tag{7.45}$$

where $|\phi_l\rangle$ and $|\chi_m\rangle$ are the eigenvectors of $\hat{H}_{HH}$ and $\hat{H}_{AA}$ respectively and l and m label the occupied bands of these Hamiltonians. With this, it can be seen that if only the bottom band is populated then the summation above disappears and the projector is also separable. If we let $\hat{P}'$ project into the lowest band of $\hat{H}_{HH}$ and let $\hat{P}''$ project into the lowest band of $\hat{H}_{AA}$ we get that the projector $\hat{P}$,

which projects into the lowest band of $\hat{H}_{3D}$, takes the form $\hat{P} = \hat{P}' \otimes \hat{P}''$. With the separability of the projector, along with the identity $\hat{P}(\partial_i \hat{P})\hat{P} = 0$, it can be shown that

$$\epsilon_{ijk}\hat{\mathcal{F}}_{ti}\hat{\mathcal{F}}_{jk} = 2\hat{\mathcal{F}}'_{k_x k_y} \otimes \hat{\mathcal{F}}''_{tk_z}. \tag{7.46}$$

Above, $\hat{\mathcal{F}}_{ij}$, $\hat{\mathcal{F}}'_{ij}$ and $\hat{\mathcal{F}}''_{ij}$ are constructed from $\hat{P}$, $\hat{P}'$ and $\hat{P}''$ respectively. Using this it can then be seen that the second Chern number of $\hat{H}_{3D}$ becomes

$$C_2 = \frac{1}{8\pi^2}\epsilon^{ijk}\int d\boldsymbol{k}\mathrm{Tr}\Big(\hat{\mathcal{F}}_{ti}\hat{\mathcal{F}}_{jk}\Big) = \frac{1}{4\pi^2}\int d\boldsymbol{k}\mathrm{Tr}\Big(\hat{\mathcal{F}}'_{k_x k_y}\Big)\mathrm{Tr}\Big(\hat{\mathcal{F}}''_{tk_z}\Big) = C'_1\, C''_1, \tag{7.47}$$

where C'_1 and C''_1 are the first Chern numbers of $\hat{H}_{HH}$ and $\hat{H}_{AA}$ respectively. We also used $\mathrm{Tr}(\hat{A}\otimes\hat{B}) = \mathrm{Tr}(\hat{A})\,\mathrm{Tr}(\hat{B})$ to get the second equality.

It was shown earlier that the first Chern number of the bottom band of $\hat{H}_{AA}$ is 1 and, due to the relation between $\hat{H}_{HH}$ and $\hat{H}_{AA}$, the first Chern number of the bottom band of $\hat{H}_{HH}$ is also 1. From this, the bottom band of $\hat{H}_{3D}$ has a second Chern number of 1 and we therefore expect $\mathcal{M}_3$ to change by 1 over a full time period.

Figure 7.1 shows the time evolution of the 3D marker, $\mathcal{M}_3$, deep within the bulk for a finite system with open boundary conditions. From this we see that the 3D marker does indeed change by 1 over

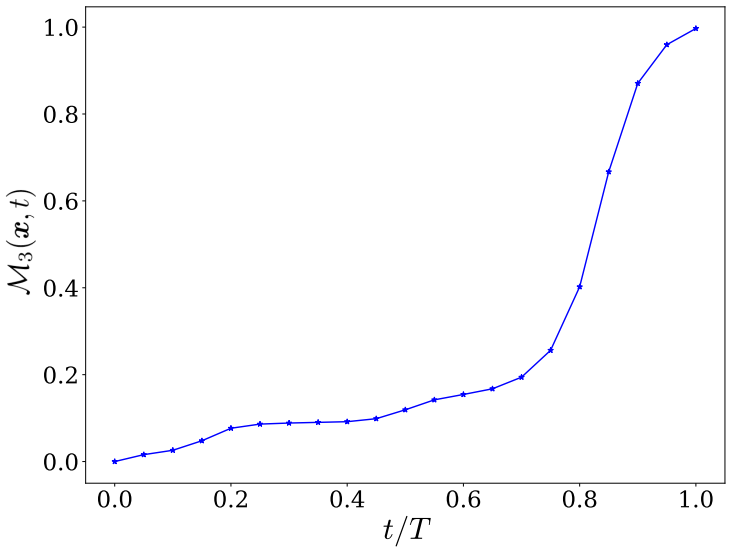

Figure 7.1: $\mathcal{M}_3(\boldsymbol{x}, t)$ as a function of time for a unit cell $\boldsymbol{x}$ in the bulk. The local trace was taken over the central unit cell for a finite system which extended by 10 unit cells in each direction and each unit cell contained 9 lattice sites. The parameters of the system were set to those in Figure 3.2.

a full time period which confirms our expectations. One may also notice that Figure 7.1 is similar to Figure 6.2. This is a result of $\hat{H}_{3D}$ being a decoupled Hamiltonian constructed from $\hat{H}_{AA}$ and another time independent 2D Hamiltonian. As such, all the time dependence of our 3D model comes from $\hat{H}_{AA}$ which results in the profile of Figure 7.1 being the same as that of Figure 6.2.

Similar to the 1D marker, the agreement between the 3D marker and the second Chern number fails when the local trace is taken over a unit cell which is close to the boundary of the system. This results from the fact that near the boundary of the system translational invariance can no longer be assumed and thus the equivalence between the 3D marker and the second Chern number deteriorates.

To investigate this break down in agreement further we calculate the 3D marker for $\hat{H}_{3D}$ (with the parameters given in Figure 3.2) in the central unit cell of the system for varying system size N^3, where N is the number of unit cells along each axis. Figure 7.2 shows that as N is increased the value of $\mathcal{M}_3$ increases and for $N = 9$ and $N = 10$ the 3D marker is 1. It was shown earlier that for $\hat{H}_{AA}$ (with the same parameters set in $\hat{H}_{3D}$) the 1D marker also converged to 1 at a system size of $N = 9$. This is not a coincidence but is due to how $\hat{H}_{3D}$ is constructed. Because of the decoupled nature of $\hat{H}_{3D}$, in

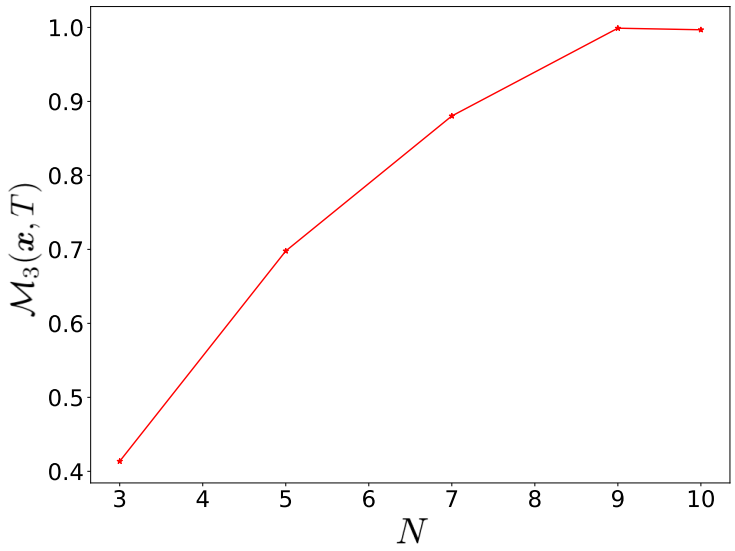

Figure 7.2: The change in $\mathcal{M}_3(\boldsymbol{x}, T)$ over a full time period for varying systems sizes, N^3, for the lowest band of $\hat{H}_{3D}$. The parameters of the system were set to the same values as in Figure 3.2. The local trace was taken over the centre most unit cell of the system and N represents the number of unit cells along each axis of the system.

the bulk of the system $\mathcal{M}_3$ becomes

$$\mathcal{M}_3 = \frac{1}{4\pi^2}\int_{\mathrm{BZ}} d\boldsymbol{k}\mathrm{Tr}\Big(\hat{\mathcal{A}}'_{k_z}\Big)\,\mathrm{Tr}\Big(\hat{\tilde{\mathcal{F}}}''_{k_x k_y}\Big) = \Big(\mathcal{M}'_1(t) - \mathcal{M}'_1(0)\Big)\mathcal{M}''_2. \tag{7.48}$$

This then makes it clear that, for a decoupled 3D Hamiltonian, the convergence of $\mathcal{M}_3$ to an integer depends on the convergence of $\mathcal{M}_1$ and $\mathcal{M}_2$ for the reduced Hamiltonians.

It was shown in chapter 6 that when $\mathcal{M}_1$ is measured 5 unit cells from the edge of the system it accurately predicts the topological index of the system. It can also be shown that $\mathcal{M}_2$, calculated over the central unit cell of the system, converges to an integer for $\hat{H}_{HH}$ (with the same parameters set in $\hat{H}_{3D}$) when the system size is $N^2 \geq 9^2$. This in turn suggests that the edge state modes have a negligible effect on sites 5 unit cells or more from the surface of the system. We analyse this by plotting the probability density of an edge state mode for $\hat{H}_{HH}$ in Figure 7.3.

It is clear from fig. 7.3 that the probability density of the edge state mode rapidly decays in size from the edge of the system. Further analysis shows that this decay is exponential in nature and 5 unit cells in from the edges of the system the probability density of the edge state mode is of order 3×10^{-4}. This analysis was done for numerous system sizes and it was found that the probability density of the edge state mode was negligible 5 unit cells in from the edges of the system. It can be shown that all the edge state modes of $\hat{H}_{HH}$ have negligible amplitude 5 unit cells from the edge of the system just like the edge state mode depicted in Figure 7.3. This in turn corroborates the statement that $\mathcal{M}_2$, calculated in the central unit cell of the system, converges for $N^2 \geq 9^2$.

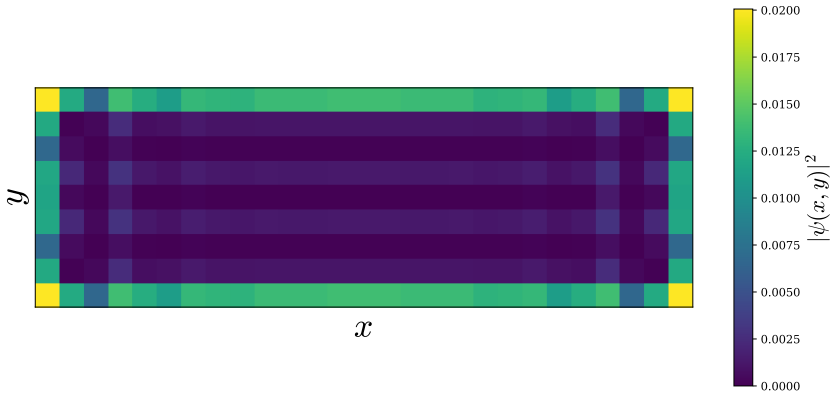

Figure 7.3: Colour plot showing the amplitude squared of an edge state wave vector for $\hat{H}_{HH}$ with $\Delta' = -J'$ and $\beta' = 1/3$. The system size was set to $N^2 = 9^2$ where N represents the number of unit cells along each axis.

Using eq. (7.48), along with the fact that $\mathcal{M}_1$ and $\mathcal{M}_2$ of the reduced Hamiltonians of $\hat{H}_{3D}$ converge to integers for $N = 9$ and $N^2 = 9^2$ respectively, then suggests that $\mathcal{M}_3$ calculated in the central unit cell of the system should converge at $N^3 = 9^3$, supporting what was found in Figure 7.2.

Before closing this section it is worth while discussing how the calculation of $\mathcal{M}_3$ was carried out. Due to $\hat{H}_{3D}$ having the form of a decoupled Hamiltonian its eigenvectors are separable. As such, to find the eigenvectors of $\hat{H}_{3D}$ we found the eigenvectors of its reduced Hamiltonians $\hat{H}_{HH}$ and $\hat{H}_{AA}$ and then took the tensor product between them. After this, we constructed the projector $\hat{P}$ at all time steps and used the same steps outlined for $\mathcal{M}_1$ to calculate $\hat{U}$. With $\hat{P}$ and $\hat{U}$ calculated for every time step, we then calculated $\mathcal{M}_3$ using eq. (7.35) along with the subsequent definitions of $\hat{A}_i$, $\hat{F}_{ij}$ and $\hat{\tilde{F}}_{ij}$ which we restate here for convenience; $\hat{A}_i = \hat{U}^\dagger \hat{P} \hat{x}_i \hat{P} \hat{U} - \hat{\tilde{P}} \hat{x}_i \hat{\tilde{P}}$, $\hat{F}_{ij} = -i[\hat{P}\hat{x}_i\hat{P}\,,\,\hat{P}\hat{x}_j\hat{P}]$, and $\hat{\tilde{F}}_{ij} = \hat{F}_{ij}(t = 0)$.

Within this section we have therefore confirmed numerically that the 3D marker correctly predicts the second Chern number of $\hat{H}_{3D}$ when it is calculated within the bulk of the system. We also showed that $\mathcal{M}_3$ correctly predicts the time-dependent dynamics of the system and indicates that something is being pumped through the 3D system over a full time period, however, it is still unclear what this object is.

8

1D quasicrystal marker

In chapter 6 and chapter 7 we developed topological markers to predict the first and second Chern numbers of 1D and 3D time-dependent systems with translational invariance. However, non-trivial topology can also be seen in quasicrystal systems that do not possess translational invariance [14, 50, 15, 51]. In this case the Chern number stated in eq. (2.28) is not well defined due to the Brillouin zone being ill defined and, as such, one cannot use this form of the Chern number to determine the topological index of quasicrystals in 1D and 2D systems.

This has previously been circumvented by considering periodic approximations of the systems and using the flux insertion method. Due to this approximation one has to consider large system sizes which is not always ideal. With this approximation one can then calculate the Chern number of the system for gaps that remain open in the thermodynamic limit (see supplementary material for [50]).

The topology of 1D quasicrystal systems has also been investigated by considering the Aubry-André model with the parameter b set to the inverse of the golden ratio, τ. It was shown that this system was topologically equivalent to the Fibonacci chain which is a known quasicrystal system [50]. The Aubry-André model is unique in that its topological index obeys a Diophantine equation due to its relationship with the Harper-Hofstadter model. This Diophantine equation is obeyed to a high degree of accuracy even if b is set to an irrational value. Unfortunately, this method requires one to know the value of b and for systems where the value of b is not obvious it is hard to apply the Diophantine

equation.

For 2D quasicrystal systems it has been shown that the Chern marker is an effective way of determining the topological indices of the system. This is due to the fact that it does not depend upon translational invariance for its evaluation. The Chern marker has been used to investigate different 2D quasicrystal tilings such as; Penrose tiling, Ammann-Beenker tiling, Dürer's tiling and the generalised Rauzy tiling [36, 79, 48, 49]. The local nature of the Chern marker also allows one to investigate how disorder affects the topology of these systems. It is important to point out that this method does not require any approximation of the quasicrystal system.

From this it is clear that current methods used to determine the topology of 1D time-dependent quasicrystal systems are not ideal as they require one to either approximate the system as periodic or consider specific Hamiltonians that possess the same topology as the desired quasicrystal Hamiltonian. It would therefore be useful if a 1D local topological marker could be constructed which could be used to determine the topological index of 1D time-dependent quasicrystal systems. This would then also allow the investigation of how disorder affects these systems.

In this chapter we adapt the 1D marker defined previously in chapter 6 such that it can be used to determine the topological index of both periodic and aperiodic 1D time-dependent systems and label it the 1D quasicrystal (QC) marker. We confirm it correctly predicts the topological index numerically by applying the 1D QC marker to the Aubry-André model with $b = 1/3$ and $b = 1/\tau$, where τ is the golden ratio, and comparing this to the topology found using the Diophantine equation. We then apply the 1D QC marker to the Rice-Mele quasicrystal model with the silver mean sequence applied; which is a known quasicrystal sequence. The Diophantine equation cannot be used for this model and therefore we check the predicted topology by analysing both the shift in the Wannier centres over a full time period along with the flow of particles across a divide placed in the bulk of the system. With this we confirm that the 1D QC marker correctly predicts the topological index of a 1D time-dependent system. We then use this marker to analyse how local disorder affects the Rice-Mele quasicrystal model with the silver mean sequence applied and also discuss the requirements a Hamiltonian needs such that the 1D QC marker correctly predicts the topological index of the system. Next, we use the 1D QC marker to investigate the topological index of the Rice-Mele quasicrystal model with the Thue-Morse sequence and Period-doubing sequence applied. These sequences are aperiodic sequences that do not possess quasiperiodic nature. Finally, we show that the evolution over time of 1D QC marker quantitatively matches the evolution of the global polarisation of the system and can therefore be used to investigate the change in the polarisation of quasicrystal systems.

8.1 1D quasicrystal marker

In chapter 6 we introduced the 1D marker for systems with translational invariance and showed that its change over a full time period gives the topological index of the system. In this section we will alter the definition of the 1D marker such that it can be used to determine the topological index of both periodic and aperiodic systems.

We first restate the 1D marker given in eq. (6.24);

$$\mathcal{M}_1(x,t) = \frac{1}{V_c}\mathrm{tr}_x\big(\hat{U}^\dagger \hat{P}\hat{x}\hat{P}\hat{U}\big). \tag{8.1}$$

We will adapt the 1D marker above to deal with aperiodic systems by first adapting its operators and then adapting its trace and prefactor. We start by analysing the projection operator, $\hat{P}$. In eq. (4.2) the projection operator was defined with a sum over occupied bands along with an integral over the Brillouin zone. This definition is ill defined for the aperiodic case and as such we choose to define it in the more general way given by

$$\hat{P} = \sum_{E=0}^{E_{FE}} |\psi_E(t)\rangle \langle\psi_E(t)| \tag{8.2}$$

where $|\psi_E(t)\rangle$ are the instantaneous eigenvectors of the Hamiltonian at time t. This definition is well defined for both periodic and aperiodic systems.

With this we now address the adiabatic evolution operator, $\hat{U}$. This operator is defined solely by the projection operator and its derivative. As such, as long as the projection operator and its derivative are well defined, which they are when using eq. (8.2), then the adiabatic evolution operator $\hat{U}$ is also well defined.

Next we address the position operator, $\hat{x}$. We previously defined the position operator as

$$\hat{\boldsymbol{x}} = \sum_{\boldsymbol{x}} \boldsymbol{x}\, |\boldsymbol{x}\rangle \langle\boldsymbol{x}| \otimes \mathbb{1} \tag{8.3}$$

where $\mathbb{1}$ had a dimension equal to the number of degrees of freedom within the unit cell. Here the degrees of freedom within the unit cell included both the lattice degrees of freedom along with the internal degrees of freedom of a particle like spin etc. Because the unit cell is ill defined for aperiodic systems we redefine the position operator by choosing $\mathbb{1}$ to have a dimension equal to the number of internal degrees of freedom of the particle only. Doing this the position operator labels the position of the particle within the system rather than labelling the unit cell the particle is in. Throughout this chapter we consider lattice models where $\boldsymbol{x} = an$ where a is the lattice spacing and n is an integer labelling the lattice site. We also only consider spinless systems and as such $\mathbb{1}$ has a dimension of 1

and therefore can be dropped.

With this all the operators in the 1D marker are now well defined for both periodic and aperiodic systems. We now move on to address the trace and its prefactor. The trace $\mathrm{tr}_{\boldsymbol{x}}$, defined in eq. (4.5), was defined as a trace over all the internal degrees of freedom of a unit cell represented by the states $|\alpha\rangle$. For translationally invariant systems the unit cell is natural length scale to trace over as all the bulk information of the system is contained within one unit cell. A similar natural length scale does not exist for aperiodic systems. Despite this there is some structure that exists in aperiodic systems due to rules that generate the aperiodic structure of the system. This may then suggest that one does not have to consider the whole of the system but just a large portion of the system. We therefore define a local trace over some region $\mathscr{R}$ in the following way

$$tr_{\mathscr{R}}(\hat{O}) = \sum_{n\in\mathscr{R}} \langle n|\, \hat{O}\, |n\rangle \tag{8.4}$$

where n labels the lattice sites of the system. We choose the region $\mathscr{R}$ to lie within the bulk of the system to ensure that we are calculating the bulk behaviour of the system. This definition then allows us to consider varying sizes of region $\mathscr{R}$ for a fixed system size and analyse what proportion of the system needs to be considered such that topological effects start to become visible.

The last object to consider in the 1D marker is the prefactor $1/V_c$. This prefactor normalised the 1D marker by the size of the unit cell and if $\mathcal{M}_1$ was taken over numerous unit cells it had to be averaged by the number of unit cells also. This then suggests that we should normalise the trace over region $\mathscr{R}$ by the length of region $\mathscr{R}$. For our systems we normalise the lattice spacing, a, to 1 and therefore the length of region $\mathscr{R}$ is given by $N_{\mathscr{R}}$ which gives the total number of lattice sites within the region $\mathscr{R}$.

With this we now define the 1D quasicrystal marker as

$$M_{QC}(x,t) = \frac{1}{N_{\mathscr{R}}}\, \mathrm{tr}_{\mathscr{R}}\Big(\hat{U}^\dagger \hat{P}\hat{x}\hat{P}\hat{U}\Big) \tag{8.5}$$

where the operators are given by their adjusted forms. Note above that we do not script M for the quasicrystal case as it is not translationally invariant. The next step is to apply the generalised $M_{QC}(x,t)$ to both a periodic system as well as an aperiodic system and check if it gives the correct topology of these systems. We carry out this analysis in the next section and use the Aubry-André model to generate the periodic and aperiodic systems.

8.2 1D QC marker and the Aubry-André model

In the previous section we defined the 1D QC marker, $M_{QC}(x,t)$. We now use it to determine the topological index of the Aubry-André model for both the periodic case, obtained by setting b to a rational fraction, and the quasicrystal case, obtained by setting b to an irrational value. We show that in both cases the change in the 1D QC marker gives the topological index of the system when the region $\mathscr{R}$ is set to a large portion of the system. We confirm the topological index of the system for the quasicrystal case by using the Diophantine equation.

The Aubry-André model was introduced in section 3.1 and is ideal model to investigate the 1D QC marker as it can model both crystalline and quasicrystalline structures and its topological structure is well known in both cases. We start by analysing the crystalline structure case first and measure its topological index using the 1D marker. From fig. 3.1 it can be seen that two topological energy gaps exist when $b = 1/3$ and $\Delta/J = -2$; one at a Fermi-energy of $\varepsilon_F/J = -1.3$ and one at $\varepsilon_F/J = 1.3$. It was shown in chapter 6 that the bottom band of the AA model has a topological index of 1. Therefore, we expect that when the Fermi-energy is set to $\varepsilon_F/J = -1.3$ the change in $M_{QC}(x,t)$ over a full time period will be 1 if it correctly represents the topological index of the system.

Figure 8.1a shows evolution of the 1D QC marker for the AA model with the parameters $b = 1/3$ and $\Delta/J = -2$. From this figure it can be seen that the change in M_{QC} over a full time period, T, gives 1 which we know is the topological index of the system. Here the region $\mathscr{R}$ was set to span 3

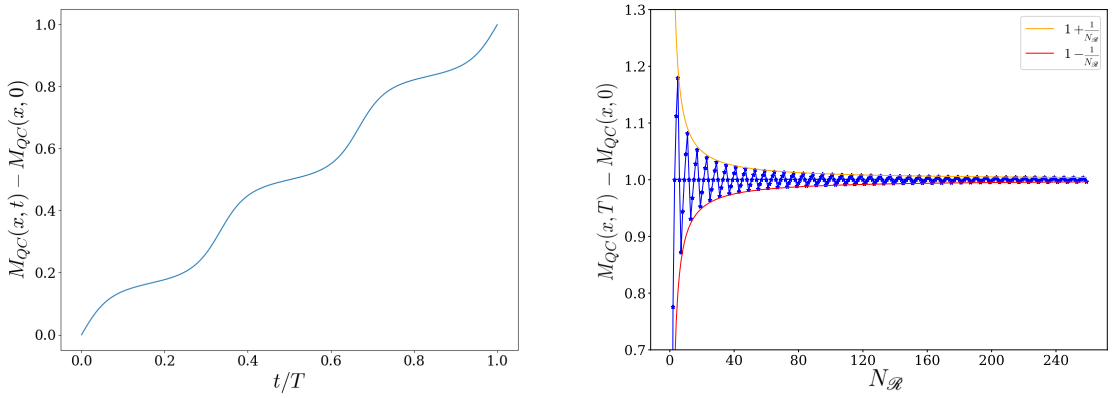

(a) (b)

Figure 8.1: Figures analysing the change in the 1D QC marker for the AA model with $\Delta/J = -2$, $b = 1/3$ and a Fermi-energy of -1.3. (a) The change in the 1D QC marker evaluated in the centre of the system with $N_{\mathscr{R}} = 3$. (b) The change in the 1D QC marker for varying values of $N_{\mathscr{R}}$ calculated in the bulk of the system. Here we set the size of the system to be 360 lattice sites in length. The lines $-1 + \frac{1}{N_{\mathscr{R}}}$ and $-1 - \frac{1}{N_{\mathscr{R}}}$ are also plotted to emphasise the envelope of the change in the 1D QC marker as it tends to the topological index of the system.

lattice sites within the bulk of the system due to the fact that the system has a well defined unit cell of size 3 lattice sites. As such, fig. 8.1a confirms that the change in M_{QC} can correctly predict the topological index of a periodic system when the region $\mathscr{R}$ is set to the size of the unit cell.

Figure 8.1b shows the change in $M_{QC}(x,t)$ over a full time period for the AA model with varying sizes of the region $\mathscr{R}$. The parameters are the same as in fig. 8.1a. The first thing to notice from this figure is that when $N_{\mathscr{R}}$ is set to a multiple of 3 the change in the 1D QC marker accurately predicts the topological index of the system. This is not surprising as in this case it is equivalent to the change in $\mathcal{M}_1$ averaged over an integer number of unit cells. The more interesting thing to notice about this figure, however, is that with increasing $N_{\mathscr{R}}$ the change in $M_{QC}(x,t)$ over a full time period tends to the topological index of the system when $N_{\mathscr{R}}$ is not equal to a multiple of 3. In this case M_{QC} tends to the topological index with an envelope of $1 + 1/N_{\mathscr{R}}$. From this it is then interesting to ask if this behaviour persists for more complex topological systems. To answer this question we consider the AA model with $b = 37/50$ and use M_{QC} to investigate one of its topological gaps.

Figure 8.2a shows the Energy spectrum for the AA model with $b = 37/50$ and $\Delta/J = -2$. From this it can be seen that a gap exists at an Energy of $E/J = -1.5$ with edge state modes crossing this gap. To determine the topology of this system we will use the Diophantine equation stated in eq. (2.41). Due to the complex structure of the AA model with $b = 37/50$ it is hard to determine the value of r for the gap at $E/J = -1.5$. As such, we rearrange the Diophantine equation by dividing through by q and notice that r/q gives the density, or the filling factor, of the system. With this the

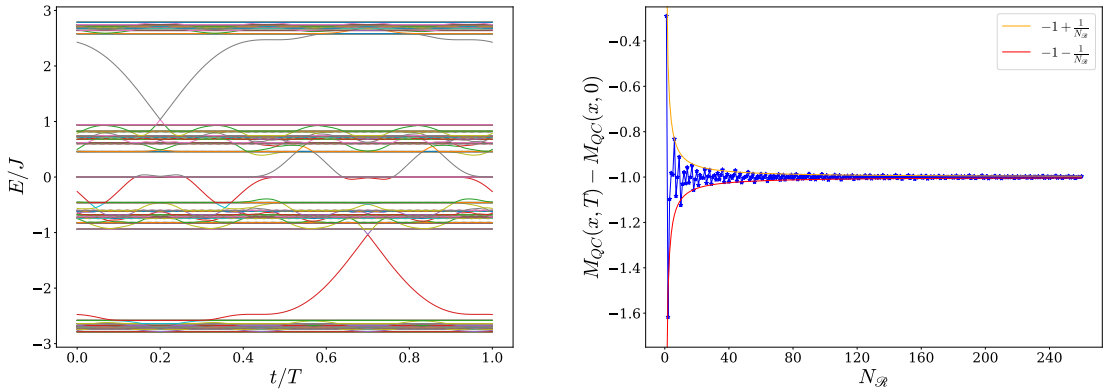

(a) (b)

Figure 8.2: Figures analysing the change in the 1D QC marker for the AAM with $\Delta/J = -2$ and $b = 37/50$. (a) The energy spectrum of the Aubry-André model. (b) The change in the 1D QC marker for varying values of $N_{\mathscr{R}}$ calculated in the bulk of the system with a Fermi-energy of $\varepsilon_F/J = -1.5$. Here we set the size of the system to be 361 lattice sites in length. The lines $-1+\frac{1}{N_{\mathscr{R}}}$ and $-1-\frac{1}{N_{\mathscr{R}}}$ are also plotted to emphasise the envelope of the change in the 1D QC marker as it tends to the topological index of the system.

Diophantine equation becomes

$$\rho = C_r\, b \;+\; t_r \tag{8.6}$$

where $b = p/q$ and ρ is the density of the system [80, 81, 82]. Using this altered version of the Diophantine equation it can be shown that the topological index of the system is -1 when the Fermi-energy is set to $\varepsilon_F/J = -1.5$.

Figure 8.2b shows the change in the 1D QC marker for the AA model with $b = 37/50$ for varying values of $N_{\mathscr{R}}$. We see from this figure that despite changing the value of b the change in the 1D QC marker still tends to the topological index of the system for increasing values of $N_{\mathscr{R}}$, which in this case is -1. As well as this, the 1D QC marker also tends to the topological index with the same envelope shape seen in the previous case. This then suggests that this tendency to the topological index of the system, along with its envelope shape, is independent of the value of b. It is then interesting to ask whether this tendency to the topological index of the system persists for irrational values of b seen as one can approximate an irrational value of b with a rational fraction that has large values for both the numerator and the denominator.

We now analyse the Aubry-André model with quasicrystalline structure using the 1D marker. It was stated previously that the AA model has the same topological structure as the Fibonacci chain, which is a known quasicrystal Hamiltonian, when $b = 1/\tau$ where $\tau = (1+\sqrt{5})/2$ is the golden ratio [50]. As such, we set b to the golden ratio in the AA model and use the 1D QC marker to analyse the topological structure of this quasicrystal Hamiltonian.

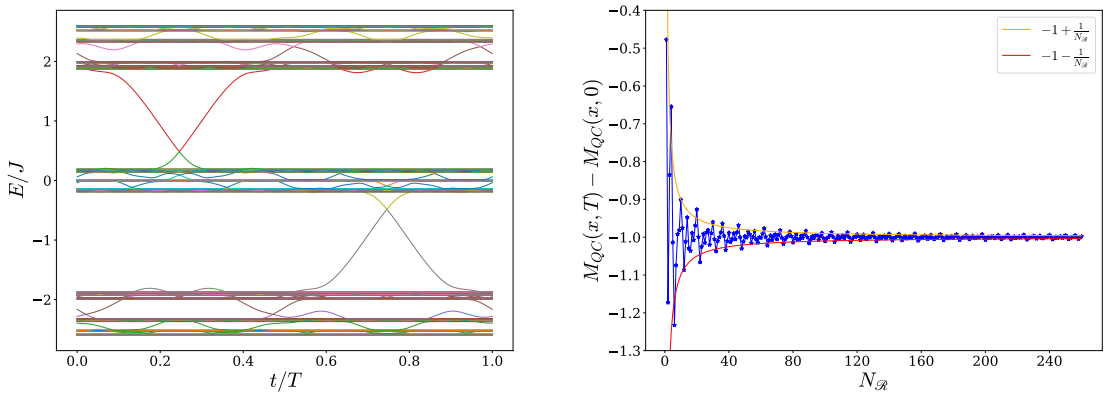

(a) (b)

Figure 8.3: Figures analysing the AAM with $\Delta/J = -2$ and $b = 1/\tau$ where τ is the golden ratio. (a) The energy spectrum of the Aubry-André model. (b) The change in the 1D QC marker for the AA model for varying values of $N_{\mathscr{R}}$ with a Fermi-energy of $\varepsilon_F/J = -1$. Here we set the size of the system to be 361 lattice sites in length. The curves $-1 + \frac{1}{N_{\mathscr{R}}}$ and $-1 - \frac{1}{N_{\mathscr{R}}}$ are also plotted to emphasise the envelope of the change in the 1D QC marker as it tends to the topological index of the system.

Figure 8.3a shows the Energy spectrum of the AA model with $b = 1/\tau$. This shows that a large gap is present around the energy $E/J = -1$, a smaller gap exists around the energy $E/J = -2.12$ and another smaller gap exists around the energy $E/J = -2.43$. It can be shown using the Diophantine given in eq. (8.6) that the topological index of the gap around $E/J = -1$ is -1, the topological index of the gap around $E/J = -2.12$ is 2, and the topological index of the gap around $E/J = -2.43$ is -3.

Figure 8.3b displays the change in the 1D marker over a time period for the AA model with $\varepsilon_F/J = -1$ and varying $N_{\mathscr{R}}$. It shows that the change in $M_{QC}(x,t)$ tends to -1 for increasing values of $N_{\mathscr{R}}$ which is the topological index of the system. This then shows that the change in the 1D QC marker over a full time period can be used to accurately determine the topology of the AA model with quasicrystalline structure when the region $\mathscr{R}$ encompasses a large portion of the system. We also see that once again the change in $M_{QC}(x,t)$ tends to the topological index with an envelope. This envelope can still be approximated by $-1 + 1/N_{\mathscr{R}}$, however, for the quasicrystal case its fit is not as accurate as the periodic case.

Up to now we have only analysed gaps with a topological index of magnitude 1. It is therefore important to check that the 1D QC marker correctly predicts the topological index of gaps with a magnitude higher than that of 1. It is also interesting to ask if the shape of the envelope changes for higher topological indices. In fig. 8.4a and fig. 8.4b we analyse the topological gaps at $E/J = -2.12$ and $E/J = -2.43$ respectively using the 1D QC marker. For each case we measure the change in $M_{QC}(x,t)$ over a full time period for increasing $N_{\mathscr{R}}$ values. From these we confirm that the change in

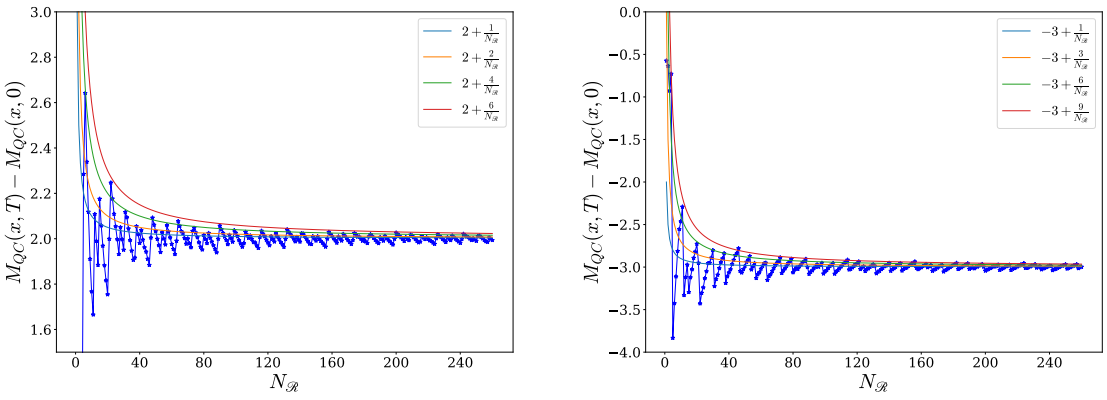

(a) (b)

Figure 8.4: Figures analysing the change in the 1D QC marker for the AAM with $\Delta/J = -2$ and $b = 1/\tau$ where τ is the golden ratio. The size of the system was set to 361 lattice sites in length. Different curves are plotted to analyse the envelope of the change in $M_{QC}(x,t)$. (a) The change in the 1D QC marker for varying values of $N_{\mathscr{R}}$ calculated in the bulk of the system with a Fermi-energy of $\varepsilon_F/J = -2.12$. (b) The change in the 1D QC marker for varying values of $N_{\mathscr{R}}$ calculated in the bulk of the system with a Fermi-energy of $\varepsilon_F/J = -2.43$.

$M_{QC}(x,t)$ tends to the topological index of the system in each case. We also plot varying curves to analyse the envelope of each case. In each case it is clear that the curve given by $C_r + 1/N_{\mathscr{R}}$, with C_r representing the topological index of the system, does not give the best fit for the envelope. This then shows that the shape of the envelope is affected by the value of C_r. Analysing fig. 8.4a it can be seen that $2 + \frac{4}{N_{\mathscr{R}}}$ and $2 + \frac{6}{N_{\mathscr{R}}}$ both fit the envelope well and analysing fig. 8.4b shows that $-3 + \frac{9}{N_{\mathscr{R}}}$ fits the envelope best. We previously showed that $-1 + \frac{1}{N_{\mathscr{R}}}$ best approximated the envelope for the topological gap at $E/J = -1$. Considering all these findings the envelope of the change in M_{QC} for the AA model with $b = 1/\tau$ can be approximated by $C_r + \frac{C_r^2}{N_{\mathscr{R}}}$ and an approximate upper bound on the error of the change in $M_{QC}(x,t)$ is given by $\frac{C_r^2}{N_{\mathscr{R}}}$ for this model.

In this section we used the 1D QC marker to analyse the topology of the Aubry-André model for both the periodic and the quasiperiodic case given by $b = 1/3$ and $b = 1/\tau$ respectively. We found that when the region $\mathscr{R}$ covers a reasonably large area of the bulk the change in $M_{QC}(x,t)$ over a full time period correctly predicts the topological index of the system in both cases. We also found that for increasingly larger regions of $\mathscr{R}$ the change in $M_{QC}(x,t)$ tended to the topological index with an envelope best approximated by $C_r + C_r^2/N_{\mathscr{R}}$ for this model. This then suggests an approximate upper bound on the error of the change in $M_{QC}(x,t)$ over a full time period of $C_r^2/N_{\mathscr{R}}$. In the next section we use M_{QC} to investigate the topological indices of the Rice-Mele quasicrystal model with the silver mean sequence applied.

8.3 1D QC marker and the Rice-Mele quasicrystal model

In the previous section we confirmed that the 1D QC marker correctly predicts the topological structure of the AA model which has known topological indices. In this section we apply the 1D QC marker to the Rice-Mele quasicrystal model with the silver mean sequence applied which has an unknown topological structure. To our knowledge there exists no adaptation to the Diophantine equation such that it can be applied to this model. Therefore, we will confirm the topological indices of the model by analysing both the shift in the Wannier centres over a full time period and the current through a boundary placed in the bulk of the system.

In section 3.4 we introduced the form of the Rice-Mele quasicrystal (RM QC) model stating that it only differed from the original Rice-Mele model by the values that f_n took. This Hamiltonian allows one to investigate any aperiodic ordering, quasiperiodic or not, and analyse how each aperiodic ordering affects the topological structure of the system. Previous studies of inhomogeneity within the original Rice-Mele model have been carried out before, however, these studies tended to concentrate on disorder induced inhomogeneity rather than structural inhomogeneity which we consider here [42]. The Rice-Mele quasicrystal Hamiltonian was first investigated with the Fibonacci sequence applied

[51]. We therefore choose to investigate another quasiperiodic sequence known as the silver mean sequence which we will introduce in a little while.

First we restate the RM QC Hamiltonian here for convenience.

$$\hat{H}_{RMQ} = \sum_n J\,|n\rangle\langle n+1| + (-1)^{f_n}\delta(t)\,|n\rangle\langle n+1| + h.c. + \sum_n (-1)^{f_n}\gamma(t)\,|n\rangle\langle n|\,,$$

$$\delta(t) = \delta_0\cos(2\pi t/T) \qquad \gamma(t) = \gamma_0\sin(2\pi t/T). \tag{8.7}$$

To regain the original Rice-Mele model one sets $f_n = n$ above which causes the sign of the modulating potentials, $\delta(t)$ and $\gamma(t)$, to alternate for each lattice site. Equally, one could set it to a sequence of alternating 1's and 0's to produce the same effect.

Before starting, it is important that we define what an aperiodic sequence is along with what a quasiperiodic sequence is and how the two differ. This will also allow us to distinguish quasicrystals from aperiodic crystals seen as the former's structure is determined by a quasiperiodic sequence and the latter's an aperiodic sequence. It is easiest to first define an aperiodic sequence as a sequence that is not periodic and is not constructed from different periodic sections joined together. It is clear then that this encompasses a large array of different sequences. A quasiperiodic sequence is a special type of aperiodic sequence which has an almost periodic nature. A more rigorous definition is that the Fourier transform of a quasicrystal system will exhibit a finite number of Bragg peaks with a well defined spacing [46, 47]. It can be shown that the Fourier transform of the silver mean sequence displays a finite number of Bragg peaks with a well defined spacing and, as such, is a quasiperiodic sequence. The Fourier transforms of the Thue-Morse sequence and the Period-doubling sequence, however, do not display this behaviour and are therefore aperiodic sequences that do not possess a quasiperiodic nature. For a more in-depth look at aperiodic sequences see [47]. With this we now move on to describe how the silver mean sequence is generated.

There are a few ways of generating aperiodic sequences, one of which is the substitution method. With this method one states a set of substitution rules, the number of which depends on how many different building blocks are present within the sequence, along with an initial value of the sequence. After this the substitution rules are applied repeatedly until one gets a sequence with the desired length. The substitution rules for the silver mean sequence are $g(A) = AAB$ and $g(B) = A$ and the initial value of the sequence is A. Using these substitution rules we find that the first four generations

of the silver mean sequence are given by

$$\begin{aligned} S_0 &= A \\ S_1 &= AAB \\ S_2 &= AABAABA \\ S_3 &= AABAABAAABAABAAAB \end{aligned} \tag{8.8}$$

with the subscript on S representing the generation number of the sequence. This sequence is quasiperiodic in nature and the ratio of A's to B's in this sequence tends to the value of the silver mean ratio, $\nu = 1 + \sqrt{2}$, when the length of the sequence becomes infinitely long [47]. We cannot apply this sequence to our Hamiltonian when it is in this form. Therefore, we use the following rule

$$f_n = \begin{cases} 1 \text{ if the } n\text{th letter of } S_i \text{ is } A \\ 0 \text{ if the } n\text{th letter of } S_i \text{ is } B \end{cases} \tag{8.9}$$

to convert our aperiodic sequence into a sequence of 0's and 1's that can be used in the RM QC Hamiltonian. The above rule can be used to convert any aperiodic sequence made up of two building blocks so that it can be applied to the Rice-Mele quasicrystal Hamiltonian.

Now that we have defined the silver mean sequence and formulated a way of applying it to our Hamiltonian we now analyse the energy spectrum of the RM QC Hamiltonian with the silver mean sequence applied.

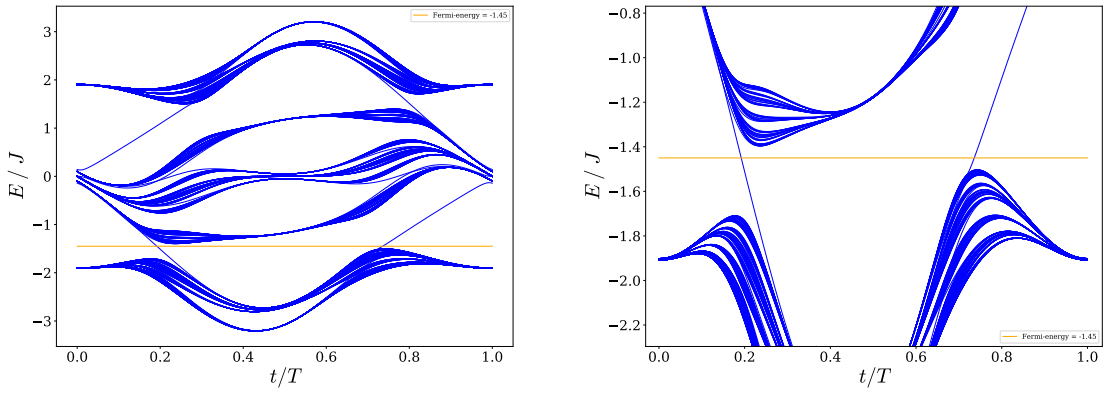

(a) (b)

Figure 8.5: Figures analysing the energy spectrum of the Rice-Mele quasicrystal model with the silver mean sequence applied. The parameters of the system were set to $\delta_0/J = 0.9$ and $\gamma_0/J = 0.8$. A line at the energy $E/J = -1.45$ was included to highlight the gap that exists at this energy value. (a) shows the full energy spectrum and (b) shows the energy spectrum around the gap at $E/J = -1.45$.

Figure 8.5 shows the energy spectrum of the RM QC Hamiltonian with the silver mean sequence applied and the parameters set to $\delta_0/J = 0.9$ and $\gamma_0/J = 0.8$. From this it can be seen that a gap exists at $E/J = -1.45$ with two eigenenergies traversing the gap over a full time period. It can be shown that the eigenvectors of these eigenenergies are exponentially localised at the edges of the system suggesting that this gap has a topological nature.

Figure 8.6 shows the change in the 1D marker evaluated in the energy gap located at $E/J = -1.45$ for varying $N_{\mathscr{R}}$. We see that the change in M_{QC} tends to the value 1 suggesting that this gap has a topological index of 1. We also see that the change in M_{QC} has an envelope best approximated by $1 + 2/N_{\mathscr{R}}$ suggesting that the approximate upper bound on the error of the change in M_{QC} for this gap is given by $2/N_{\mathscr{R}}$. While this is still of order $\mathcal{O}(1/N_{\mathscr{R}})$ it does not support our previous findings that the upper bound on the change in $M_{QC}(x,t)$ can be approximated by $C_r + C_r^2/N_{\mathscr{R}}$. As such, we can say in general that the upper bound of the change in $M_{QC}(x,t)$ over time is of order $\mathcal{O}(1/N_{\mathscr{R}})$ but a more accurate approximation of the upper bound is model dependent.

We will now check the exact topological index of this gap to confirm that the change in $M_{QC}(x,t)$ over time can predict the topological index of the Rice-Mele quasicrystal Hamiltonian. We first do this by analysing the flow of particles across a partition in the centre of the system. After this we will analyse the shift in the Wannier centres over a full time period so that we are sure of the topological

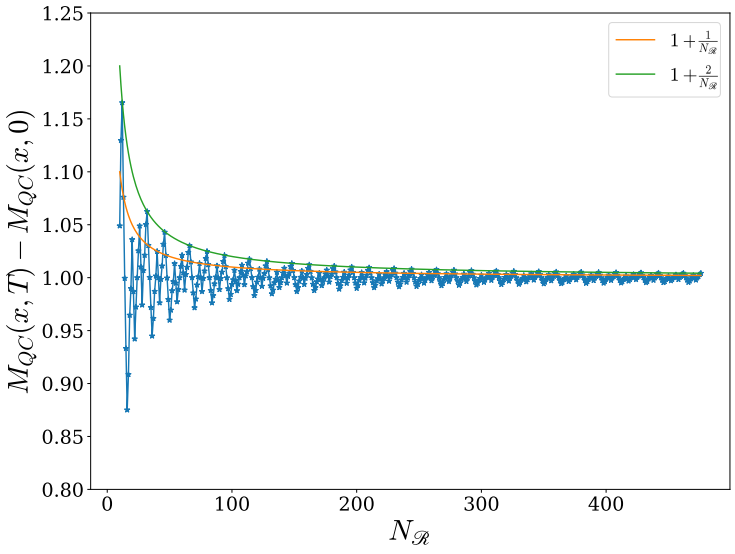

Figure 8.6: The change in the 1D QC marker for varying values of $N_{\mathscr{R}}$ for the Rice-Mele quasicrystal model with the silver mean sequence applied. The parameters of the system were set to the ones stated in fig. 8.5 and the Fermi-energy was set to $\varepsilon_F/J = -1.45$. Different curves are plotted to analyse the envelope of the change in $M_{QC}(x,t)$.

index of the system.

It was stated earlier that all 1D time dependent topological systems pump an integer amount of charge through the bulk of the system over a full time period. This quantized value is equal to the topological index of the system. Therefore, one can measure the topological index of a system by analysing the change in the particle number in one side of the system. For simplicity we will place our divide at the centre of the system. The particle number on the left hand side of the system is then given by

$$\mathcal{N}_{LHS} = \sum_{n \in LHS} \langle n | \hat{P} | n \rangle \tag{8.10}$$

where n labels the lattice sites of the system. The particle number for the right hand side of the system can be calculated in a similar way.

Figure 8.7 shows the change in the particle number on the left hand side of the system as well as the particle number for the right hand side of the system over a full time period. The most obvious part of this figure is the discontinuous jumps that are present for both $\mathcal{N}_{LHS}$ and $\mathcal{N}_{RHS}$. Comparing this figure with fig. 8.5 it can be seen that these discontinuous jumps occur when the edge state modes intersect with the Fermi-energy. The jumps are present due to the fact that the edge state modes are

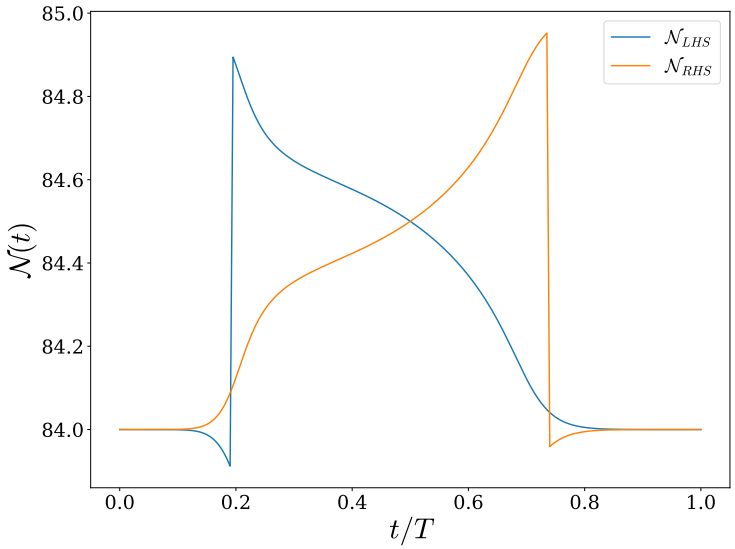

Figure 8.7: Change in the particle number on the left hand and right hand side of the system for the RM QC model with the silver mean sequence applied. Both the Fermi-energy and the parameters of the system were set to the same values as in fig. 8.6. The blue line represents the particle number for the left hand side of the system and the orange line represents the particle number for the right hand side of the system.

excluded from $\mathcal{N}_{LHS}$ (and similarly $\mathcal{N}_{RHS}$) when their energy is above the Fermi-energy. This then leads to an integer jump in the particle number. Because we are interested in the behaviour in the bulk of the system and this is clearly an edge state effect we can ignore the discontinuities. Doing this it is easy to see that the particle number on the RHS of the system increases by 1 over a full time period and the particle number on the LHS decreases by 1. This then shows that 1 particle passes through the divide placed in the centre of the system over a full time period. Here we put the divide in the centre of the system, however, it can be shown that this pumping behaviour is independent of where the divide is placed as long as it is placed within the bulk of the system. With this we have shown that over a full time period a single amount of charge is pumped through the bulk of the system. This then shows that the topological index of the system is 1 which agrees with what we previously found using $M_{QC}(x,t)$.

Next we confirm the topological index further by considering the shift in Wannier centres in the bulk of the system over a full time period. It has been shown that Wannier centres can be defined for both periodic and aperiodic systems by calculating the eigenvalues of $\hat{P}\hat{x}\hat{P}$ where the projector is defined by eq. (8.2) [83, 84, 85]. For periodic systems one can determine the topological index of a band by projecting into this band and then looking at the change in a single Wannier centre in the bulk of the system. For aperiodic systems this technique cannot be used. This is due to the fact that the aperiodic nature of the system allows the Wannier centres to move by different amounts throughout the system and therefore a single Wannier centre is not restricted to move by an integer amount over a full time period. However, there is another way in which one can use the Wannier centres to determine the topological index of an aperiodic system. This is done by analysing how many Wannier centres cross a horizontal line over a full time period. Here the horizontal line corresponds to a specific point in the system. It could be asked whether one can get different answers depending on where the horizontal line is placed. To show that this is not possible we look at a property needed for 1D time-dependent Hamiltonians to display topological pumping. For a time-dependent Hamiltonian to display topological pumping it has to be periodic in time such that $\hat{H}(0) = \hat{H}(T)$. This then restricts each Wannier centre in the bulk to have a final position equal to the initial position of the next Wannier centre. As a result, as long as the horizontal line is placed within the bulk of the system the number of Wannier centres crossing it will always be the same.

Figure 8.8 depicts the time evolution of a set of Wannier centres located in the bulk of the system for the RM QC model with the silver mean sequence applied and the same parameters as in fig. 8.6. A horizontal line is plotted in the figure and it can be seen that one Wannier centre passes up through it. This then shows that one Wannier centre passes through the position $x = 288$ suggesting that the topological index of the system is 1. This agrees with both the result found using the particle number method and the change in $M_{QC}(x,t)$. It should be noted that if the Wannier centre passes

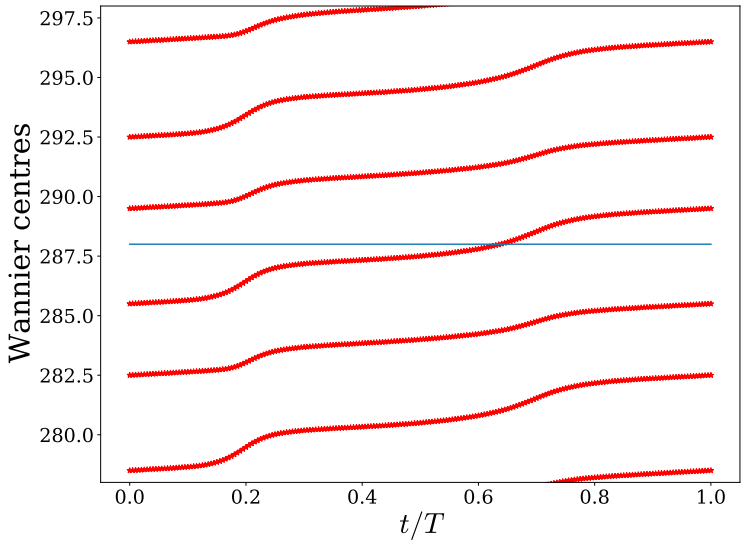

Figure 8.8: The time dependence of a set of Wannier centres in the bulk of the system for the RM QC model over a full time period. Both the Fermi-energy and the parameters of the system were set to the same values as in fig. 8.6.A horizontal line is plotted at 288.

down through the horizontal line this indicates a negative topological index.

There is also another way in which the bulk Wannier centres of the system can be used to determine the topological index of the system. Earlier we stated that Wannier centres can move by different amounts for an aperiodic system, but we know that if the system is topological in nature it should still display quantized pumping over a full time period. This then suggests that while individual Wannier centres can move by different amounts the collective behaviour of bulk Wannier centres should display a quantized amount of movement. We define M_{wan} as

$$M_{\text{wan}}(t) = \frac{1}{W_{R+1}(0) - W_0(0)} \sum_{r=0}^{R} W_r(t) \tag{8.11}$$

where W_r represents the Wannier centres in the aperiodic system and the summation is over the Wannier centres located in the region $\mathscr{R}$ at time $t = 0$. The above equation compares the average shift in all the Wannier centres in region $\mathscr{R}$ to average the distance between the Wannier centres at time $t = 0$. The change in this over a full time period will then give the topological index of the system. Here the idea is that the topological index is equal to the number of particles pumped through the system and the change in $M_{wan}(t)$ over a full time period tells us how many particles are pumped across the region $\mathscr{R}$ over a full time period. We show the evolution of $M_{wan}(t)$ over a full time period

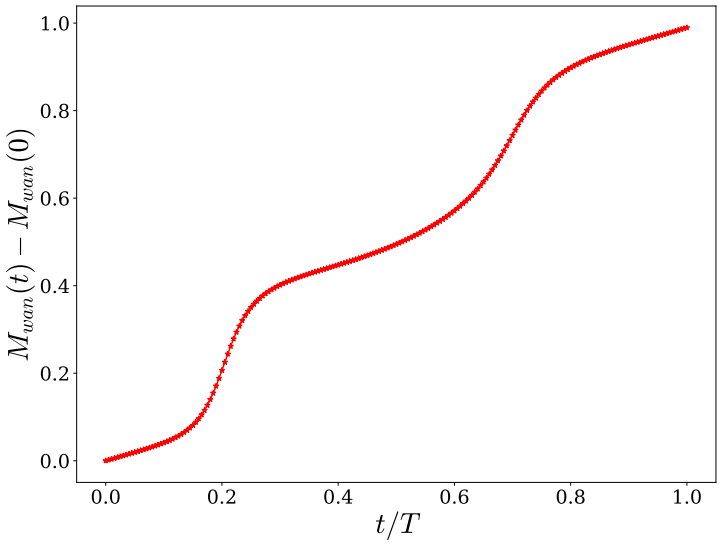

Figure 8.9: Change in $M_{wan}(t)$ for the RM QC model over a full time period. Both the Fermi-energy and the parameters of the system were set to the same values as in fig. 8.6. The region $\mathscr{R}$ spanned from $x = 145.5$ to $x = 429.5$ with the size of the system set to 577 lattice sites.

in fig. 8.9. From this figure it can be seen that the change in $M_{wan}(t)$ over a full time period is 1 and therefore gives the topological index of the system.

It is then interesting to compare the accuracy of the change in M_{QC} and M_{wan} over a time period relative to the topological index of the system. Figure 8.10 plots the error for both the change in $M_{QC}(x,t)$ and $M_{wan}(t)$ over a full time period compared to the true topological index of the system. From this it can be seen that on average the change in $M_{wan}(t)$ has a higher error compared to the change in $M_{QC}(x,t)$. The figure also shows the curve $1/N_{\mathscr{R}}$ which highlights that the error for the change in both $M_{QC}(x,t)$ and $M_{wan}(t)$ has a $1/N_{\mathscr{R}}$ behaviour.

With this we have shown that the change in $M_{QC}(x,t)$ over a full time period correctly predicts the topological index of two different aperiodic systems. We have also introduced a few other ways of finding the topological index of an aperiodic system. It is therefore worth discussing the advantages of the 1D QC marker. One advantage of the 1D QC marker is that it naturally produces an single value which determines the topological index of the system. This is a useful property when analysing phase transitions within a topological system. This property is not naturally present for the change in particle number method or the analysis of individual Wannier centres in the bulk due to the fact that discontinuities can arise in these methods. We also showed that while this property is present for $M_{wan}(t)$, the change in $M_{QC}(x,t)$ provides a more accurate calculation of the topological index of the

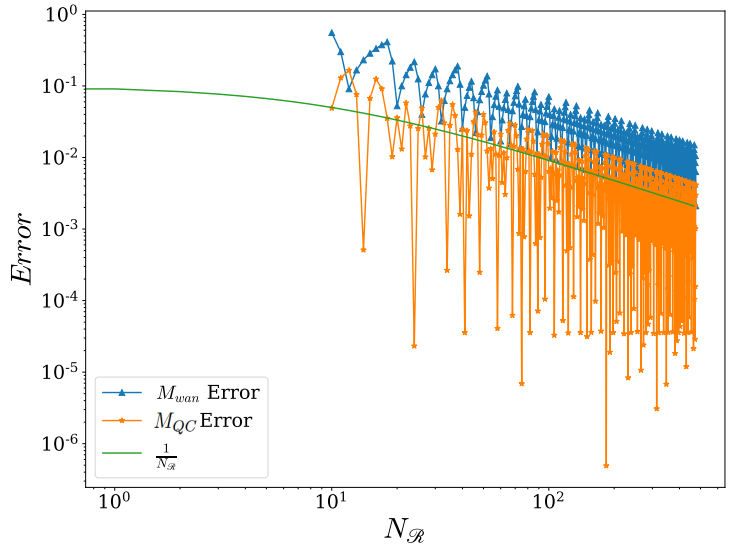

Figure 8.10: The error for both the change in $M_{QC}(x,t)$ and $M_{wan}(t)$ over a full time period compared to the true topological index of the system for varying region sizes given by $N_{\mathscr{R}}$. Both the Fermi-energy and the parameters of the system were set to the same values as in fig. 8.6. The curve $1/N_{\mathscr{R}}$ is also plotted.

system.

Another advantage of $M_{QC}(x,t)$ is its local nature which allows one to calculate the topological index of a specific region in the system. This can then be used to determine how local disorder affects the topological index for different areas of the system. To demonstrate this property we consider the RM QC model studied in this section with a length of 1000 lattice sites. We add local disorder to the system by setting the value of f_n to 1 for the 440th to the 449th lattice sites of the system breaking the aperiodic sequence in this region. Next, we then divide the system into 10 regions, each 100 lattice sites in length, and measure the topological index of each region using the change in $M_{QC}(x,t)$ over a full time period. It was shown in fig. 8.6 that the upper bound for the error on the change in $M_{QC}(x,t)$ is best described by $2/N_{\mathscr{R}}$. Using this, the upper bound on the error for the change in M_{QC} for a region of size $N_{\mathscr{R}} = 100$ is ± 0.02. Therefore, if the region is topological in nature we expect the change in $M_{QC}(x,t)$ to be 1 ± 0.02.

Figure 8.11 shows the change in M_{QC} over a full time period measured for each region. An error bar of ± 0.02 is also included for each point. It is clear from this figure that the defect lies within the 4th region of the system seen as the change in M_{QC} for this region is not equal to an integer to within the error. It can also be seen that the change in M_{QC} for the other regions of the system gives an integer value to within the tolerance of M_{QC}, neglecting the edge regions which do not give integer

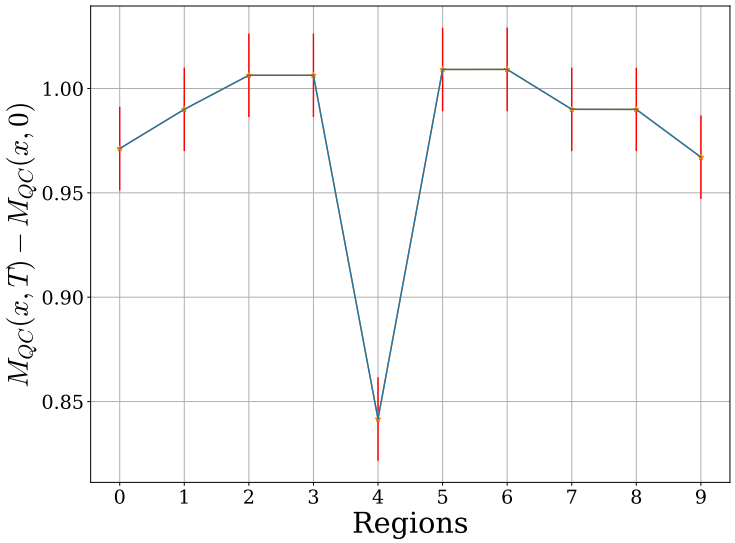

Figure 8.11: Change in $M_{QC}(x,t)$ over a full time period for the RM QC model with a local defect placed inn the system. The system has a length of 1000 lattice sites and was split into 10 regions of 100 lattice sites. The change in M_{QC} was then measured for each region. Both the Fermi-energy and the parameters of the system were set to the same values as in fig. 8.6. Error bars of ± 0.02 are included with the error tolerance calculated using $2/N_{\mathscr{R}}$.

values due to edge state effects. This then suggests that topological pumping will still be present within the regions of the system far from the defect.

In this section we have shown that the change in $M_{QC}(x,t)$ correctly determines the topological index of the Rice-Mele quasicrystal model. This, coupled with what was shown in section 8.2, shows that the change in $M_{QC}(x,t)$ over a full time period is a robust way of measuring the topological index of an aperiodic system. We also introduced other ways of determining the topological index of aperiodic systems, but then highlighted the advantages the 1D QC marker has over these other methods. Finally, we used M_{QC} to investigate how local disorder affects the topological structure in different regions of the system and found that the topological indices of regions away from the local disorder are unaffected suggesting that topological pumping is still present within these regions. It is then interesting to ask whether this means that topological pumping across the system could persist with the defect acting as a potential energy barrier that has to be surmounted. This question is not considered within this thesis, but could be a future avenue of investigation.

8.4 Requirements of the 1D QC marker

So far we have used the 1D QC marker on the Aubry-André model and the Rice-Mele quasicrystal model with an applied quasiperiodic sequence and found that the change in $M_{QC}(x,t)$ over a full time period correctly predicts the topological index of a system when calculated over a large area. It is then pertinent to ask when the 1D QC marker does not correctly predict the topological index of a system even if it is measured over a large portion of the system. To answer this we point out that to analyse the topological structure of the Fibonacci chain we analysed the topological structure of the AA model with $b = 1/\tau$ rather than the Fibonacci chain itself. This is because the Fibonacci chain possesses discontinuous jumps in its energy spectrum which cause problems for the 1D QC marker. To demonstrate these discontinuous jumps we define the Fibonacci chain Hamiltonian below and show its energy spectrum.

We start by first writing down the Fibonacci chain Hamiltonian given by

$$\hat{H}_{FC} = \sum_n \Big[\big(t_b + V_n^F (t_a - t_b)\big) \left|n+1\right\rangle \left\langle n\right| + \big(\epsilon_b + V_n^F (\epsilon_a - \epsilon_b)\big) \left|n\right\rangle \left\langle n\right| \Big]. \tag{8.12}$$

Here V_n^F represents the elements of the Fibonacci sequence when converted to the binary form using eq. (8.9). When $V_n^F = 1$ then the hopping parameter for that site takes the value of t_a and its onsite potential takes the value of ϵ_a; when $V_n^F = 0$ the hopping parameter is given by t_b and the onsite potential is given by ϵ_b.

As mentioned earlier the values of V_n^F can be determined in a few different ways. Here we use a different method from the substitution rules as it allows us to see the discontinuous nature in time of the Hamiltonian. Another method for generation the Fibonacci sequence is using the equation

$$V_n^F = 2\Big(\lfloor (n+2)/\tau \rfloor - \lfloor (n+1)/\tau \rfloor \Big) - 1 \tag{8.13}$$

where $\tau = (1+\sqrt{5})/2$ is the golden ratio and $\lfloor x \rfloor$ is the floor function. The above equation gives the Fibonacci sequence in terms of 1's and -1's, but one can easily change the sequence to be in terms of 1's and 0's by adding 1 to the sequence and then dividing by 2. It is known that eq. (8.13) is equal to [50]

$$\chi_n = sign\Big[\cos(2\pi b(n+1) + \pi b + \phi) - \cos(\pi b) \Big] \tag{8.14}$$

when $\phi = 0$. Above $sign[x]$ is -1 if $x > 0$ and 1 if $x < 0$ and $b = 1/\tau$. Again this can easily be changed to a sequence of 0's and 1's using the method previously mentioned. The value ϕ is a constant phase and varying ϕ generates a family of Fibonacci chains. From this we can define the time-dependent Fibonacci chain Hamiltonian by setting $\phi = 2\pi t/T$, where T is the time period of the system. Doing

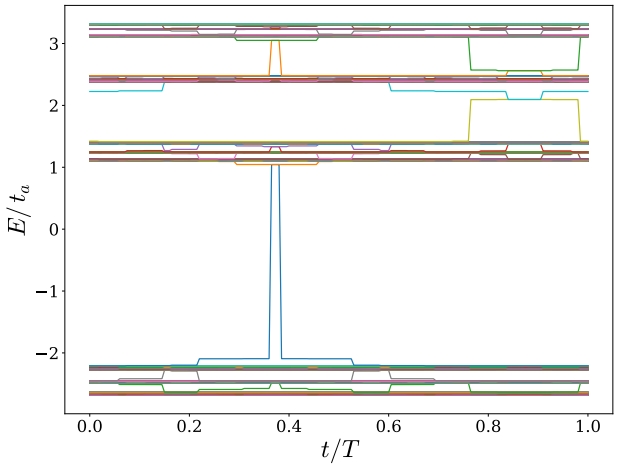

Figure 8.12: The energy spectrum of the diagonal Fibonacci chain with $t_b = t_a$ and $\epsilon_a = -\epsilon_b = 2t_a$.

this the time-dependent Fibonacci chain Hamiltonian is defined in the following way

$$\hat{H}_{FC}(t) = \sum_n \Big[\big(t_b + \chi_n(t)\,(t_a - t_b)\big)\,|n+1\rangle\langle n| + \big(\epsilon_b + \chi_n(t)\,(\epsilon_a - \epsilon_b)\big)\,|n\rangle\langle n| \Big]. \tag{8.15}$$

With the time-dependent Fibonacci chain Hamiltonian defined we can now show its discontinuous nature in time. The energy spectrum of the diagonal Fibonacci chain is shown in fig. 8.12. From this figure the abrupt changes in the energies of the edge state modes are apparent, but these abrupt changes are also present in the bulk modes which are harder to see. It is not surprising that these abrupt changes arise in all the modes because we are taking the sign of a function that is dependent on time. As such, at some point in time the energy of a given mode will abruptly change causing discontinuous jumps in the energy of that mode.

Due to these discontinuous changes the adiabatic approximation breaks down for this model and thus the 1D QC marker cannot correctly calculate the topological index of this model. Therefore, to investigate the topology of this model one has to investigate the topology of the Aubry-André model with $b = 1/\tau$ where τ is the golden ratio.

From this we conclude that for the generalised 1D marker to correctly indicate the topological index of the system the Hamiltonian needs to be continuous in time such that the adiabatic approximation can be applied. With this the adiabatic evolution operator can then be used to correctly evolve the projection operators in time. Seen as the projection operator and the position operator can be well defined for any Hamiltonian the adiabatic requirement is only needed to ensure the adiabatic evolution operators correctly evolve the system in time. Therefore, if the true time-dependent evolution operator is known the 1D marker can be used to calculate the topological structure by replacing the adiabatic

evolution operator with the true time-dependent evolution operator.

8.5 Thue-Morse and Period-doubling sequence

Previously, we considered the Rice-Mele quasicrystal model with the silver mean sequence applied. Previous work has been done investigating the topological structure of quasicrystals, mainly Fibonacci quasicrystal chain, however, it is suspected that other non-periodic sequences can also possess topological properties. The topological properties of these aperiodic, but non-quasicrystal, sequences have previously been hard to study due to the fact that no topological mapping has been found between systems with these sequences and the Aubry-André model [81]. On the other hand, these sequences can be directly applied to the Rice-Mele quasicrystal model which then allows the topological effects of these aperiodic sequences to be investigated in terms of this model. As such, in this section we will apply both the Thue-Morse and the Period-doubling aperiodic sequences to the RM QC model and investigate how these aperiodic sequences affect the topological structure of this system. We will use the change in $M_{QC}(x,t)$ to determine the topological indices of the system.

We first analyse the topological structure of the RM QC with the Thue-Morse sequence applied. This sequence is generated using the following substitution rules $g(A) = AB$ and $g(B) = BA$ with the initial value of the sequence set to A. We show a few generations of the sequence below;

$$\begin{aligned} T_1 &= AB \\ T_2 &= ABBA \\ T_3 &= ABBABAAB \\ T_4 &= ABBABAABBAABABBA \end{aligned} \tag{8.16}$$

The Thue-Morse sequence is an aperiodic sequence but is not quasiperiodic in nature. One way of seeing this is by analysing the ratio of A's to B's in the sequence. For the Thue-Morse sequence this ratio is 1 for any sequence length greater than 1 and not an irrational value like it was for the silver mean sequence. With the sequence defined we can now use eq. (8.9) to apply this sequence to the RM QC.

Figure 8.13 shows the energy spectrum for the RM QC model with the Thue-Morse sequence applied. The parameters of the system were set to $\delta_0/J = 0.9$ and $\gamma_0/J = 0.8$. From the energy spectrum it can be seen that 2 gaps exist around $E/J = -1.2$ and $E/J = 1.2$. It can also be shown that the energy modes that traverse these gaps are localised on the edge of the system suggesting that the gaps are topological in nature. For our analysis we will concentrate on the gap that exists at $E/J = -1.2$ and calculate the topological index of this gap using $M_{QC}(x,t)$.

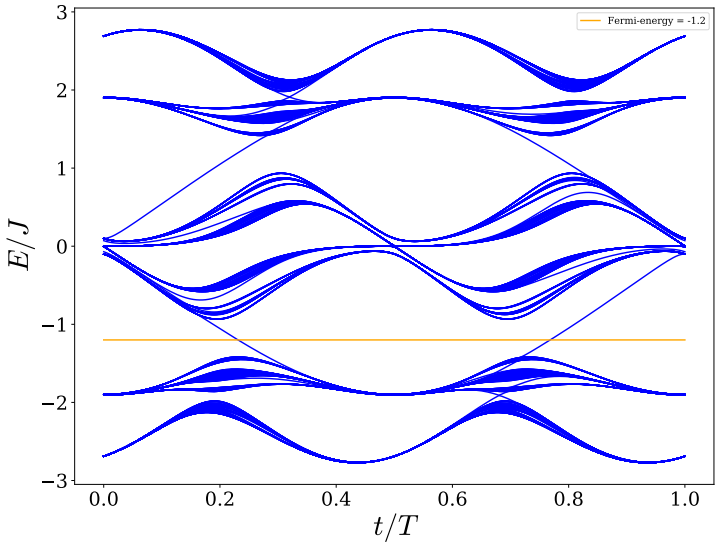

Figure 8.13: Energy spectrum of the Rice-Mele quasicrystal model with the Thue-Morse sequence applied. The parameters of the system were set to $\delta_0 = 0.9/J$ and $\gamma_0/J = 0.8$. A line at $E/J = -1.2$ is also plotted to highlight the gap present at this energy.

Figure 8.14 shows the topological analysis for the RM QC model with the Thue-Morse sequence applied. Figure 8.14a shows how $M_{QC}(x,t)$ evolves over time and that over a full time period it changes by 1 showing that this gap has a topological index of 1. Figure 8.14b displays the change in $M_{QC}(x,t)$ over a full time period for varying values of $N_{\mathscr{R}}$. Again we see that the change in M_{QC} tends to the topological index of the system for increasing $N_{\mathscr{R}}$. We also see the envelope of the tendency is of order $\mathcal{O}(1/N_{\mathscr{R}})$. It is interesting to point out that for the RM QC model with the Thue-Morse sequence applied the envelope is best described by $C_r + 1/N_{\mathscr{R}}$ and not $C_r + 2/N_{\mathscr{R}}$ which best described the RM QC model with the silver mean sequence applied. This then shows that the approximate upper bound for the change in M_{QC} is dependent also on the applied sequence of the model as well as the model itself.

It can also be seen that there are narrow gaps at $E/J = -1.95$ and $E/J = 1.95$. It can be confirmed using $M_{QC}(x,t)$ that these gaps are also topological in nature. Calculating the topological structure for the energy spectrum shown in fig. 8.13 we find that the topological indices for the gaps at $E/J = -1.95, -1.2, 1.2, 1.95$ are 1, 1, 1, 1 respectively. These values can be confirmed by using the Wannier centres method or the change in particle number method introduced in the previous section.

With this we have shown that the RM QC model with the Thue-Morse sequence applied possesses topological gaps and displays topological pumping. This then shows that topological behaviour can

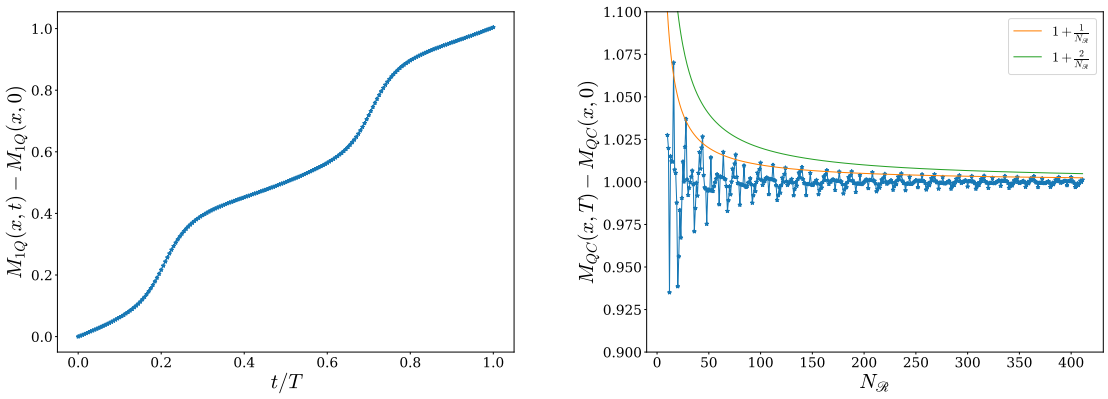

(a) (b)

Figure 8.14: Figures analysing the change in the 1D QC marker for the RM QC model with the Thue-Morse sequence applied and $\delta_0/J = 0.9$ and $\gamma_0/J = 0.8$. The Fermi-energy was set to $\varepsilon_F/J = -1.2$ and the size of the system was set to 512 lattice sites in length. (a) The change in the 1D QC marker for $N_{\mathscr{R}} = 256$. The change of $M_{QC}(x,t)$ over a full time period is 1.004 (b) The change in the 1D QC marker for varying values of $N_{\mathscr{R}}$. Different decay profiles are plotted to analyse the envelope of the change in $M_{QC}(x,t)$.

be induced by aperiodic sequences that are not quasiperiodic in nature.

Next we will apply the Period-doubling sequence to the RM QC model and show it can also produce gaps with no trivial topology. We first introduce the Period-doubling sequence which is generated by setting the initial value to A and then using the following substitution rules; $g(A) = AB$ and $g(B) = AA$. Below we show the first few generations of this sequence

$$\begin{aligned} T_1 &= AB \\ T_2 &= ABAA \\ T_3 &= ABAAABAB \\ T_4 &= ABAAABABABAAABAA \end{aligned} \tag{8.17}$$

Like the Thue-Morse sequence, this sequence is aperiodic but is not quasiperiodic in nature. This is demonstrated by the fact that for this sequence the ratio of A's to B's tends to the value of 2 and not a irrational number which is the case for quasiperiodic sequence. Once again we use eq. (8.9) to convert the sequence to a binary sequence so that it can be applied to the RM QC model.

Doing this the energy spectrum of the RM QC model with the Period-doubling sequence can be found. Figure 8.15 shows the energy spectrum of this model with the parameters $\delta_0/J = 0.75$ and $\gamma_0/J = 0.25$. From this figure it can be seen that a gap is present at $E/J = 0$ with two energy modes traversing this gap. It can be shown that these modes are exponentially localised at the edges of the

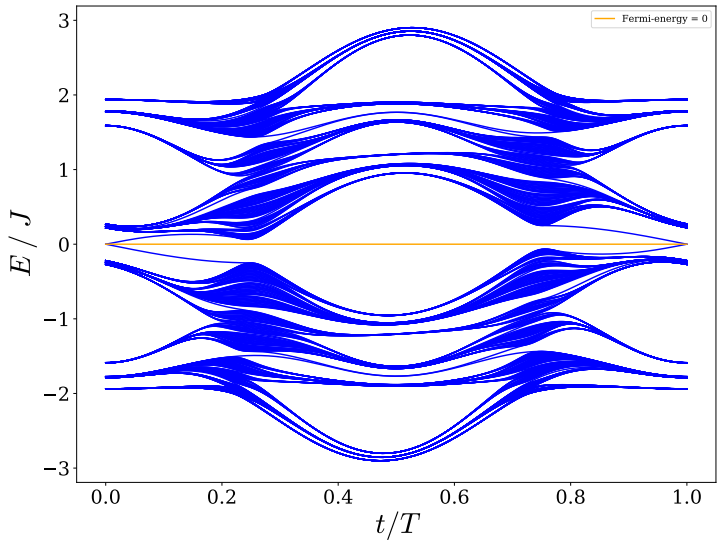

Figure 8.15: Energy spectrum of the Rice-Mele quasicrystal model with the Period-doubling sequence applied. The parameters of the system were set to $\delta_0 = 0.75/J$ and $\gamma_0/J = 0.25$. A line at $E/J = 0$ is also plotted to highlight the gap present at this energy.

system suggesting that this gap is topological in nature and we confirm this using the 1D QC marker.

Figure 8.16 analyses the change in $M_{QC}(x,t)$ for the RM QC model with the Period-doubling sequence applied. The parameters of the system were set to the same as in fig. 8.15 and the Fermi-energy was set to $\varepsilon_F/J = 0$. Figure 8.16a shows how the change in the 1D QC marker evolves over a full time period and shows that its total change is equal to 1. Here we set the region $\mathscr{R}$ to cover half the system. This then shows that the topological index of the gap shown in fig. 8.15 is 1 and that this model can display topological pumping. Figure 8.16b shows the change in the 1D QC marker over a full time period for varying $N_{\mathscr{R}}$ for the same system. In this figure it is shown that the change in M_{QC} tends to the value of 1 for increasing $N_{\mathscr{R}}$ which agrees with the finding that the topological index of the system is 1. From this figure it can also be seen that the envelope of the change in M_{QC} for this model is best described by $C_r + 2/N_{\mathscr{R}}$ which is different from the envelope behaviour seen when the Thue-Morse sequence was applied.

We have therefore shown in this section that the Rice-Mele quasicrystal model can possess gaps with non-trivial topological indices when both the Thue-Morse and Period-doubling sequences are applied. This shows that topological behaviour can be induced by aperiodic sequences that are not quasiperiodic in nature.

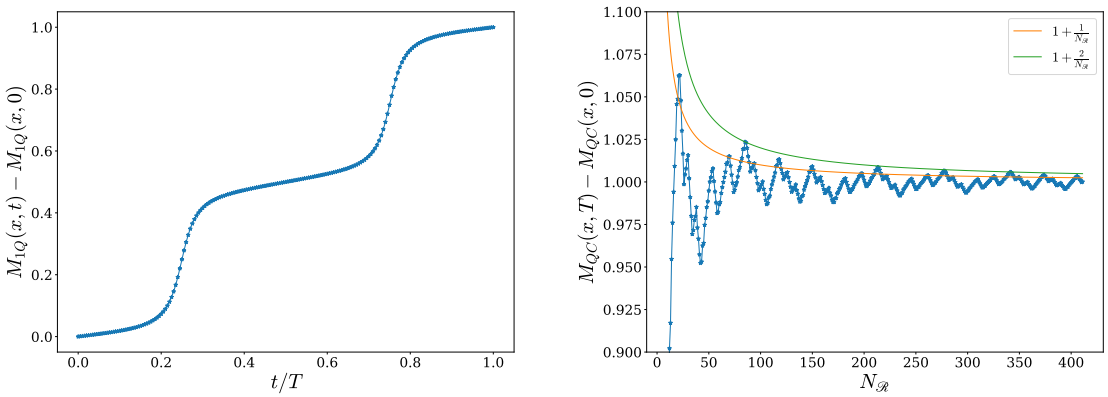

(a) (b)

Figure 8.16: Figures analysing the change in the 1D QC marker for the RM QC model with the Period-doubling sequence applied and $\delta_0/J = 0.75$ and $\gamma_0/J = 0.25$. The Fermi-energy was set to $\varepsilon_F/J = 0$ and the size of the system was set to 512 lattice sites in length. (a) The change in the 1D QC marker for $N_{\mathscr{R}} = 256$. The change of $M_{QC}(x,t)$ over a full time period is 1.004 (b) The change in the 1D QC marker for varying values of $N_{\mathscr{R}}$. Different decay profiles are plotted to analyse the envelope of the change in $M_{QC}(x,t)$.

8.6 Polarisation and the 1D QC marker

In previous sections we have shown that the change in the 1D QC marker over a full time period correctly indicates the topological index of the system with both periodic and aperiodic structure. It is also well known from the modern theory of polarisation that the change in the global polarisation of the system over a full time period is linked to the topological structure of the system for transitionally invariant systems [23]. It is therefore interesting to ask how the change in the 1D QC marker is related to the global polarisation of systems with aperiodic order seen as the global polarisation is an important property of the system. Throughout this section we show that the evolution of $M_{QC}(x,t)$ over a time interval quantitatively matches the evolution of the polarisation over the same time interval to a high degree and the two become equivalent in the thermodynamic limit when the region $\mathscr{R} \to \infty$.

It is known that for 1D systems with open boundary conditions the global polarisation of the system is represented by the dipole moment per unit length [22];

$$P_{el}\,(t) = \frac{1}{N}\mathrm{Tr}(\hat{P}\hat{x}) = \frac{1}{N}\int dx\; x\; \rho(x) \tag{8.18}$$

where N is the length of the system, $Tr(\hat{O})$ is the trace over the whole system and $\rho(x)$ is the density. As such, we will compare the evolution of $M_{QC}(x,t)$ to the evolution of $P_{el}(t)$ to investigate their relation to one another.

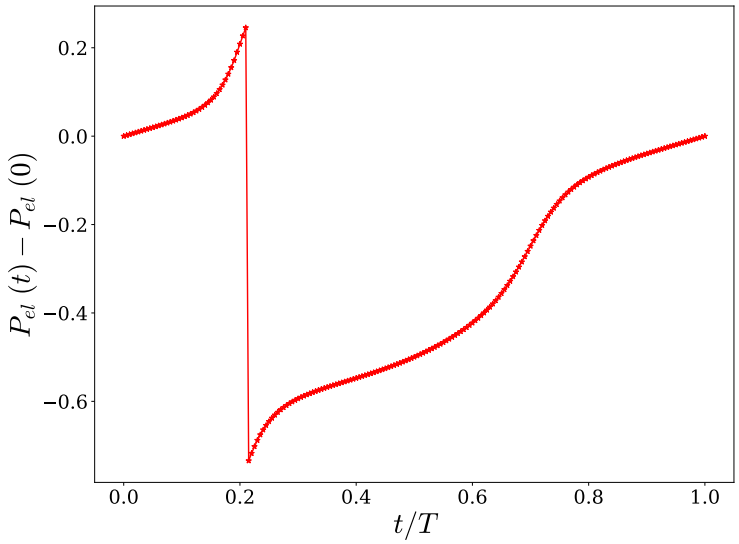

Figure 8.17: The time evolution of the global polarisation, P_{el}, over a full time period for the RM QC model with the silver mean sequence applied. The parameters of the system are the same as in fig. 8.6 and the system size was set to $N = 1393$.

We start by plotting the evolution of $P_{el}(t)$ for the RM QC model with the silver mean sequence applied. This evolution can be seen in fig. 8.17 where the parameters of the system were set to those given in fig. 8.6. From this figure one can see the characteristic discontinuity in the polarisation which has a magnitude of one. For the open boundary case this discontinuity is caused by the edge state mode located on the right of the system crossing the Fermi-energy and no longer being included in the calculation of P_{el}. These types of discontinuities would not appear for the periodic boundary case, but in this case eq. (6.23) does not give the global polarisation due to $\hat{x}$ being multivalued for the periodic boundary case. The magnitude of the discontinuity is one due to the fact that the right edge state mode is exponentially localised at the position $x = N$ and therefore contributes a value of one to P_{el}. As a result, when the right edge state mode has an energy greater than the Fermi-energy it is not included in the calculation of P_{el} causing P_{el} to decrease by one. This confirms that the discontinuity in P_{el} is a purely edge state effect and because $M_{QC}(x,t)$ only considers bulk behaviour we will ignore the discontinuity when comparing the two; also note that this discontinuity will disappear in the thermodynamic limit when $N_{\mathscr{R}} \to \infty$. We also point out that there is no discontinuity when the left edge state mode crosses the Fermi-energy. This is because the left edge state mode is exponentially localised at $x = 1$ and there for its contribution to P_{el} is $1/N$ which is negligible for large N.

Figure 8.18 shows the evolution of $M_{1Q}(x,t)$ over a full time period for the RM QC model with the

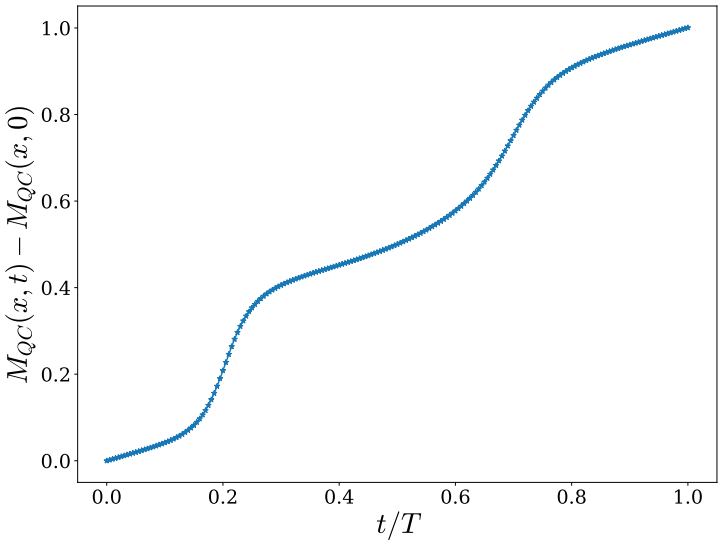

Figure 8.18: The time evolution of $M_{1Q}(x,t)$ over a full time period for the RM QC model with the silver mean sequence applied. The parameters of the system along with the Fermi-energy and the number of lattice sites are the same as in fig. 8.17 and the region $\mathscr{R}$ encompassed the sites from $N = 348$ to $N = 1044$. There is no discontinuity here because we are only considering a region in the bulk of the system.

silver mean sequence applied. The region $\mathscr{R}$ extended from $x = 348$ to $x = 1044$ and the parameters were set to those in fig. 8.17. Comparing fig. 8.17 and fig. 8.18 one can immediately see that the general shape of each curve is very similar when the discontinuity is neglected.

Figure 8.19 compares the time evolution of the polarisation to the time evolution of the 1D QC marker over a full time period for the RM QC model with the silver mean sequence applied. This figure shows that the time evolution of $P_{el}(t)$ and $M_{QC}(x,t)$ quantitatively match to a high degree of accuracy when the discontinuity from $P_{el}(t)$ is ignored. Therefore, one can use $M_{QC}(x,t)$ to determine the polarisation of the system at any time t. It can also be shown that the slight discrepancy between these two values decreases when the region $\mathscr{R}$ is increased whilst keeping the edge state regions $\mathscr{A}$, which cover the rest of the system not contained within $\mathscr{R}$, the same size. From this it can then be seen that in the thermodynamic limit, when $N_{\mathscr{R}} \to \infty$ and region $\mathscr{A}$ is fixed, the evolution of $M_{QC}(x,t)$ is equal to the global polarisation of the system.

We have thus shown that $M_{1Q}(x,t)$ can be used to determine the global polarisation of the system at any time t when $N_{\mathscr{R}}$ is set to a large value. We also showed that in the thermodynamic limit $M_{1Q}(x,t)$ tends to the global polarisation. Whilst we have been primarily interested in topological systems where the polarisation changes by quantized values throughout this thesis, it is important to

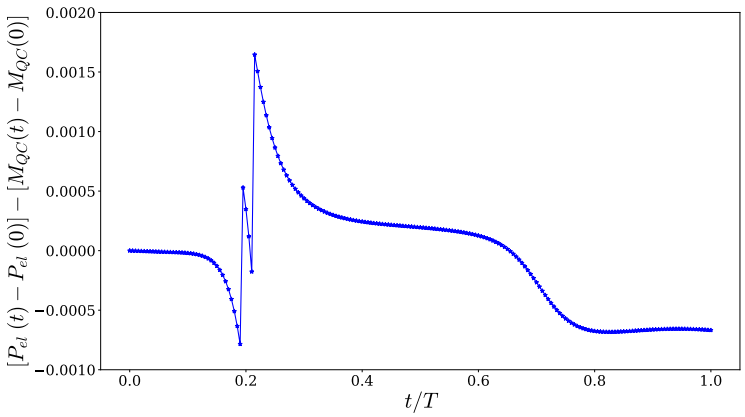

Figure 8.19: The difference between the time evolution of $M_{1Q}(x,t)$ and the time evolution of $P_{el}(t)$ over a full time period for the RM QC model with the silver mean sequence applied. The parameters of the system along with the Fermi-energy and the number of lattice sites are the same as in fig. 8.17 and the region $\mathscr{R}$ encompassed the sites from $N = 348$ to $N = 1044$.

note that $M_{QC}(x,t)$ can also be used to determine the bulk polarisation of non-topological systems, both periodic and aperiodic, where the polarisation of the system is important.

8.7 Conclusion

To conclude this chapter we will discuss its relevant findings. Within this chapter we defined the 1D quasicrystal marker such that it could be applied to both periodic and aperiodic crystal structures. We then applied it to Aubry-André model for both rational and irrational values of the parameter b. In both cases it was found that the change in $M_{QC}(x,t)$ tended to the topological index of the system with increasing $N_{\mathscr{R}}$ and therefore, when $N_{\mathscr{R}}$ is reasonably large, the change in $M_{QC}(x,t)$ over a full time period correctly predicts the topological index of the system. We also found that the envelope of the change in $M_{QC}(x,t)$ over a full time period could be approximated by $C_r + C_r^2/N_{\mathscr{R}}$ for the Aubry-André model which gives an approximate upper bound on the error of the change in $M_{QC}(x,t)$ to be $C_r^2/N_{\mathscr{R}}$ for this model. This can then be used to estimate the size of region $\mathscr{R}$ needed to determine the topological index of the Aubry-André model to a certain degree of accuracy.

We next applied M_{QC} to the Rice-Mele quasicrystal model with the silver mean sequence applied and found that the change in M_{QC} again tended to the topological index of the system for increasing $N_{\mathscr{R}}$. For this model the envelope of the change in M_{QC} was best described by $1 + 2/N_{\mathscr{R}}$ when the system had a topological index of one. This does not agree with the $C_r + C_r^2/N_{\mathscr{R}}$ found for the Aubry-André model. As such, the approximate upper bound for the change in M_{QC} over a full time period

can best be described by $\alpha/N_{\mathscr{R}}$ where alpha is of order unity of low values of the topological index and the exact form of α is model dependent. In this section we also introduced three other ways of determining the topological index of the system. We then pointed out that while these other methods have their place in the determination of topological indices they are either less accurate than the 1D QC marker, require visual analysis of a graph, or possess unwanted discontinuities. Another advantage of $M_{QC}(x,t)$ is that it has a natural generalisation to higher dimensional systems. The 3D marker defined in section 7.2 can be adapted in a similar way to the 1D marker to generate a 3D quasicrystal marker which could be used to determine the second Chern number of a system. Higher dimensional generalisations of methods using the Wannier centres is not trivial seen as Wannier functions can only be exponentially localised in one dimension. Higher dimensional generalisations of the particle number method are also nontrivial seen as it is not clear what is being pumped in the 3D case. We also showed that $M_{QC}(x,t)$ can be used to determine the topological index of specific regions in the system thus allowing it to be used to investigate how the topological properties of a system change if local disorder is present.

After this, we discussed the requirements a system has to have for the 1D QC marker to be able to correctly predict the topological index of the system. Here we demonstrated that as long as the system is continuous in time, such that the adiabatic approximation can be applied to the Hamiltonian, the adiabatic evolution operator can be used to correctly evolve the system in time and therefore the 1D QC marker can be used to correctly predict the topological structure of the system. This is not the case for quasicrystal systems like the Fibonacci chain where the Hamiltonian instantaneously changes at some point across the time period. It was also pointed out that if the true time evolution operator is known then this can be used in place of the adiabatic evolution operator and one does not have to worry about adiabaticity.

Next, we used M_{QC} to investigate the topological structure of the Rice-Mele model when the Thue-Morse and the Period-doubling sequences were applied. These sequences are aperiodic but not quasiperiodic in nature [81, 47]. We showed that these aperiodic sequences can produce topological structures when applied the RM QC model. We also observed that the characteristic envelope of the change in M_{QC} for increasing $N_{\mathscr{R}}$ was also present for these aperiodic sequence.

Finally, we demonstrated that $M_{QC}(x,t)$ is equal to global the polarisation of a system whether it be periodic, aperiodic or even topological in nature.

It is important to highlight that while throughout this work we have used the quasicrystal marker for systems with open boundary conditions it can also be used on systems with periodic boundary conditions as long as it is evaluated away from the region where the position operator, $\hat{x}$, is discontinuous. The point at which the position operator is discontinuous can be viewed as a "branch cut" to be placed at a convenient point.

9

Noble mean sequences and the Aubry-André model

It was previously shown by Y. Kraus and O. Zilberberg that the Aubry-André model with $b = 1/\tau$, where $\tau = (1 + \sqrt{5})/2$ is the golden ratio, has the same topological structure as the Fibonacci quasicrystal chain [50]. However, this paper showed on a more fundamental level that any sequence that can be generated by eq. (8.13), and subsequently eq. (8.14), has the same topological structure as the Aubry-André model with the same value of τ. In this chapter we will show that one can investigate the silver mean chain or the bronze mean chain or in fact any noble mean chain by investigating the Aubry-André model with a specific value of b. We will present an equation allowing one to determine the value of b for any noble mean chain later.

The Fibonacci chain Hamiltonian was stated earlier in eq. (8.12) but we will restate it here for convenience

$$\hat{H}_{FC} = \sum_n \Big[\big(t_b + V_n^F (t_a - t_b)\big) \left|n+1\right\rangle \left\langle n\right| + \big(\epsilon_b + V_n^F (\epsilon_a - \epsilon_b)\big) \left|n\right\rangle \left\langle n\right| \Big]. \tag{9.1}$$

Above V_n^F represents the nth value of the Fibonacci sequence when it has been converted to its binary

form using eq. (8.9). We also recall that the nth value of the Fibonacci sequence can be generated by

$$V_n^F = 2\Big(\lfloor (n+2)/\tau \rfloor - \lfloor (n+1)/\tau \rfloor\Big) - 1 \tag{9.2}$$

when the value of τ is equal to the golden ratio. The values produced by the above equation are either 1 or -1 but can be converted to binary values by adding 1 and then dividing by 2. Note that when comparing it to the Fibonacci sequence generated by the substitution rules $g(A) = AB$ and $g(B) = B$ and the initial condition $S_0 = A$, $n = 0$ gives the first value of this sequence and $n = 1$ gives the second value and so on. It was shown in [50] that the topological structure of this Hamiltonian with τ set to the golden ratio is equivalent to topological structure of the Aubry-André model with the parameter b set to one over the golden ratio. It was also shown that any sequence generated by V_n^F can be described by the Aubry-André model with the corresponding value of b. This then means that the topological structure of the Fibonacci like Hamiltonians can be investigated with relative ease by considering the corresponding topological structure of the AA model. It is then interesting to ask what other known sequences can be generated by eq. (9.2).

It can be shown that the golden ratio is related to the Fibonacci chain in the following way [82]

$$\lim_{n\to\infty} \frac{F_n}{F_{n-1}} = \lim_{n\to\infty} \frac{N_A(S_n)}{N_B(S_n)} = \tau \tag{9.3}$$

where F_n is the length of the Fibonacci sequence S_n which is generated using the substitution rules $g(A) = AB$ and $g(B) = B$ and the initial condition $S_0 = A$. $N_A(S_n)$ represents the number of A's in the sequence and $N_B(S_n)$ represents the number of B's in the sequence. This then shows that the value of b is equal to the ratio $N_B(S_n)/N_A(S_n)$ for the Fibonacci chain.

From this one could ask whether the silver mean sequence can be generated by eq. (9.2) when τ is set to the silver mean ratio $1 + \sqrt{2}$, seen as $N_A(S_n)/N_B(S_n)$ for the silver mean sequence tends to the silver mean ratio in the limit n goes to infinity. This is not implausible because the substitution rules for the silver mean sequence and the Fibonacci sequence are similar and both are actually part of a larger family of sequences known as the noble mean sequences. We will now show directly, however, that this is not the case. The third generation of the silver mean sequence in its binary form is given by

$$\mathcal{S}_3 = 1, 1, 0, 1, 1, 0, 1, 1, 1, 0, 1, 1, 0, 1, 1, 1, 0 \tag{9.4}$$

and the binary sequence of the same length generated by eq. (9.2) using $\tau = 1 + \sqrt{2}$ is given by

$$\mathcal{V}_F = 0, 1, 0, 1, 0, 0, 1, 0, 1, 0, 0, 1, 0, 1, 0, 1, 0. \tag{9.5}$$

From this it is evident that eq. (9.2) does not generate the silver mean sequence when τ is set to the silver mean ratio. We then ask whether there is a special property the golden ratio possesses that may highlight why eq. (9.2) works for the Fibonacci sequence but not the the silver mean sequence.

The golden ratio has an interesting property that $\tau = 1 + 1/\tau$. We show this relation is true below;

$$\begin{aligned} 1 + \frac{2}{1+\sqrt{5}} &= \frac{3+\sqrt{5}}{1+\sqrt{5}} \\ &= \frac{(3+\sqrt{5})(1-\sqrt{5})}{-4} \\ &= \frac{5+2\sqrt{5}-3}{4} \\ &= \frac{1+\sqrt{5}}{2}. \end{aligned} \tag{9.6}$$

With the above identity we then ask whether replacing $1/\tau$ with $1/(1+1/\tau)$ in eq. (9.2) would allow us to generate both the Fibonacci sequence and the silver mean sequence. To test this theory we define a new sequence generator V_n^{NM} as

$$V_n^{NM} = 2\Bigg(\left\lfloor (n+2)\Big(\frac{1}{1+1/\tau}\Big) \right\rfloor - \left\lfloor (n+1)\Big(\frac{1}{1+1/\tau}\Big) \right\rfloor \Bigg) - 1 \tag{9.7}$$

where τ is given by eq. (9.3). We then set τ to the silver mean ratio, $\tau = 1+\sqrt{2}$, in eq. (9.7) and find that it generates the following sequence

$$\mathcal{V}_S = 1,1,0,1,1,0,1,1,1,0,1,1,0,1,1,1,0. \tag{9.8}$$

Comparing this to eq. (9.4) we see that V_n^{NM} does indeed generate the silver mean sequence when τ is defined by eq. (9.3). With this we have shown that eq. (9.7) can be used to generate both the silver mean sequence and the Fibonacci sequence when the value of τ is determined by eq. (9.3). Because of this we now define a new Hamiltonian, which we call the noble mean Hamiltonian, in the following way

$$\hat{H}_{NM} = \sum_n \Big[\big(t_b + V_n^{NM}(t_a - t_b)\big) \left|n+1\right\rangle \left\langle n\right| + \big(\epsilon_b + V_n^{NM}(\epsilon_a - \epsilon_b)\big) \left|n\right\rangle \left\langle n\right| \Big] \tag{9.9}$$

where V_n^{NM} is defined in eq. (9.7). This Hamiltonian is equivalent to the Fibonacci chain Hamiltonian when τ is set to the golden ratio. When $\tau = 1+\sqrt{2}$ this Hamiltonian defines the silver mean chain Hamiltonian. From the findings in [50], this then means that one can analyse the topological structure of the silver mean chain Hamiltonian by analysing the Aubry-André model with $b = 1/(1+1/\tau)$ where $\tau = 1+\sqrt{2}$.

To visualise the topological equivalence between the Aubry-Andre model and the silver mean chain

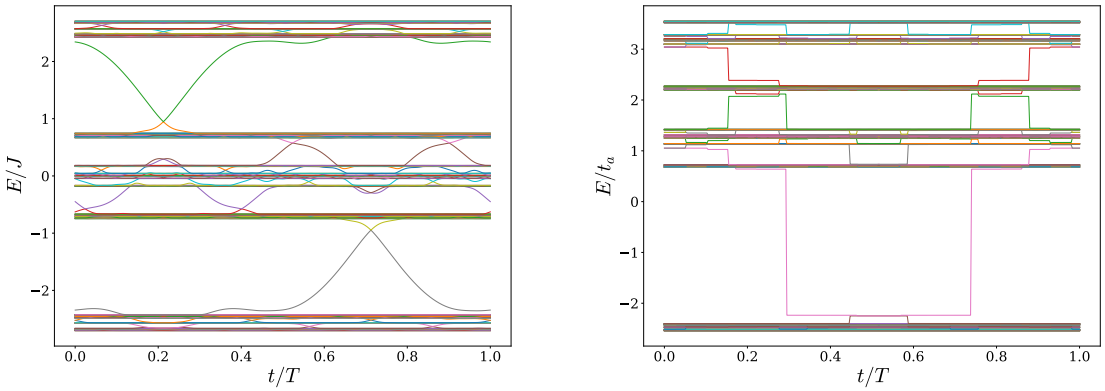

(a) (b)

Figure 9.1: Figures highlighting the topological equivalence of the Aubry-André model and the silver mean chain. (a) The energy spectrum for the Aubry-André model with $b = 1/(1+1/\tau)$, where τ is equal to $1+\sqrt{2}$, and $\Delta/J = -2$. (b) The energy spectrum for the silver mean chain with $t_b/t_a = 1, \epsilon_a/t_a = 2$ and $\epsilon_b/t_a = -2$.

we plot the energy spectrum of both models in fig. 9.1. Figure 9.1a shows the energy spectrum for the Aubry-André model with $b = 1/(1+1/\tau)$ with $\tau = 1+\sqrt{2}$ which is the silver mean ratio. Figure 9.1b shows the energy spectrum of the silver mean chain with the parameters $t_b/t_a = 1$, $\epsilon_a/t_a = 2$ and $\epsilon_b/t_a = -2$. To generate this figure we used the fact that V_n^{NM} is equivalent to

$$\chi_n = sign\Big[\cos(2\pi b(n+1) + \pi b + \phi) - \cos(\pi b)\Big] \tag{9.10}$$

when $b = 1/(1+1/\tau)$ and $\phi = 0$. Using this and setting $\phi = 2\pi t/T$ then allows us to plot the energy spectrum against time as we do in the AA energy spectrum. From these figures one can see that the structure of each energy diagram is similar and they both possess the same amount of reasonably sized gaps. As well as this, it can be noticed that the number of edge modes crossing each of these reasonably sized gaps are equivalent. For example in fig. 9.1a we see that there is one edge mode crossing in the gap around $E/J = -1.5$; it can be seen that the number of edge mode crossings in the gap at $E/\epsilon_a = -1$ in fig. 9.1b is also one. It can be shown definitively that these gaps are topologically equivalent by considering the following Hamiltonian which is a continuous deformation between the Aubry-André model and the silver mean sequence shown in fig. 9.1;

$$H^S(t,\beta) = \sum_n \left(t\,|n+1\rangle\langle n| + \lambda \frac{\tanh\big(\beta[\cos(2\pi bn+\phi) - \cos(\pi b)]\big)}{\tanh(\beta)}\,|n\rangle\langle n| \right). \tag{9.11}$$

Above $b = 1/(1+1/\tau)$ with $\tau = 1+\sqrt{2}$ and β is the deformation parameter. In the limit $\beta \to 0$ H^S becomes the Aubry-André model plus some constant energy shift and in the limit $\beta \to \infty$ H^S

becomes the silver mean chain [50]. It can be shown that the gap at $E/J = -1.5$ in the AA model never closes as the parameter β is continuously increased to ∞ and deforms into the gap seen at at $E/t_a = -1$ in the silver mean chain. Because this gap never closes as β is varied the topological index cannot change and therefore these two gaps are topologically equivalent. With this we have confirmed that the topological index of an energy gap in the silver mean chain Hamiltonian can be determined by the topological index of a gap in the Aubry-André model Hamiltonian as long as this gap does not close when varying the the parameter β in eq. (9.11).

While we showed above that the topological structure of the AA model can be used to determine the topological structure of the silver mean chain we can actually generalise this further and show that the AA model can be used to determine the topological structure of any noble mean chain. To show this we first define the noble mean sequences via the generating rules

$$\begin{aligned} g(A) &= A^p B \\ g(B) &= A \end{aligned} \tag{9.12}$$

with the initial value of the sequence set to A. The value p is an integer that determines which noble mean sequence is being considered; $p = 1$ gives the Fibonacci sequence, $p = 2$ gives the silver mean sequence, $p = 3$ gives the bronze mean sequence and so on. It is known that the ratio of N_A/N_B for the noble mean sequences is given by [47]

$$\lim_{n\to\infty} \frac{N_A(S_n)}{N_B(S_n)} = \frac{1}{2}\big(p + \sqrt{p^2+4}\big). \tag{9.13}$$

With this one can then use V_n^{NM} to generate any noble mean sequence. To demonstrate this we consider the bronze mean sequence and compare it to the sequence generated by V_n^{NM} with τ set by eq. (9.13) and $p = 3$. The third generation of the bronze mean sequence is given by

$$\mathcal{B}_2 = 1,1,1,0,1,1,1,0,1,1,1,0,1,1,1,1,0,1,1,1,0,1,1,1,0,1,1,1,1,0,1,1,1,1,0,1,1,1,0,1,1,1,0,1,1,1,1,0. \tag{9.14}$$

Using eq. (9.13) we see that $\tau = (3+\sqrt{13})/2$ which is known as the bronze mean ratio. Using this in eq. (9.7) we generate the following sequence

$$\mathcal{V}_B = 1,1,1,0,1,1,1,0,1,1,1,0,1,1,1,1,0,1,1,1,0,1,1,1,0,1,1,1,1,0,1,1,1,1,0,1,1,1,0,1,1,1,0,1,1,1,1,0 \tag{9.15}$$

where we set the length of the sequence to match $\mathcal{B}_2$. It can be seen that these two sequences are equivalent. This then demonstrates that any noble mean sequence can be generated by eq. (9.7) when the value of τ is determined by eq. (9.13). With this we also confirm that the topological structure

of any noble mean chain, defined by $\hat{H}_{NM}$ given in eq. (9.9), can be determined by the topological structure of the Aubry-André model with

$$b = \frac{1}{1 + \frac{2}{p+\sqrt{p^2+4}}}. \tag{9.16}$$

10

Conclusion and Discussion

Within this final chapter we summarise the major findings presented within this thesis and explore possible new avenues of research that they could generate.

In chapter 4 the usefulness of the Chern marker for 2D systems was demonstrated by using it to display the topological structure of the Hofstadter butterfly for the Harper-Hofstadter model. In this chapter we also defined a 4D version of this topological marker which will allow the topological structure of a 4D system to be investigated more thoroughly. One potential hurdle in the topological investigation of 4D systems is the size of the Hamiltonians needed such that the 4D topological marker gives an accurate prediction of the topological index of the system. It was shown in chapter 8 that the 2D Chern marker has to be measured 5 unit cells away from the edge of the system in each direction. As such, the system needed to have 81 unit cells or more for the Chern marker to give an accurate representation of the systems topological structure. Assuming this rule also applies to 4D models one would have to consider a system with 6561 unit cells each with more than one lattice site within it. Form this one can see that very large matrices have to be diagonalized, as well as multiplied numerous times, to calculate the 4D topological marker. Whilst this hurdle may seem slightly daunting it may not be as large as initially thought due to recent advancements in parallel computing and the use of graphics cards for matrix multiplication.

Chapter 5 compared the Bott index to the Chern number and showed that these two objects are equivalent in both the discrete and the continuous regime. The local Bott index was also compared to the Chern marker and was found to be equivalent when system of reasonable size were considered.

Chapter 6 introduced the 1D marker for one dimensional time-dependent systems which is one of the main findings within this thesis. The accuracy of this marker was confirmed numerically and it was shown that the time evolution of the marker was equivalent to that of the Wannier centre evolution showing also that the 1D marker gives the change in the polarisation of the system. Because the 1D marker does not require translational invariance it was then used to investigate a system with random disorder applied throughout; the analysis was averaged over 100 random disorder matrices. It was found that the topological structure of the system changed only when some of the disorder matrices started to close the band gap, allowing the topological structure to change for that specific disorder matrix. This agrees with previous studies of how disorder affects the topological structure of a system [42]. The affect of a point defect on the topological structure was also investigated; this investigation is only possible with local topological markers. In this case it was found that the point defect only affected the topological structure close to the defect and far from the defect the topological structure remained unaffected. This finding is interesting as it suggests that topological pumping may still exist when point defects are present. This is because far from the defect the topological index is non-zero suggesting that topological pumping persists to the left and right of the defect but not at the defect. Because of this pumping it may be that a potential difference is created across the defect and increases until it is great enough that the current can surmount the energy step created by the defect and thus topological pumping through the system is restored. It would be interesting to analyse this experimentally either with photonic systems or cold atomic gas systems. The investigation of point defects within topological systems is important not only to the understanding of topological materials but also to their application to engineering systems. This is due to the fact that point defects can easily arise when creating these systems and therefore understanding how they affect the desired properties of topological materials is crucial. Here we investigated a single point defect, however, it would also be interesting to see how the topological structure of the system, along with the current through the system, is affected by two point defects and the separation between them. As well as this, the 1D marker could be used to better understand how disorder eventually destroys the topological structure of the system and whether certain configurations of disorder can destroy the topological structure with less point defects. The topological phase transitions of the generalised Aubry-André model were also investigated within this chapter with the parameter b set to $1/3$. We showed that when the fixed hopping strength, J, is set to one the topological structure of the system is generally stable when the parameters of the system are varied. However, when $J = 0$ so that the hopping term is determined solely by the modulating hopping strength the system displays a wide array of topological phase transitions as the parameters of the system are varied. It was seen that when only the bottom band of the system is populated phase transitions between different non-trivial topological regimes were observed, but when the bottom two bands of the system were populated phase transitions

between topological and non-topological regimes also existed. For the specific case of $T_2/T_1 = 2$ it was seen that when the ratio of the hopping modulation and the onsite modulation was varied the system underwent a phase transition between the topological index being zero and the topological index being -2. This phase transition is potentially very useful as it could form the basis for a topological pumping switch. More interestingly, when T_2/T_1 was set to 6 the system possessed three topological phases; one with a positive topological index of 4, one with a topological index of 0, and one with a negative topological index of -2. This regime provides even more control of the pumping through the system allowing both forwards and backwards pumping along with no pumping at all. It is important to point out, however, that the positive topological phase has a narrow band gap and is therefore susceptible to disorder. It is clear that both these cases could prove very useful when using topological materials to control pumping behaviour. Here we only investigated the generalised Aubry-André model with $b = 1/3$; it would therefore be interesting to analyse the phase diagrams of the generalised Aubry-André model with other values of b, say $1/5$ or $1/7$, and see if further interesting phase transitions are present. Another interesting point is that when the system under went a phase transition and the bands touched, therefore making the system a semi-metal, the change in the 1D marker was no longer quantized to an integer value but was still nonzero. This suggests that some of the current through the system in this case would be caused by the topological structure of the system with the other part of the current being due to the excitations around this band touching. While it is most likely that the current due to the topological structure of the system will be much less than that due to excitations it is still interesting to ask what the ratio between the different contributions would be. This could be one possible future direction of study. It was stated earlier that the generalised Aubry-André model was first proposed in [86]. In the supplementary material of this paper an experimental setup was suggested using photonic wave guides where the hopping strength of the system was determined by the spacing between the wave guides. As such, a experimental setup using photonic wave guides could be used to analyse the phase transitions seen in the generalised Aubry-André model when $J = 0$. As well as this, by stacking wave guides with different parameters on top of each other one could potentially generate a topological photonic switch that could control the flow of photons through a system.

In chapter 7 we defined the 3D marker which is another major finding of this thesis. It was shown analytically that the change in the 3D marker over a full time period gave the second Chern number of the system which is the topological index associated with 3D time-dependent and 4D systems. It was also shown analytically that the 3D marker is equivalent to the change in the Chern-Simons axion coupling which has been linked to the magnetoelectric polarisation of a system [26, 25]. It was then confirmed numerically that the 3D marker gives the second Chern number of a system by considering a 3D time-dependent Hamiltonian with known second Chern number. Whilst carrying out this numerical investigation it was apparent that a major obstacle to investigating 3D time-dependent

topological systems is the size of the matrices one has to manipulate. For example, here we did not investigate how a point defect would affect the topological structure of the system. This is because to do this it would be best to consider a 30 unit cell by 30 unit cell by 30 unit cell system with 9 lattice points per unit cell. Therefore we would be dealing with matrices of size 243000×243000 not to mention we would have to do this for each time step. Therefore, it is evident that computational restrictions prevent the full use of the 3D marker for the moment but one hopes that these problems will be surmountable in the near future allowing us to unlock the full potential of the 3D marker. These computational advances could also allow the investigation of 3D quasicrystals and the 3D marker could be used to investigate these systems once the same adaptations that were made to the 1D marker in chapter 9 were applied to the 3D marker. One avenue of further investigation that could be carried out without this advancement, however, is the use of the 3D marker on a topological Hamiltonian that is not formed from a tensor product. As well as this, despite showing that the Chern-Simons axion coupling is the thing that is progressively changing over time it was still not confirmed what this object relates to when there is no electric or magnetic field applied to the system. It is therefore evident that this area needs further investigation to determine what property of the system is changing over time and what object, if any, is being pumped through the system.

Within chapter 8 we adapted the 1D marker introduced in chapter 6 so that it could be applied to systems with aperiodic structure as well as to systems with periodic structure. This result is the final major finding of this thesis. We then used the Aubry-Andre model to confirm that this object can correctly determine the topological structure of both periodic and aperiodic 1D time-dependent systems. It was found that the 1D quasicrystal marker does indeed correctly determine the topological structure of these systems, however, for quasicrystal systems the topological marker needs to be evaluated over a larger area of the system, compared to the periodic case, to determine the topological structure accurately. As well as this, it was found that the 1D quasicrystal marker tended to the topological index of the system when the region considered was increased. The upper bound on the error of the 1D quasicrystal marker displayed a decay profile which was approximately the same for both the periodic case and the quasicrystal case. It was also seen that this decay profile changed for different topological values. After this, the 1D quasicrystal marker was used to investigate the topological structure of the Rice-Mele quasicrystal model with the silver mean sequence applied and it was found that this system is topological in nature. As well as this, the same decay profile for the approximate upper bound of the 1D quasicrystal marker seen for the Aubry-André model was also seen for this model suggesting that the decay profile is present for all models. The topological structure of the system was then confirmed by analysing the current through the system as well as analysing the evolution of the Wannier centres of the system. This then showed that the 1D quasicrystal marker can be used to determine the topological index of quasicrystal systems that could not previously be

investigated using traditional methods. It was also demonstrated that the 1D quasicrystal marker can be used to investigate the topological structure of a local region within the system and determine the effects a local defect has on its topological structure, although the size of the regions considered have to be considerably larger than in the periodic case. Despite the fact that the size of the regions needs to be large, the 1D quasicrystal marker could still prove very useful when investigating how disorder and local defects affect the topological pumping through quasicrystal systems. It would be interesting to investigate the disorder in quasicrystal systems further and compare the effects to those seen in periodic systems to see if any differences arise. The requirements a system needs for the 1D quasicrystal marker to accurately predict the topological structure of the system were then discussed. It was highlighted that if the adiabatic evolution operator is used then the system has to be continuous in time such that the adiabatic approximation holds, but if the true time-dependent operator is known one can use this in the 1D quasicrystal marker and not worry about the conditions of the adiabatic approximation. Following this, the topological structure of the Rice-Mele model with the Thue-Morse sequence and the Period-doubling sequence applied was investigated. These sequences are aperiodic sequences but are not quasiperiodic in nature. It was confirmed that these system can possess a topological nature and therefore can exhibit quantized pumping. It was also seen that the approximate upper bound on the error of the 1D quasicrystal marker exhibited a decay profile similar to that seen in previous models, however, its dependence on the value of the topological index was slightly different to that seen in the previous models. Comparing the approximate upper bound on the errors from the models studied we concluded that $C_r/N_{\mathscr{R}}$ can be used to give a rough estimate of the error of the 1D quasicrystal marker for a given system size. It would be interesting to investigate the error of the 1D marker analytically to try to determine how the upper bound on the error varies for different models and what properties of the Hamiltonian determine this variation. Lastly, the evolution of the polarisation for a quasicrystal system was calculated and compared to the evolution of the 1D quasicrystal marker. It was found that the evolution of the 1D quasicrystal marker matched that of the polarisation when the discontinuous jump in the polarisation was neglected. This then confirmed that the relationship between the 1D marker and the polarisation of the system is present in quasicrystal systems also. This shows that the 1D marker and the 1D quasicrystal marker are useful not just for topological system but also for systems in general where it is important to know the polarisation of the system. A natural next step from this is to compare the polarisation of other non-topological systems with the results measure using the 1D marker for that system. A this stage it is important to point out that a time-dependent version of the Bott index exists for 1D systems and has been used to determine both the polarisation and the topological index of a quasicrystal system [51]. Its form differs from that of the 1D quasicrystal in a few ways, one of which is that it does not use the adiabatic evolution operator to evolve the states and only uses the projectors at different snapshots in time. Therefore,

one future direction of study could compare the time-dependent Bott index with the local marker both analytically and numerically. It would also be useful to investigate the difference in the time taken to calculate these objects. Another natural next step using the 1D marker would be to try and answer the question 'how big does a quasicrystal system have to be to show topological behaviour?'. This is an interesting question seen as it was shown that the 1D quasicrystal marker is not quantized for systems of size 30 lattice sites or less. This would also naturally raise the question of how long a quasi crystal system has to be. Let us for example consider the silver mean sequence. It is obvious that the first generation of this sequence, which has a length of 3, is not long enough to be a quasicrystal seen as no repeating structure can be seen, nor is the second generation long enough, but can the third generation be classed as a quasicrystal seen as repeating structure can be seen in these generations? One other area of future study could see the 1D marker used to analyse the change in the polarisation of metallic aperiodic systems. It is known that the majority of the current that arises in normal metallic system is due to excited states, but a small contribution can also come from the change in the polarisation of the system; however small it may be. Something similar has previously been investigated for 2D metallic systems using the Chern marker [41]. It would also be interesting to see how this contribution to the current differs for quasicrystal systems compared to the periodic case. finally, it is worth pointing out that we only considered the Rice-Mele quasicrystal model with modulating potentials that have the same time period. From the analysis done on the generalised Aubry-André model in chapter 6 it is clear that letting the time periods of each modulating potential differ would change the structure of the system. This could potentially give rise to exotic phase transitions within 1D quasicrystal systems.

Finally, within chapter 9 it was shown that the Aubry-André model can possess the same topological structure as other quasiperiodic noble mean chains apart from the Fibonacci chain. This is achieved by setting the parameter b to a specific value which is determined by eq. (9.16). This will allow future studies into different quasicrystal systems and increase the over all understanding of the interplay between topological structure and quasicrystal structure. One aspect that could be investigated further using the noble mean sequences is the question 'what is the lowest ratio of A's to B's a system needs to show topological properties?'. The noble mean sequences are ideally suited to study this seen as one just needs to increase the value of p in eq. (9.12) for a set system size and use the 1D quasicrystal marker to measure the topology of the system. This has potential benefits when trying to engineer a topological system seen as the A's within the system represent one type of particle and the B's represent another. Therefore, if the topological system has to be engineered in some way, say for instance using a doping technique, the higher the ratio of A's to B's within the system the less doping is required.

It is evident that the field of topological physics is still rapidly growing and we hope that the results found in this thesis contribute to this growth as well as inspire future areas of investigation.

A

Relation between $\hat{\mathcal{A}}_i$ and $\hat{\mathcal{F}}_{ij}$

Within this appendix we prove the identity

$$\hat{\mathcal{U}}^\dagger \hat{\mathcal{F}}_{ij} \hat{\mathcal{U}} = \hat{\tilde{\mathcal{P}}}\Big(\partial_i \hat{\mathcal{A}}_j - \partial_j \hat{\mathcal{A}}_i - i[\hat{\mathcal{A}}_i, \hat{\mathcal{A}}_j]\Big)\hat{\tilde{\mathcal{P}}} + \hat{\tilde{\mathcal{F}}}_{ij} \tag{A.1}$$

which was stated in eq. (7.29) and $\hat{\mathcal{P}}$, $\hat{\mathcal{U}}$ and $\hat{\mathcal{A}}_i$ are defined as in Section 6.2.

To show this we analyse the left hand side of the above equation and expand it so that we gain the right hand side of the equation. In eq. (7.13) we defined $\hat{\mathcal{F}}_{ij}$ as

$$\hat{\mathcal{F}}_{ij} = i\,\hat{\mathcal{P}}\Big[\partial_i \hat{\mathcal{P}}, \partial_j \hat{\mathcal{P}}\Big]\hat{\mathcal{P}} \tag{A.2}$$

where the square brackets denote the commutator and $\hat{\mathcal{P}}$ is the translationally invariant part of the projector $\hat{P}$. The derivatives are defined as $\partial_i = \partial_{k_i}$. If we use the relation $\hat{\mathcal{P}} = \hat{\mathcal{U}}\hat{\tilde{\mathcal{P}}}\hat{\mathcal{U}}^\dagger$, given in eq. (6.7), we get that

$$\hat{\mathcal{U}}^\dagger \hat{\mathcal{F}}_{ij} \hat{\mathcal{U}} = i\Big(\hat{\tilde{\mathcal{P}}}\hat{\mathcal{U}}^\dagger(\partial_i \hat{\mathcal{P}})(\partial_j \hat{\mathcal{P}})\hat{\mathcal{U}}\hat{\tilde{\mathcal{P}}} - \hat{\tilde{\mathcal{P}}}\hat{\mathcal{U}}^\dagger(\partial_j \hat{\mathcal{P}})(\partial_i \hat{\mathcal{P}})\hat{\mathcal{U}}\hat{\tilde{\mathcal{P}}}\Big) \tag{A.3}$$

One can also derive the following identities

$$\hat{\mathcal{U}}^\dagger(\partial_i\hat{\mathcal{P}}) = (\partial_i\hat{\bar{\mathcal{P}}})\hat{\mathcal{U}}^\dagger + \hat{\bar{\mathcal{P}}}(\partial_i\hat{\mathcal{U}}^\dagger) - (\partial_i\hat{\mathcal{U}}^\dagger)\hat{\mathcal{P}} \tag{A.4}$$

$$(\partial_i\hat{\mathcal{P}})\hat{\mathcal{U}} = (\partial_i\hat{\mathcal{U}})\hat{\bar{\mathcal{P}}} + \hat{\mathcal{U}}(\partial_i\hat{\bar{\mathcal{P}}}) - \hat{\mathcal{P}}(\partial_i\hat{\mathcal{U}}). \tag{A.5}$$

If we use the above identities to evaluate the first term in eq. (A.3) we get that

$$\begin{aligned}\hat{\bar{\mathcal{P}}}\hat{\mathcal{U}}^\dagger(\partial_i\hat{\mathcal{P}})(\partial_j\hat{\mathcal{P}})\hat{\mathcal{U}}\hat{\bar{\mathcal{P}}} = \hat{\bar{\mathcal{P}}}(\partial_i\hat{\mathcal{U}}^\dagger)(\partial_j\hat{\mathcal{U}})\hat{\bar{\mathcal{P}}} + \hat{\bar{\mathcal{P}}}(\partial_i\hat{\mathcal{U}}^\dagger)\hat{\mathcal{U}}(\partial_j\hat{\bar{\mathcal{P}}})\hat{\bar{\mathcal{P}}} + \hat{\bar{\mathcal{P}}}(\partial_i\hat{\bar{\mathcal{P}}})\hat{\mathcal{U}}^\dagger(\partial_j\hat{\mathcal{U}})\hat{\bar{\mathcal{P}}} \\ -\hat{\bar{\mathcal{P}}}(\partial_i\hat{\mathcal{U}}^\dagger)\hat{\mathcal{P}}(\partial_j\hat{\mathcal{U}})\hat{\bar{\mathcal{P}}} + \hat{\bar{\mathcal{P}}}(\partial_i\hat{\bar{\mathcal{P}}})(\partial_j\hat{\bar{\mathcal{P}}})\hat{\bar{\mathcal{P}}}.\end{aligned} \tag{A.6}$$

The second term in equation eq. (A.3) is identical to the first but with the labels on the derivative switched. As such, the above equation can be used to expand eq. (A.3).

We now condense these terms such that we get the right hand side of eq. (A.1). To do this we first show that

$$\begin{aligned}\hat{\bar{\mathcal{P}}}\partial_i\hat{\mathcal{A}}_j\hat{\bar{\mathcal{P}}} = i\hat{\bar{\mathcal{P}}}\partial_i\Big(\hat{\bar{\mathcal{P}}}\hat{\mathcal{U}}^\dagger(\partial_j\hat{\mathcal{U}})\hat{\bar{\mathcal{P}}}\Big)\hat{\bar{\mathcal{P}}} = i\Big(\hat{\bar{\mathcal{P}}}(\partial_i\hat{\bar{\mathcal{P}}})\hat{\mathcal{U}}^\dagger(\partial_j\hat{\mathcal{U}})\hat{\bar{\mathcal{P}}} + \hat{\bar{\mathcal{P}}}(\partial_i\hat{\mathcal{U}}^\dagger)(\partial_j\hat{\mathcal{U}})\hat{\bar{\mathcal{P}}} - \hat{\bar{\mathcal{P}}}(\partial_j\hat{\mathcal{U}}^\dagger)\hat{\mathcal{U}}(\partial_i\hat{\bar{\mathcal{P}}})\hat{\bar{\mathcal{P}}} \\ +\hat{\bar{\mathcal{P}}}\hat{\mathcal{U}}^\dagger(\partial_i\partial_j\hat{\mathcal{U}})\hat{\bar{\mathcal{P}}}\Big),\end{aligned} \tag{A.7}$$

where in the first equality we used the definition of $\hat{\mathcal{A}}_i$ given in eq. (6.19) and in the second equality we have used $\hat{\mathcal{U}}^\dagger(\partial_j\hat{\mathcal{U}}) = -(\partial_j\hat{\mathcal{U}}^\dagger)\hat{\mathcal{U}}$. Comparing the first three terms of the above equation with the first three terms in eq. (A.6) we see that they are the same. If we use eq. (A.7) along with eq. (A.6) to analyse eq. (A.3) we find that

$$\hat{\mathcal{U}}^\dagger\hat{\mathcal{F}}_{ij}\hat{\mathcal{U}} = \hat{\bar{\mathcal{P}}}\Big(\partial_i\hat{\mathcal{A}}_j - \partial_j\hat{\mathcal{A}}_i\Big)\hat{\bar{\mathcal{P}}} - i\,\hat{\bar{\mathcal{P}}}(\partial_i\hat{\mathcal{U}}^\dagger)\hat{\mathcal{P}}(\partial_j\hat{\mathcal{U}})\hat{\bar{\mathcal{P}}} + i\,\hat{\bar{\mathcal{P}}}(\partial_j\hat{\mathcal{U}}^\dagger)\hat{\mathcal{P}}(\partial_i\hat{\mathcal{U}})\hat{\bar{\mathcal{P}}} + i\,\hat{\bar{\mathcal{P}}}\big[\partial_i\hat{\bar{\mathcal{P}}}, \partial_j\hat{\bar{\mathcal{P}}}\big]\hat{\bar{\mathcal{P}}}. \tag{A.8}$$

Next we analyse $\hat{\mathcal{A}}_i\hat{\mathcal{A}}_j$ and find that

$$\hat{\mathcal{A}}_i\hat{\mathcal{A}}_j = -\hat{\bar{\mathcal{P}}}\hat{\mathcal{U}}^\dagger(\partial_i\hat{\mathcal{U}})\hat{\bar{\mathcal{P}}}\hat{\mathcal{U}}^\dagger(\partial_j\hat{\mathcal{U}})\hat{\bar{\mathcal{P}}} = \hat{\bar{\mathcal{P}}}(\partial_i\hat{\mathcal{U}}^\dagger)\hat{\mathcal{P}}(\partial_j\hat{\mathcal{U}})\hat{\bar{\mathcal{P}}} \tag{A.9}$$

where in the last equality we used $\hat{\mathcal{U}}^\dagger(\partial_j\hat{\mathcal{U}}) = -(\partial_j\hat{\mathcal{U}}^\dagger)\hat{\mathcal{U}}$ as well as $\hat{\mathcal{P}} = \hat{\mathcal{U}}\hat{\bar{\mathcal{P}}}\hat{\mathcal{U}}^\dagger$. Using this in eq. (A.8) we see that

$$\hat{\mathcal{U}}^\dagger\hat{\mathcal{F}}_{ij}\hat{\mathcal{U}} = \hat{\bar{\mathcal{P}}}\Big(\partial_i\hat{\mathcal{A}}_j - \partial_j\hat{\mathcal{A}}_i - i\Big[\hat{\mathcal{A}}_i, \hat{\mathcal{A}}_j\Big]\Big)\hat{\bar{\mathcal{P}}} + i\,\hat{\bar{\mathcal{P}}}\big[\partial_i\hat{\bar{\mathcal{P}}}, \partial_j\hat{\bar{\mathcal{P}}}\big]\hat{\bar{\mathcal{P}}}. \tag{A.10}$$

For the final part of the proof we use the definition $\hat{\bar{F}}_{ij} = i\,\hat{\bar{\mathcal{P}}}\Big[\partial_i\hat{\bar{\mathcal{P}}}, \partial_j\hat{\bar{\mathcal{P}}}\Big]\hat{\bar{\mathcal{P}}}$ and get

$$\hat{\mathcal{U}}^\dagger\hat{\mathcal{F}}_{ij}\hat{\mathcal{U}} = \hat{\bar{\mathcal{P}}}\Big(\partial_i\hat{\mathcal{A}}_j - \partial_j\hat{\mathcal{A}}_i - i[\hat{\mathcal{A}}_i, \hat{\mathcal{A}}_j]\Big)\hat{\bar{\mathcal{P}}} + \hat{\bar{\mathcal{F}}}_{ij}. \tag{A.11}$$

We have thus proven the identity stated in eq. (7.29) in the main text.

Bibliography

[1] N. Cooper, J. Dalibard, and I. Spielman, "Topological bands for ultracold atoms," *Reviews of modern physics*, vol. 91, no. 1, p. 015005, 2019.

[2] P. W. Anderson, "More is different," *Science*, vol. 177, no. 4047, pp. 393–396, 1972.

[3] P. W. Anderson, *Basic notions of condensed matter physics*. CRC Press, 2018.

[4] K. v. Klitzing, G. Dorda, and M. Pepper, "New method for high-accuracy determination of the fine-structure constant based on quantized hall resistance," *Physical review letters*, vol. 45, no. 6, p. 494, 1980.

[5] D. J. Thouless, M. Kohmoto, M. P. Nightingale, and M. den Nijs, "Quantized hall conductance in a two-dimensional periodic potential," *Phys. Rev. Lett.*, vol. 49, pp. 405–408, Aug 1982.

[6] R. B. Laughlin, "Anomalous quantum hall effect: an incompressible quantum fluid with fractionally charged excitations," *Physical Review Letters*, vol. 50, no. 18, p. 1395, 1983.

[7] D. E. Feldman and B. I. Halperin, "Fractional charge and fractional statistics in the quantum hall effects," *Reports on Progress in Physics*, 2021.

[8] D. Tong, "Lectures on the quantum Hall effect," *arXiv:1606.06687*.

[9] D. J. Thouless, M. Kohmoto, M. P. Nightingale, and M. den Nijs, "Quantized Hall conductance in a two-dimensional periodic potential," *Phys. Rev. Lett.*, vol. 49, no. 6, p. 405, 1982.

[10] M. Lohse, C. Schweizer, O. Zilberberg, M. Aidelsburger, and I. Bloch, "A thouless quantum pump with ultracold bosonic atoms in an optical superlattice," *Nat. Phys.*, vol. 12, no. 4, pp. 350–354, 2016.

[11] C. Schweizer, M. Lohse, R. Citro, and I. Bloch, "Spin pumping and measurement of spin currents in optical superlattices," *Phys. Rev. Lett.*, vol. 117, no. 17, p. 170405, 2016.

[12] S. Nakajima, T. Tomita, S. Taie, T. Ichinose, H. Ozawa, L. Wang, M. Troyer, and Y. Takahashi, "Topological thouless pumping of ultracold fermions," *Nat. Phys.*, vol. 12, no. 4, pp. 296–300, 2016.

[13] S. Nakajima, N. Takei, K. Sakuma, Y. Kuno, P. Marra, and Y. Takahashi, "Competition and interplay between topology and quasi-periodic disorder in thouless pumping of ultracold atoms," *Nat. Phys.*, pp. 1–6, 2021.

[14] Y. E. Kraus, Y. Lahini, Z. Ringel, M. Verbin, and O. Zilberberg, "Topological states and adiabatic pumping in quasicrystals," *Phys. Rev. Lett.*, vol. 109, no. 10, p. 106402, 2012.

[15] M. Verbin, O. Zilberberg, Y. Lahini, Y. E. Kraus, and Y. Silberberg, "Topological pumping over a photonic fibonacci quasicrystal," *Phys. Rev. B*, vol. 91, no. 6, p. 064201, 2015.

[16] M. Wimmer, H. M. Price, I. Carusotto, and U. Peschel, "Experimental measurement of the berry curvature from anomalous transport," *Nat. Phys.*, vol. 13, no. 6, pp. 545–550, 2017.

[17] M. I. N. Rosa, R. K. Pal, J. R. F. Arruda, and M. Ruzzene, "Edge states and topological pumping in spatially modulated elastic lattices," *Phys. Rev. Lett.*, vol. 123, no. 3, p. 034301, 2019.

[18] I. H. Grinberg, M. Lin, C. Harris, W. A. Benalcazar, C. W. Peterson, T. L. Hughes, and G. Bahl, "Robust temporal pumping in a magneto-mechanical topological insulator," *Nat. Commun.*, vol. 11, no. 1, pp. 1–9, 2020.

[19] R. Resta, "Theory of the electric polarization in crystals," *Ferroelectrics*, vol. 136, no. 1, pp. 51–55, 1992.

[20] R. King-Smith and D. Vanderbilt, "Theory of polarization of crystalline solids," *Physical Review B*, vol. 47, no. 3, p. 1651, 1993.

[21] G. Ortiz and R. M. Martin, "Macroscopic polarization as a geometric quantum phase: Many-body formulation," *Phys. Rev. B*, vol. 49, no. 20, p. 14202, 1994.

[22] R. Resta, "Quantum-mechanical position operator in extended systems," *Physical Review Letters*, vol. 80, no. 9, p. 1800, 1998.

[23] D. Vanderbilt, *Berry Phases in Electronic Structure Theory: Electric Polarization, Orbital Magnetization and Topological Insulators*. Cambridge University Press, 2018.

[24] X.-L. Qi, T. L. Hughes, and S.-C. Zhang, "Topological field theory of time-reversal invariant insulators," *Physical Review B*, vol. 78, no. 19, p. 195424, 2008.

[25] A. M. Essin, J. E. Moore, and D. Vanderbilt, "Magnetoelectric polarizability and axion electrodynamics in crystalline insulators," *Phys. Rev. Lett.*, vol. 102, no. 14, p. 146805, 2009.

[26] A. Malashevich, I. Souza, S. Coh, and D. Vanderbilt, "Theory of orbital magnetoelectric response," *New J. Phys.*, vol. 12, no. 5, p. 053032, 2010.

[27] Y. E. Kraus, Z. Ringel, and O. Zilberberg, "Four-dimensional quantum hall effect in a two-dimensional quasicrystal," *Phys. rev. letters*, vol. 111, no. 22, p. 226401, 2013.

[28] H. M. Price, O. Zilberberg, T. Ozawa, I. Carusotto, and N. Goldman, "Four-dimensional quantum hall effect with ultracold atoms," *Phys. Rev. Lett.*, vol. 115, no. 19, p. 195303, 2015.

[29] T. Ozawa and H. M. Price, "Topological quantum matter in synthetic dimensions," *Nat. Rev. Phys.*, vol. 1, no. 5, pp. 349–357, 2019.

[30] O. Zilberberg, S. Huang, J. Guglielmon, M. Wang, K. P. Chen, Y. E. Kraus, and M. C. Rechtsman, "Photonic topological boundary pumping as a probe of 4d quantum hall physics," *Nature*, vol. 553, no. 7686, pp. 59–62, 2018.

[31] M. Lohse, C. Schweizer, H. M. Price, O. Zilberberg, and I. Bloch, "Exploring 4d quantum hall physics with a 2d topological charge pump," *Nature*, vol. 553, no. 7686, pp. 55–58, 2018.

[32] S. Ryu, A. P. Schnyder, A. Furusaki, and A. W. Ludwig, "Topological insulators and superconductors: tenfold way and dimensional hierarchy," *New Journal of Physics*, vol. 12, no. 6, p. 065010, 2010.

[33] A. Kitaev, "Periodic table for topological insulators and superconductors," *AIP conference proceedings*, vol. 1134, no. 1, pp. 22–30, 2009.

[34] R. Bianco and R. Resta, "Mapping topological order in coordinate space," *Phys. Rev. B*, vol. 84, no. 24, p. 241106, 2011.

[35] E. Prodan, T. L. Hughes, and B. A. Bernevig, "Entanglement spectrum of a disordered topological chern insulator," *Phys. Rev. Lett.*, vol. 105, p. 115501, Sep 2010.

[36] D. T. Tran, A. Dauphin, N. Goldman, and P. Gaspard, "Topological hofstadter insulators in a two-dimensional quasicrystal," *Phys. Rev. B*, vol. 91, no. 8, p. 085125, 2015.

[37] N. P. Mitchell, L. M. Nash, D. Hexner, A. M. Turner, and W. T. Irvine, "Amorphous topological insulators constructed from random point sets," *Nat. Phys.*, vol. 14, no. 4, pp. 380–385, 2018.

[38] B. Irsigler, J. H. Zheng, and W. Hofstetter, "Interacting hofstadter interface," *Phys. Rev. Lett.*, vol. 122, p. 010406, Jan 2019.

[39] U. Gebert, B. Irsigler, and W. Hofstetter, "Local chern marker of smoothly confined hofstadter fermions," *Phys. Rev. A*, vol. 101, p. 063606, Jun 2020.

[40] L. Ulčakar, J. Mravlje, and T. Rejec, "Kibble-zurek behavior in disordered chern insulators," *Phys. Rev. Lett.*, vol. 125, p. 216601, Nov 2020.

[41] A. Marrazzo and R. Resta, "Locality of the anomalous hall conductivity," *Phys. Rev. B*, vol. 95, no. 12, p. 121114(R), 2017.

[42] A. Hayward, E. Bertok, U. Schneider, and F. Heidrich-Meisner, "Effect of disorder on topological charge pumping in the rice-mele model," *Phys. Rev. A*, vol. 103, no. 4, p. 043310, 2021.

[43] D. Varjas, M. Fruchart, A. R. Akhmerov, and P. M. Perez-Piskunow, "Computation of topological phase diagram of disordered pb 1- x sn x te using the kernel polynomial method," *Phys. Rev. Research*, vol. 2, no. 1, p. 013229, 2020.

[44] M. D. Caio, G. Möller, N. R. Cooper, and M. J. Bhaseen, "Topological marker currents in chern insulators," *Nat. Phys.*, vol. 15, no. 3, pp. 257–261, 2019.

[45] F. Song, S. Yao, and Z. Wang, "Non-hermitian topological invariants in real space," *Phys. Rev. Lett.*, vol. 123, p. 246801, Dec 2019.

[46] A. N. Kalish, R. S. Komarov, M. A. Kozhaev, V. G. Achanta, S. A. Dagesyan, A. N. Shaposhnikov, A. R. Prokopov, V. N. Berzhansky, A. K. Zvezdin, and V. I. Belotelov, "Magnetoplasmonic quasicrystals: an approach for multiband magneto-optical response," *Optica*, vol. 5, no. 5, pp. 617–623, 2018.

[47] M. Baake and U. Grimm, *Aperiodic Order*, vol. 1 of *Encyclopedia of Mathematics and its Applications*. Cambridge University Press, 2013.

[48] R. Ghadimi, T. Sugimoto, K. Tanaka, and T. Tohyama, "Topological superconductivity in quasicrystals," *Physical Review B*, vol. 104, no. 14, p. 144511, 2021.

[49] D. Johnstone, M. J. Colbrook, A. E. Nielsen, P. Öhberg, and C. W. Duncan, "Bulk localised transport states in infinite and finite quasicrystals via magnetic aperiodicity," *arXiv:2107.05635*.

[50] Y. E. Kraus and O. Zilberberg, "Topological equivalence between the fibonacci quasicrystal and the harper model," *Physical review letters*, vol. 109, no. 11, p. 116404, 2012.

[51] M. Yoshii, S. Kitamura, and T. Morimoto, "Topological charge pumping in quasiperiodic systems characterized by the bott index," *Physical Review B*, vol. 104, no. 15, p. 155126, 2021.

[52] F. Bloch, "Über die quantenmechanik der elektronen in kristallgittern," *Zeitschrift fur Physik*, vol. 52, pp. 555–600, July 1929.

[53] S. H. Simon, *The Oxford solid state basics*. OUP Oxford, 2013.

[54] J. K. Asbóth, L. Oroszlány, and A. Pályi, *A short course on topological insulators*. Springer, 2016.

[55] M. V. Berry, "Quantal Phase Factors Accompanying Adiabatic Changes," *Proceedings of the Royal Society of London Series A*, vol. 392, pp. 45–57, Mar. 1984.

[56] T. Fukui, K. Shiozaki, T. Fujiwara, and S. Fujimoto, "Bulk-edge correspondence for chern topological phases: A viewpoint from a generalized index theorem," *Journal of the Physical Society of Japan*, vol. 81, no. 11, p. 114602, 2012.

[57] R. S. Mong and V. Shivamoggi, "Edge states and the bulk-boundary correspondence in dirac hamiltonians," *Physical Review B*, vol. 83, no. 12, p. 125109, 2011.

[58] H. Zhai, "Degenerate quantum gases with spin–orbit coupling: a review," *Reports on Progress in Physics*, vol. 78, no. 2, p. 026001, 2015.

[59] J. Dalibard, "Introduction to the physics of artificial gauge fields," *Quantum Matter at Ultralow Temperatures*, 2015.

[60] M. Aidelsburger, S. Nascimbene, and N. Goldman, "Artificial gauge fields in materials and engineered systems," *Comptes Rendus Physique*, vol. 19, no. 6, pp. 394–432, 2018.

[61] P. G. Harper, "Single band motion of conduction electrons in a uniform magnetic field," *Proc. Phys. Soc. A*, vol. 68, no. 10, p. 874, 1955.

[62] S. Aubry and G. André, "Analyticity breaking and anderson localization in incommensurate lattices," *Ann. Israel Phys. Soc*, vol. 3, no. 133, p. 18, 1980.

[63] D. R. Hofstadter, "Energy levels and wave functions of bloch electrons in rational and irrational magnetic fields," *Physical review B*, vol. 14, no. 6, p. 2239, 1976.

[64] D. Osadchy and J. Avron, "Hofstadter butterfly as quantum phase diagram," *Journal of Mathematical Physics*, vol. 42, no. 12, pp. 5665–5671, 2001.

[65] T. A. Loring and M. B. Hastings, "Disordered topological insulators via C^*-algebras," *EPL (Europhysics Letters)*, vol. 92, no. 6, p. 67004, 2011.

[66] M. B. Hastings and T. A. Loring, "Almost commuting matrices, localized Wannier functions, and the quantum Hall effect," *Journal of Mathematical Physics*, vol. 51, no. 1, p. 015214, 2010.

[67] M. B. Hastings and T. A. Loring, "Topological insulators and C^*-algebras: Theory and numerical practice," *Annals of Physics*, vol. 326, no. 7, pp. 1699–1759, 2011.

[68] T. A. Loring *et al.*, "Quantitative K-theory related to spin Chern numbers," *SIGMA. Symmetry, Integrability and Geometry: Methods and Applications*, vol. 10, p. 077, 2014.

[69] D. Toniolo, "Time-dependent topological systems: A study of the bott index," *Physical Review B*, vol. 98, no. 23, p. 235425, 2018.

[70] N. Marzari, A. A. Mostofi, J. R. Yates, I. Souza, and D. Vanderbilt, "Maximally localized wannier functions: Theory and applications," *Rev. Mod. Phys.*, vol. 84, no. 4, p. 1419, 2012.

[71] N. Marzari and D. Vanderbilt, "Maximally localized generalized wannier functions for composite energy bands," *Phys. Rev. B*, vol. 56, no. 20, p. 12847, 1997.

[72] A. Messiah, *Quantum mechanics*, vol. 2. Elsevier, 1981.

[73] A. Kitaev, "Anyons in an exactly solved model and beyond," *Annals of Physics*, vol. 321, no. 1, pp. 2–111, 2006.

[74] J. Avron, L. Sadun, J. Segert, and B. Simon, "Chern numbers, quaternions, and berry's phases in fermi systems," *Commun. Math. Phys.*, vol. 124, no. 4, pp. 595–627, 1989.

[75] D. Xiao, M.-C. Chang, and Q. Niu, "Berry phase effects on electronic properties," *Rev. Mod. Phys.*, vol. 82, no. 3, p. 1959, 2010.

[76] T. Olsen, M. Taherinejad, D. Vanderbilt, and I. Souza, "Surface theorem for the chern-simons axion coupling," *Physical Review B*, vol. 95, no. 7, p. 075137, 2017.

[77] M. Nakahara, *Geometry, topology and physics*. CRC Press, 2003.

[78] J. E. Moore, "An introduction to topological phases of electrons," *Topological Aspects of Condensed Matter Physics: Lecture Notes of the Les Houches Summer School*, vol. 103, p. 1, 2017.

[79] A.-L. He, L.-R. Ding, Y. Zhou, Y.-F. Wang, and C.-D. Gong, "Quasicrystalline chern insulators," *Physical Review B*, vol. 100, no. 21, p. 214109, 2019.

[80] J. Bellissard, B. Iochum, E. Scoppola, and D. Testard, "Spectral properties of one-dimensional quasi-crystals," *Communications in Mathematical Physics*, vol. 125, no. 3, pp. 527–543, 1989.

[81] O. Zilberberg, "Topology in quasicrystals," *Optical Materials Express*, vol. 11, no. 4, pp. 1143–1157, 2021.

[82] A. Jagannathan, "The fibonacci quasicrystal: case study of hidden dimensions and multifractality," *Reviews of Modern Physics*, vol. 93, no. 4, p. 045001, 2021.

[83] S. Kivelson, "Wannier functions in one-dimensional disordered systems: Application to fractionally charged solitons," *Physical Review B*, vol. 26, no. 8, p. 4269, 1982.

[84] Q. Niu, "Theory of the quantized adiabatic particle transport," *Modern Physics Letters B*, vol. 5, no. 14n15, pp. 923–931, 1991.

[85] A. Nenciu and G. Nenciu, "The existence of generalised wannier functions for one-dimensional systems," *Communications in mathematical physics*, vol. 190, no. 3, pp. 541–548, 1998.

[86] S. Ganeshan, K. Sun, and S. D. Sarma, "Topological zero-energy modes in gapless commensurate aubry-andré-harper models," *Physical review letters*, vol. 110, no. 18, p. 180403, 2013.